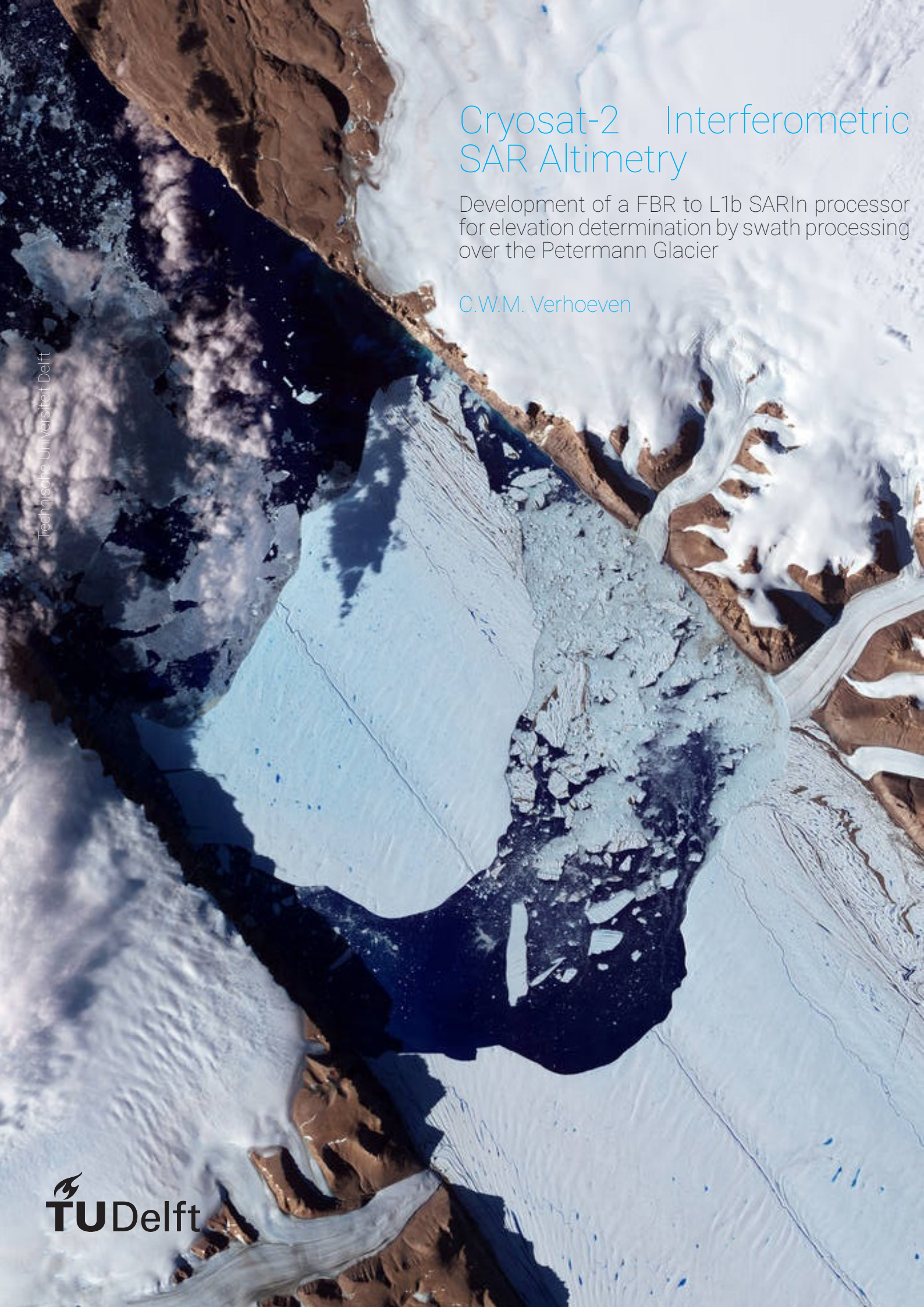

Cryosat-2 Interferometric SAR Altimetry

Development of a FBR to L1b SARIn processor for elevation determination by swath processing over the Petermann Glacier

C.W.M. Verhoeven

Technische Universiteit Delft

TU Delft

Cryosat-2 Interferometric SAR Altimetry

Development of a FBR to L1b SARIn processor for elevation determination by swath processing over the Petermann Glacier

by

C.W.M. Verhoeven

to obtain the degree of Master of Science
at the Delft University of Technology,
to be defended publicly.

Student number: 4038452
Project duration: January 23, 2018 – December 21, 2018
Thesis committee:
Dr. ir. W. van der Wal, TU Delft, Chairman
Dr. Ir. D. C. Slobbe, TU Delft, External Supervisor
Dr. Ir. E. J. O. Schrama, TU Delft, Daily Supervisor
Dr. Ir. M. Kleinherenbrink, TU Delft, Member

An electronic version of this thesis is available at `http://repository.tudelft.nl/`.

TU Delft

Preface

It has been a long journey from the start of my study towards the point I am at now. It was my master period in which I believe I really started to think about my future and the direction I wanted to go in. After having completed my final bachelor project, by designing a SAR constellation, for solely monitoring the North-Sea, my interest in Space was awakened. I did not yet know exactly which direction of the project drew my attention, however I knew Space was the way to go. In order to clear this up for me I decided to apply for a part-time job at Science & Technology in Delft. A project member had been working there for a while already, and showed me that working in the space industry is not at all reserved for the best of the best at publicly funded institutes as ESA and NASA.

My initial task was about researching new earth observation opportunities that could be realized by using the publicly available satellite data from for example the Copernicus programme. Once a month I had to present my findings to an earth observation expert from ESA and one of the managing partners of S&T. The fact that I was taken seriously by those guys was totally new to me. Furthermore, it showed me that space was booming and earth observation techniques really had something to offer. Reading all these documents enlarged my view into the field of remote sensing and satellite observations. I discovered that all I wanted to do was dive into the details and see what the techniques were exactly about. As if my superiors knew more about my ambitions than I did at that point, I was appointed to work at an S&T start-up known as Orbital Eye.

At Orbital Eye I was assigned tasks related to the processing of Sentinel-1 SAR data. The signal processing involved was extremely interesting to me, but remained too complex to grasp. As I was working for only one day a week I was not able to get a full understanding of the signal processing involved and this bothered me. Hence, I started to search for a thesis subject in the field. I was pointed towards Ejo Schrama, who introduced me to Cryosat-2 SAR altimetry, of which the signal processing involved is based on the same principles.

The collaboration started off with my year-long literature study. At this point I find myself often wondering what the exact reason is that it took so long. It may for example be related to the fact that I can spend too much time on small details instead of looking at the greater picture. Clearly, this thesis has been really helpful in realizing such facts about myself. Furthermore, this thesis has really helped me see the beauty of engineering and research. I find myself more often than before, searching the internet for engineering and science related topics, just for the sheer interest in learning new things. I have always had utmost respect for researchers, but during this project this respect has grown, as I can now see the effort and dedication it takes.

I would like to thank a lot of people for sticking with me. I would like to thank Ejo, for his support and his occasional technical anecdotes, Cornelis for his critical view and effort he put in my project, and Marcel for his enthusiastic and thorough explanations on SAR altimetry theory. Furthermore, I would like to thank my parents and both of my sisters for their trust in my sometimes lacking planning capabilities, and off course, my girlfriend, my Rotterdam friends and room-mates for helping me getting out of my working bubble every once in a while.

C.W.M. Verhoeven
Delft, December 2018

Contents

List of Abbreviations

AABR Azimuth Angular Beam Resolution. 29

AGC Automatic Gain Control. 28

ATM Airborne Topographic Mapper. 25

BRI Burst Repetition Interval. 12

CUC Cryosat Users Characterization. 28

CW Continuous Wave. 15

D/D Delay/Doppler. 18

DEM Digital Elevation Model. 3, 25, 28

DORIS Doppler Orbitography and Radio positioning Integrated by Satellite. 17

ECEF Earth-Centered Earth-Fixed. 29

ESA European Space Agency. 2, 13

FBR Full Bit Rate. 2, 13, 14

FFT Fast Fourier Transform. 18, 20

GIC Greenland Glaciers and Ice Caps. 5

GIMP Greenland Ice sheet Mapping Project. 25

GPS Global Positioning System. 25

GRACE Gravity Recovery And Climate Experiment. 5

GrIS Greenland Ice Sheet. 5

I/Q In-phase and Quadrature. 13

IB IceBridge. 3, 25

ICESat Ice, Cloud, and land Elevation Satellite. 25

L1b Level 1b. 2, 18

L2 Level 2. 18, 25

LIDAR LIght Detection And Ranging or Laser Imaging Detection And Ranging. 25

LPF Low Pass Filter. 14, 15

LRM Low Resolution Mode. 18

MNP Maximum Number of Peaks. 49

NASA National Aeronautics and Space Administration. 25

POCA Point of Closest Approach. 2, 24

PRF Pulse Repetition Frequency. 12, 18

PRI Pulse Repetition Interval. 12

SAR Synthetic Aperture Radar. 2, 8, 18

SARIn Interferometric SAR. 1, 11, 12, 16

SCOOP SAR Altimetry Coastal and Open Ocean Performance. 27

SIRAL Synthetic Aperture Radar Interferometric Radar Altimeter. 1, 11, 13, 14

SNR Signal-to-Noise Ratio. 23

SRC Slant Range Correction. 22, 33

SSW Sample Stack Weighting. 32

TU Technical University. 27

WDC Window Delay Correction. 22, 33, 34, 45

WGS-84 World Geodetic System 1984. 25

ZP Zero-padding. 35

List of Symbols

B The bandwidth of a chirp [Hz]. 12, 15

B_I Interferometric Baseline, the separation between the two antennae used for an interferometric purpose. 12

H_{mask} Mask which is applied to remove wrapped samples due to geometric corrections. 35

H_{sat} The altitude of the satellite w.r.t the WGS-84 ellipsoid. 37

H_{surf} The surface elevation measurement w.r.t to the WGS-84 ellipsoid. 37

I The interferogram. 36

K Chirp rate, Bandwidth over pulse time. 15

N Radius of curvature in the prime vertical. 37, 38

N_{IB} The number of IB measurements which are used for comparison. 54

N_L Number of looks within multi looked product. 34

N_{meas} Number of measurements used in elevation comparisons. 38, 54, 58

N_p Number of pulses within a burst. 32

$N_{s,FBR}$ Number of samples within a power waveform. 12, 33

$N_{s,L1b}$ Number of samples within a power waveform. 12

S_R Range Resolution. 33

$\Delta\phi_{bs,pj}$ Relative phase difference for pulse i, to be corrected for within the beamsteering step. 31

Δ_{ml} The interferometric phase. 36, 37

Δs Sum of geometric corrections, equal to shift in number of range bins. 33

Φ_b Complex phase term used to apply beamsteering correction. 32

Φ_{gc} Complex phase term used to apply the sum of geometric corrections. 33

$\Psi\overline{\Psi}^{(+,-)}_{ml}$ The multi looked cross-product. 34, 35

$\Psi^{(+)}\overline{\Psi}^{(+)}_{ml}$ Complex positive channel signal in frequency domain. 35

$\Psi^{(+)}_{masked}$ The masked Fourier transform of one beam. 34

$\Psi^{(+/-)}_{masked}$ The power waveform corresponding to one beam, or one look, and one of the two channels (+/-). 34

$\Psi^{(-)}\overline{\Psi}^{(-)}_{ml}$ Complex negative channel signal in frequency domain. 35

α_i Angle between nadir and in-orbit burst location to burst surface position i. 29

β The roll angle of the baseline. 37

$\epsilon_{Geophysical}$ The geophysical corrections. 37

λ_c Carrier signal wavelength [m]. 18, 19, 29

μ_{IB} Mean of the differences between measured elevations and IceBridge Elevations. 54

$\overline{\Psi}^{(-)}_{masked}$ The complex conjugate of the masked Fourier transform of one beam. 34

ϕ_{geod} The geodetic latitude. 38

ψ_{gc} A geometry corrected burst. 34

σ_{DEM} Standard deviation of the differences between measured elevations and DEM elevations. 38, 54

σ_{IB} Standard deviation of elevation differences compared to IB elevations. 54

τ_B Total burst time. 19, 29

$\tau_{WD,ref}$ The reference window delay time to which the different stack samples are corrected. 34

τ_{WD} The window delay of a burst. 34, 37

τ_{eff} Effective two-way travel time resolution. 33, 37

τ_{pulse} The time of the pulse [s]. 12, 34

τ_{ret} The retracking correction as found after retracking of the waveforms. 37

θ_{AABR} Azimuth Angular Beam Resolution (AABR). 29

θ_{SSW} The angle used in Surface Sample Stack Weighting. 32

θ_{ac} Along-track look angle, the angle between the scatterer direction and the line to surface perpendicular to the velocity vector. 37, 54

θ_c Beam angle, angle between velocity vector and beam direction.. 31, 32

θ_l Along-track look angle, the angle between the scatterer direction and the line to surface perpendicular to the velocity vector. 18

$\vec{h}$ The height vector to nadir. 34

$\vec{n}$ Vector from orbit burst location towards nadir. 29

$\vec{v}_s$ Satellite velocity vector. 18, 29

$\vec{w}_{sat\rightarrow b_i,surf}$ Vector from orbit burst location towards i'th burst surface location. 29

$\vec{w}_{sat\rightarrow surf}$ Vector from Satellite to surface location as previously computed using the AABR. 30

a Semi-major Axis of Earths ellipsoidal approximation. 38

b' The index of a beam within a stack. 33

e Eccentricity of Earth's ellipsoidal approximation. 38

f_c Carrier Frequency [Hz]. 12, 13, 15

k Wavenumber. 31, 37

p Pulse Index, index of pulse within a burst. 32

1 Introduction

The evidence for Global Warming is compelling, and the effects cannot be neglected any more. Global temperatures have risen, at the surface as well as in the oceans, the major ice sheets are decreasing in mass, glaciers are retreating, sea level rise has been recorded with higher rates than ever measured before, the arctic sea ice is declining, and last but not least more and more extreme weather events are reported globally (Wuebbles et al., 2017) (IPCC, 2013). As such, terms as "Climate Change" and "Global Warming" make up a large portion of the current political agenda. The temperature rise is a global scale event which can have major influence on the future of the earth, and may, when not dealt with, induce irreversible changes to our planet. This is why major scientific effort is put into assessing the scale of the issue, and predicting the impact it has and will have.

In order to make such assessments, accurate observations are required. Observations which show the progression of global warming and can help in predicting the future trend. One of the types of such observations are measurements of the ice extent on earth, as the decline of this ice is one of the major effects of global warming.

The Cryosphere is the collection of all portions of the world where ice is present, the melting of which is a major indicator for the presence of global warming. Most of the research into ice melting on earth is focused on the Antarctic and Greenland. These ice bodies are shown to lose mass over time. Satellite remote sensing techniques as radar/laser altimetry and gravimetry have proven to be an highly efficient aid in observing the vast lands that are part of the Cryosphere. Over recent years, satellites have become more and more advanced and estimates of mass losses are getting preciser every day.

The most dynamic changes in ice mass are occurring locally within the coastal regions of the larger ice bodies (Gardner et al., 2013). These regions contain glaciers and ice shelves, which terminate into the oceans. The topography of these areas are often highly variable, and thus a high spatial resolution is required to correctly assess the changes. Because of its high resolution altimetry has proven its value, in this respect.

Radar altimetry has been used to derive surface elevation changes of ice sheets and glaciers over time and is used to determine ice mass balance and the effects on sea-level rise (Zwally et al., 2005) (Helm et al., 2014). One of the satellites performing these types of measurements is the Cryosat-2. The Interferometric SAR (SARIn) operational mode of the radar altimeter Synthetic Aperture Radar Interferometric Radar Altimeter (SIRAL) as installed on Cryosat-2 is specifically designed for the purpose of observing topographic areas which are highly variable (Wingham et al., 2006). In along-track direction, the spatial resolution is increased by making use of the Delay/Doppler processing (Raney, 1998), whereas in the across-track direction the scatterer location is determined from a phase difference measurement (Jensen, 1999). These methods increase the capabilities of radar altimetry over regions of rough topography. However, these methods have serious limitations. The data shows high biases over areas that are steeper and topographic peaks will be oversampled which can result in positive biased measurements (Wang et al., 2015). The topography in the vicinity of glaciers is often highly variable, as they are enclosed by large cliffs. In contrast, within the glaciers local topographic variations as rifts are present, which are important determinants of glacier behaviour as melting rate and ice breaking events (Joughin and MacAyeal, 2005). Accurate monitoring of local topography of these ice masses is therefore of utmost importance to reliably predict future trends.

A method currently under a lot of attention which could provide improvement in overcoming the difficulties encountered in observing these complex topographic areas is interferometric Swath Processing (Hawley

et al., 2009) (Foresta et al., 2016). Swath processing increases its measurement density in across-track direction by making the assumption that the radar echo is coming from one side of the point on the surface nearest to the satellite, the Point of Closest Approach (POCA), instead of two directions, and thus is unambiguous. By doing so an entire Swath of data points can be obtained in across-track direction, in addition to the one POCA SARIn measurement. The extra measurements are obtained at the expense of a small loss of quality compared to the POCA measurements (Gourmelen et al., 2017).

The Swath processing algorithm uses data supplied by European Space Agency (ESA). ESA processes Full Bit Rate (FBR) or the raw satellite radar data into Level 1b (L1b) power waveforms. The L1b waveforms are provided by ESA. In essence, Swath only uses part of the data that fulfil certain quality criteria. These values can be found in the level 1b data from ESA. As a result most related research makes use of these L1b results and do not question the influence the FBR to L1b processing has on the eventual derived elevations.

1.1. Research question

Glaciers show large variations in local topography, and prediction of glacier behaviour very much depends on the presence of such variations in local topography. Current radar altimetry does not accurately measure steep slopes, peaks and steep rifts, as they very strongly affect the scattered signal. Swath Processing algorithms potentially improve radar altimetry signal processing but relies on FBR-to-L1b processing of data already performed by and supplied by ESA. The FBR-to-L1b processing by ESA is not optimized for specific applications, and the effect of this data processing by ESA on accuracy of ice mass monitoring is unknown. We hypothesized that an FBR-to-L1b processing scheme that is dedicated specifically for ice mass detection in the steep margins improves the quality of data input for the Swath algorithm and hence improves radar altimetry of ice masses. Our research questions therefore are:

Can we develop a FBR-to-L1b processing scheme that can serve as input to radar swath altimetry?

and

Are local Swath processed elevation measurements in the margins of large ice bodies improved by this FBR-to-L1b processing?

1.2. Approach

In this study, we developed a FBR-to-L1b processor for the SARIn mode on Cryosat-2 based on the Synthetic Aperture Radar (SAR) processor as described in Cipollini (2016) and written by Slobbe et al. (2016), and compared the eventual Swath Processed elevations to the same elevations following from the ESA provided L1b waveforms.

To test the performance of the processing scheme developed in this thesis, we focussed our analyses on one specific glacier, namely the Petermann Glacier located in North-West Greenland. The Petermann Glacier is one of the large outlet glaciers of Greenland. This glacier has been showing large cracks (see figure 1.1) that could predict a breaking-off event as has happened with Larsen C in Antarctica (Tollefson, 2017).

In our study, the approach steps were as follows:

1. Develop, and implement the FBR to L1b processing for Cryosat SARIn FBR data, based on the SAR processor written by Slobbe et al. (2016).

2. Implement the Swath processing algorithm.

3. Generate L1b datasets and Swath processed L2 datasets over the Petermann Glacier from ESA provided L1b products as well as FBR derived L1b products.

4. Verify the FBR to L1b processor, by comparing L1b results to ESA provided L1b results, and by comparing retracked L2 results to a DEM.

5. Validate the FBR derived L2-Swath results, and assess the sensitivity to different FBR to L1b processing variables, by comparing the results to the IceBridge Laser Altimetry data and the corresponding L2-Swath results derived from ESA L1b product.

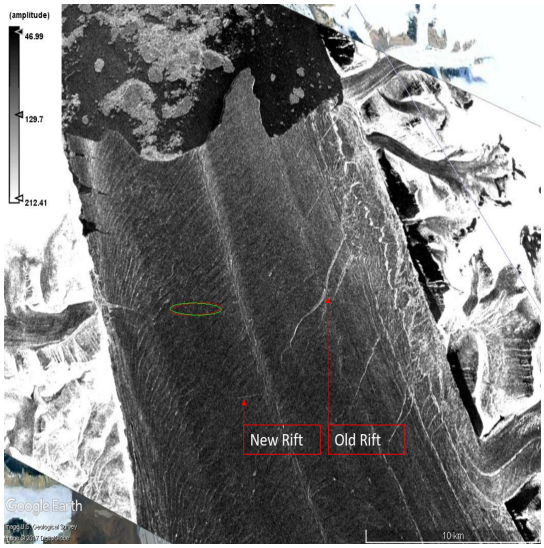

Figure 1.1: Petermann Glacier cracks, Sentinel-1 image of 28 August 2017, showing the old and new rifts.

1.3. Outline of this thesis

First the area of interest, the Petermann Glacier, is described in chapter 2. In chapter 3 the theory concerning Radar altimetry, SARIn processing and swath processing is explained. In chapter 4, the methodology concerning the development of FBR-to-L1b processor and the implementation of the swath processing algorithm will be discussed. The results that follow from the FBR-to-L1b processing steps will be verified in chapter 5. In the subsequent chapter 6 the actual Swath elevations will be determined, and these will be validated by comparing them to a Digital Elevation Model (DEM) and the operation IceBridge (IB) Laser Altimetry elevations. This chapter includes a small assessment of the sensitivity of the L2-Swath results on a selection of the lower level processing input settings. Finally, the conclusions and recommendations that follow from the research are described in chapter 7.

2

Study Area

The study area as outlined in the introduction is the Petermann Glacier. The Petermann Glacier is located in the marginal area of Greenland, and is one of its largest outlet Glaciers. The glacier runs out into the ocean, and consists for a large part of a floating ice shelf. The glacier is known for it's large scale calving events.

In this chapter these aspects will be shortly addressed, and it is attempted to give and insight into why this Petermann Glacier was chosen to be the area of interest.

2.1. Greenland Ice

The ice on Greenland represents about 10% of the total world ice mass. The ice sheet covers $1.7 \cdot 10^6$ $[km^2]$, covering roughly 80% of the surface of Greenland. The mean altitude is 2135 [m]. The thickness of the ice sheet is generally more than 2 [km]. All of the Greenland ice, would, when melted be equivalent to 7.2 [m] in sea level rise. The distribution of ice thickness can be seen in figure 2.1, where the more grey the image is the thicker the ice layer is.

It can be seen as well in figure 2.1 that not all of Greenland sub-ice land is above sea level. In the center of Greenland a large subglacial canyon is present also known as the Greenland Grand Canyon. Furthermore, the topographical variations in the margins are clearly visible. While the topographical variations reach up to heights of around 3700 [m], the highest values of ice thickness are found closer to the center of the ice sheet, with a value of around 3200 [m].

2.2. Marginal area

The marginal area of Greenland is the coastal area which consists of glaciers and ice caps. It covers around $9 \cdot 10^5$ $[km^2]$, representing 12 % of the global glaciated area. Melting of the Greenland Ice Sheet (GrIS), and the surrounding glaciers and ice caps (GIC) contribute 43[%] to sea level rise (Noël et al., 2017). While the centrally located ice sheet is studied to a great extent, the processes that occur in the GIC are not well documented, as the processes involved are complex. It is however found that these parts do contribute significantly to the sea level rise (Gardner et al., 2013) (Pritchard et al., 2009). Moreover, following Gravity Recovery And Climate Experiment (GRACE) measurements locations of highest ice mass loss are found to be located at the Southeastern and Northwestern coasts of Greenland (Wouters et al., 2008).

2.2.1. Glaciers

Glaciers are vast bodies of moving ice, which have been formed by accumulation of many years of snow. The glaciers move and deform due to the stresses that are induced by the weight of the ice, and the slope on which it is located. A lot of Glaciers exist on Greenland, all varying in size. The loss of the ice due to an accelerated flow is called dynamic thinning, and is dominantly present in the margins of Greenland. Accelerating of several large glaciers in Greenland is observed, which have resulted in increased ice loss of these regions (Rignot and Kanagaratnam, 2006).

The motion of these glaciers is mainly driven by the gravitational force exceeding the friction it experiences with the surface underneath. In such a way a basal shear stress is created in the direction of the slope. The motion can be compared to the flow of any fluid. This flow is related to the shear strain (flow) rate, as

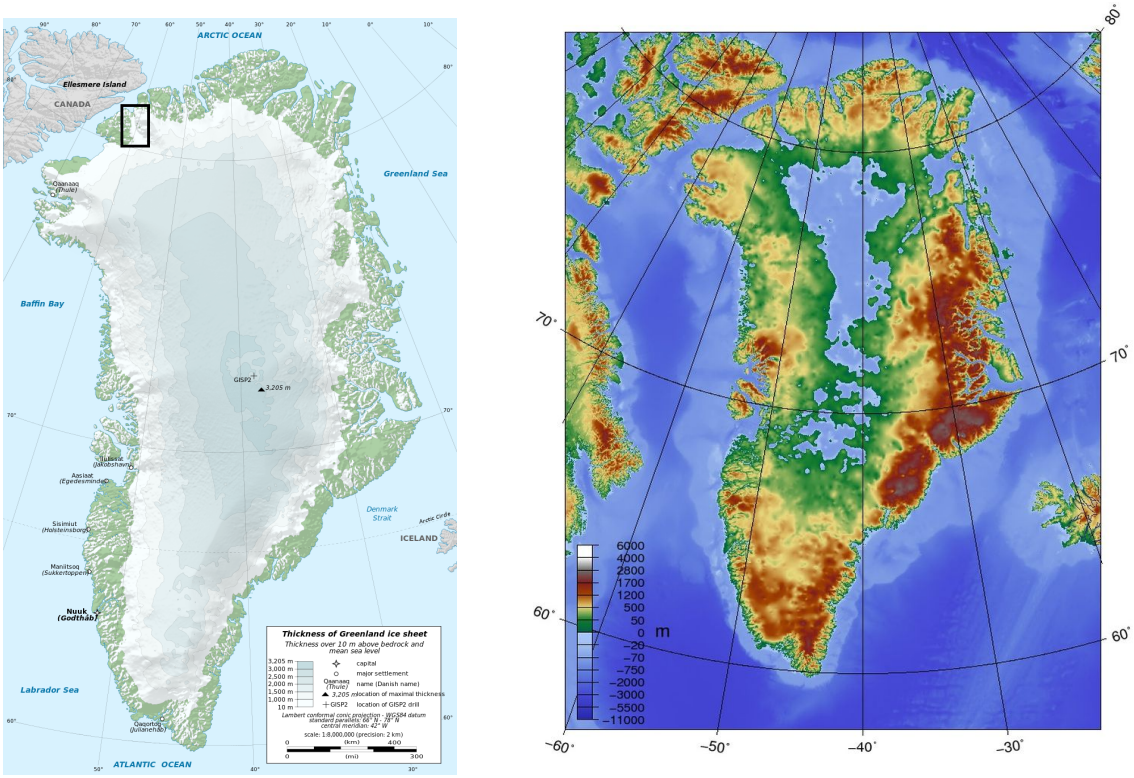

Figure 2.1: Greenland ice versus Greenland land [Credit: WikiMedia Commons]. The black box shows the location of the Petermann Glacier.

put by the Glen-Nye Flow Law, linking the amount of shear stress to the shear strain rate (Fu and Cazenave, 2001).

$$\dot{\epsilon} = K\tau^n \tag{2.1}$$

In which the $\dot{\epsilon}$ denotes the stress strain rate, K a constant dependent on temperature, τ the shear stress, and n another stress-strain constant. A typical value of n for glaciers is "3". Only after the ice layer is thick enough the ice mass is heavy enough to overcome the basal surface friction causing the flow to become more plastic and increase deformation. This is dependent on the slope. This motion and the shear friction is much more complicated than a pure surface friction as described by formula 2.1. The combination of the geothermal heat and the heat resulting from the friction melt the base of the ice sheet, increasing the sliding effect. Because of the immense forces inherent to these processes, major erosion occurs within their lifetime, which has the effect of creating fjords and valleys.

2.2.2. Ice Shelves

In these regions where ice is not grounded anymore the coupling with sea level rise becomes apparent. The border at which these transmissions occur are called grounding lines as is visible in figure 2.2. At these grounding lines ice shelves are created. Ice shelves are the parts of glaciers that departed the continental land, and continue their way on to the sea. Here the ice is calved by the water, due to a combination of tidal movements and melting. The entire system is known as a tidewater glacier. The melting of these ice shelves add to the sea level rise due to the difference in density of the fresh water ice with respect to the sea water. However, this is not in large quantities (Shepherd et al., 2010).

The larger effect that ice shelf melting decline has on sea level rise is linked to the glaciers systems they origin from. The ice shelves provide a resistant force against the glacier, known as buttressing. This buttressing force functions as a cork for the outlet glacier (Rignot et al., 2004). It is shown by observing flow velocities that, from the moment of ice shelf collapse, the flow of land ice into the ocean can accelerate. The rate at which the ice crosses the grounding line is directly linked to the ice shelf thickness as well as depth (Pritchard et al., 2012).

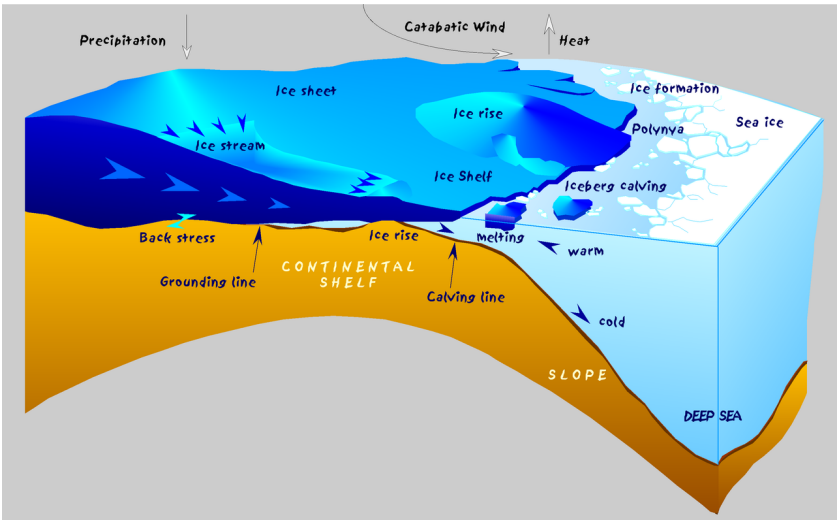

Figure 2.2: Grounding line ice sheet dynamics [Credit: Wikimedia Commons]

Most of the ice shelves that are present on the earth are located in the Antarctic, and hence most ice shelf studies focus on this area. Previous research has shown a steady retreat of the ice shelves. Radar altimetry measurements spanning multi-decadal periods show that most of the ice shelves have been thinning substantially (Fricker and Padman, 2012) (Paolo et al., 2015).

2.2.3. Calving

The ice shelves decrease in size due to calving, during which chunks of ice break off. Small calving events, where relatively little chunks break off of the ice shelf, occur on a regular basis. However, calving events are also observed in which chunks break off at once, to form large Icebergs, denoted as Iceberg calving.

Such events are observed only on average twice in a decade. As a consequence, the knowledge about the corresponding mechanisms is rather small. A known fact is that the ice berg calving is initiated by rifts propagating through the ice shelf. These rifts are large fractures that originate inside the ice body as consequence of the loadings that are working upon the ice shelf. Eventually, rifts can cause big chunks of ice to break off of an ice shelf, to form large individually floating ice bergs (Tollefson, 2017).

Several factors are named when considering the propagation and origin of these rifts and the eventual calving ice bergs. As the processes involved are dependent on the local environment no trivial driving factor can be distinguished. The following factors are named in literature:

- Glaciological stresses
- Ocean Forcing
- Tidal effects
- Bathymetry
- Composition of the ice (Ice Melange)
- Additional external factors

The Glaciological stresses are inherent to the working principle of the Glacier. As was mentioned earlier the ice shelf serves as a cork for the movement of the ice within the glacier. The ice shelf blocks the flowing ice from running dry. As a consequence tensions are created within the ice shelf. These tensions are considered to be the main force linked to propagation of rifts and the ultimate calving (Joughin and MacAyeal, 2005).

Two types of fractures in ice shelves are observed (Braun et al., 2008): The first one originates from tensile stress and are mostly seen as cracks in the ice perpendicular to the ice flow direction. These are called mode 1 cracks. Secondly, there are cracks that are shear stress related. Cracks of this second mode are found parallel to flow direction, and are often found in areas where fast and slow moving ice combines. It was shown in

earlier research that such shear-mode cracks preconditioned ice shelf break up for Larsen B (Glasser and Scambos, 2008).

Ocean forcing is the process in which the ice shelf is melted from underneath, due to warmer waters. Thinning of the ice shelf from underneath is the consequence, known as basal melting, which induces a further weakening as well (Pritchard et al., 2012). This creates basal crevasses that can transform into rifts or can cause pre-existing rifts to propagate further.

As the ice is floating on water, tidal forcing was suggested to have an influence on the propagation of these rifts (Christie et al., 2016).

Furthermore, the local bathymetry is suggested to be of influence to calving. Faster ice flows where observed at locations where an inland downward bathymetric slope was present (Paolo et al., 2015).

Moreover, the propagation of these fractures over time is found to be dependent on the characteristics of the ice. It was found that the suture zones, the zones in which multiple streams of outlet glaciers combine, provide favourable conditions for blocking crack propagation (Borstad et al., 2017). The ice at these flow boundaries is more fracture tough, due to its material properties, with main factor its heterogeneity. The suture zones mostly form downstream small peninsulas close to the grounding line of the glaciers.

The composition of the ice within the rifts is also suggested to be related to rift propagation, as was concluded from measurements showing a seasonal dependency of rift propagation rate (Fricker et al., 2005). The measurements showed higher propagation rates within summer in contrast to winter. In winter the ice melange within the rifts might induce a stronger bond due to freezing.

Furthermore, the calving events were found to be case-specific, in the sense that external factors influenced ice shelf stability. Local external factors as ocean currents, air temperature and iceberg impacts (Massom et al., 2015) are to be considered.

All these factors contribute to the fact that ice calving can occur on short time notice. Mean flow motion of glaciers is around 1 [m] a day. At some moments in time these mean velocities are exceeded extensively in so called surges. These surges can be a result of a sudden instability or tipping point.

2.3. Petermann Glacier

For this study, the Petermann Glacier is chosen as a study area, mainly due to the fact that it is features the second largest floating ice shelf in the Northern Hemisphere (Münchow et al., 2016). Furthermore, the glacier has exhibited calving events in the past (2010 and 2012) where large chunks of ice break of all at once, followed by an increase in flow velocities of up to more than 1 [km/y] (Münchow et al., 2016). Recently, new cracks have been discovered, which are suspected to cause new calving events in the near future. These cracks are shown in figure 1.1, which is a Sentinel-1 optical Synthetic Aperture Radar (SAR) image. As can be seen in figure 1.1, the old big rift nearly reaches the central channel. More accurate local altimetry measurements may aid in assessing the major causes of these rifts to propagate and the ice berg calving events that follow.

The Petermann Glacier is an example of a tidewater glacier, and is located in the North-West of Greenland (Münchow et al., 2016). The Petermann glacier is 50 [km] long measured from the grounding line and 15 [km] wide, flanked on both sides by elevated lands as can be seen in figure 2.3. The ice thickness, hence the thickness of ice below and above the water level, range from 600 [m] at the grounding line, towards 30-80 [m] at the front. The ice shelf contains a central channel (see fig. 1.1), which is on average thinner than the surrounding thick ice shelves. Rifts propagate from the side inwards. These rifts can eventually cause big chunks of ice to calve off all at once. Major calving events like this already occurred before in 2010 (see fig. 2.4) and 2012 (See cover Photo). Furthermore, a tidal force is active on the floating part of the Petermann Glacier (Münchow et al., 2016). The movement increases in deviation closer to the calving front, reaching up to 1 [m] amplitudes.

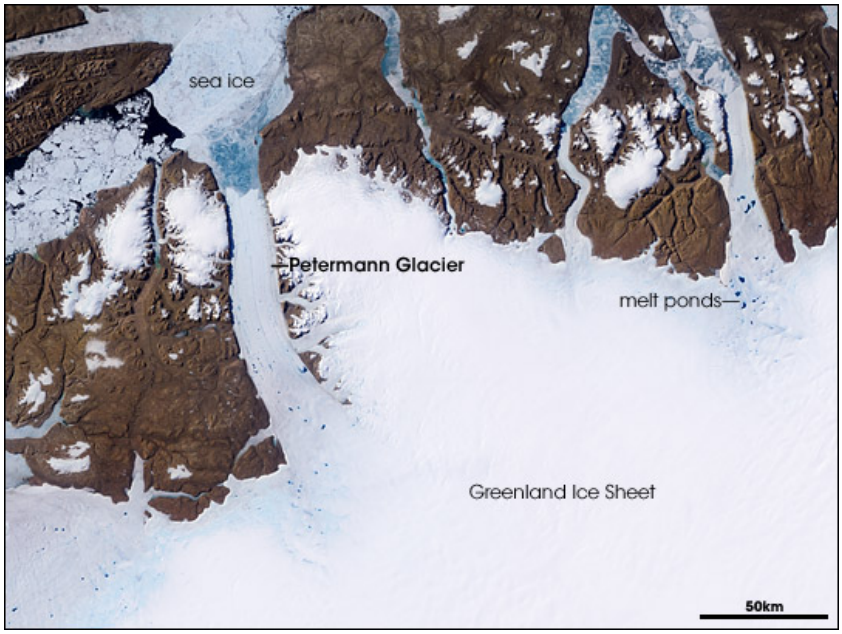

Figure 2.3: The Petermann Glacier [Credit: WikiMedia Commons]

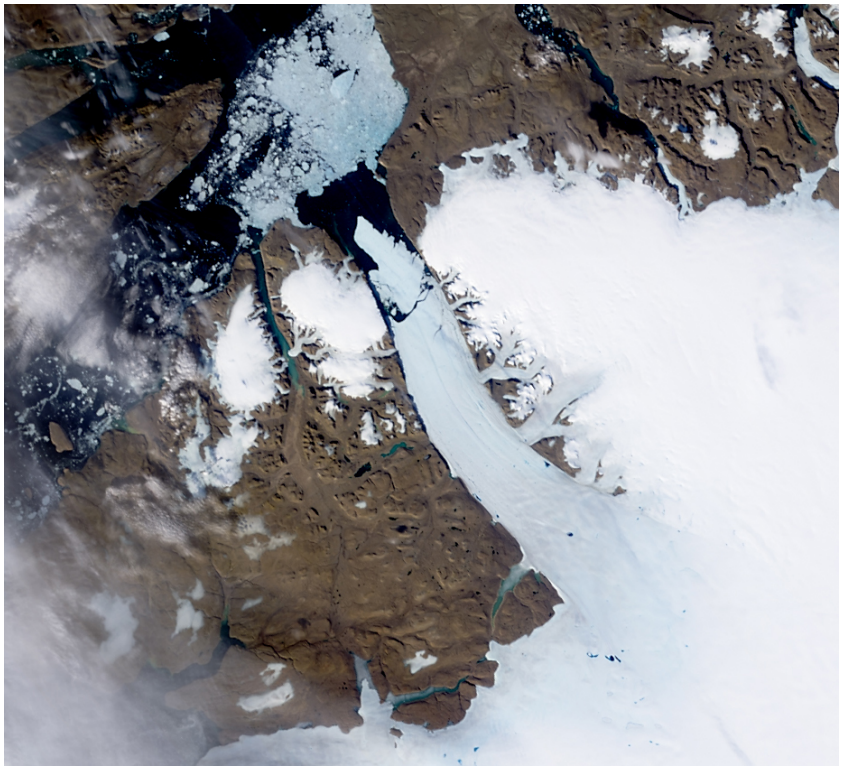

Figure 2.4: Previous major calving event of the Petermann Glacier in August 2010 [Credit: WikiMedia Commons]

3
Background

In this chapter a background will be given on the subject of radar altimetry and the research involved, specified to this specific thesis. At first the principles of radar altimetry will be shortly addressed in 3.1, as well as the satellite Cryosat-2 of which the data is to be used. Consequently, the steps involved to produce elevations of the raw Cryosat-2 radar data will be discussed in 3.2 until 3.4.

3.1. Radar Altimetry

Altimetry is the technique of measuring distance to a surface of interest by measuring the time it takes for a signal to be transmitted, scattered from the surface and returned to the receiver. The corresponding instrument, the altimeter, can be employed from satellite or aircraft. Both are used in combination for validation purposes. Furthermore, two distinct methods which are applied are Radar altimetry and Laser altimetry. The biggest difference between the two approaches is the type of signal that is used: Laser for the one and Radio waves for the other (Fu and Cazenave, 2001). The focus within this research will be Radar altimetry.

3.1.1. Cryosat-2

Since 2010 in orbit, and still operational is the Cryosat-2, a radar altimeter satellite. The altimeter on-board of the satellite is called the Synthetic Aperture Radar Interferometric Radar Altimeter (SIRAL). The satellite was launched, as the name suggests, to monitor the changes in the Cryosphere, and was one of the missions from ESA's living planet program. The program that might be known from the recently launched Aeolus mission.

Satellite The satellite was constructed by EADS Astrium. It was launched in 2010 after the launch failure of Cryosat-1 in 2005.

Cryosat-2 is positioned in a 92 ° inclination polar orbit, making it able to monitor the high latitude Arctic regions. This inclination was chosen as a compromise between high crossover coverage at high latitudes for land ice monitoring, and maximum coverage of the Arctic ocean and Antarctic. With a mean altitude of 717 [km] and an eccentricity of 0.0088 it has a period of 99.2 minutes. The repeat orbit is 369 days, in which the satellite makes 5344 revolutions with an inter-track spacing of 7.5 [km] at the equator. Furthermore, a subcycle of 30 days is present. This means that after 30 days the satellite covers approximately the same area (Wingham et al., 2006).

As can be seen in figure 3.1 the satellite flies in a nose down configuration of 6 °, for maximal stability.

The two parabolic antennae on the front are installed exactly in across-track direction of each other for the interferometric capability.

SIRAL The instrument under attention within this proposal is called the SIRAL. It is a radar altimeter that was specifically designed to increase its capabilities within highly variable topographic areas (Wingham et al., 2006). It is installed on the Cryosat-2, a satellite that has been in operation since 2010, with the aim of determining the fluctuations in Earth's land and marine ice fields.

The instrument operates in three different modes, depending on the overflown area. The mode of interest is the Interferometric SAR (SARIn) mode , which is applied over the coastal or marginal areas. In contrast to

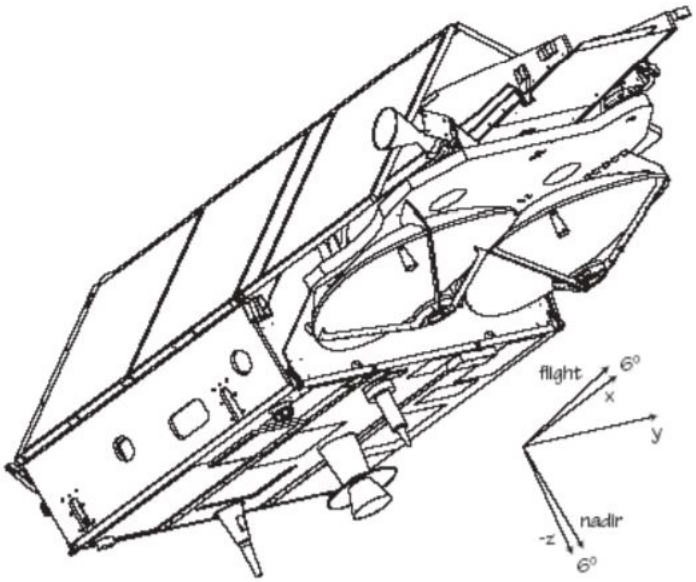

Figure 3.1: Image showing the Cryosat-2 and its attitude [credit: ESA (2012)]

the other modes, the SARIn mode makes use of two antennas, which are mounted on the satellite in across-track direction. One of the two serves as transmitter as well as receiver, whereas the other is used as receiver only (ESA, 2012).

The instrument provides accurate timing for transmission and reception of the signals. Attitude and orbit state information are generated by the dedicated systems on the satellite and are required to determine the range accurately. The instrument's calibration was done partly before launch and partly updated during mission lifetime. The static and dynamic calibration results, as well as attitude and state variables are provided (Scagliola et al., 2016).

The specifics of the instrument, which are essential for the SARIn mode, are shown in table 3.1. All of these parameters will become more clear when continuing reading this thesis.

Carrier Frequency (f_c) [GHz]	13.575
Transmitted Bandwidth (B) [MHz]	350
Transmitted pulse duration (τ_{pulse}) [μs]	49
Pulse Repetition interval (PRI) [μs]	55
Pulse Repetition Frequency (PRF) [kHz]	18.182
Burst Repetition Interval (BRI) [ms]	46.7
Samples per echo FBR ($N_{s,L1b}$)	512
Samples per echo L1b ($N_{s,FBR}$)	1024
Measurement range window [m]	240
Interferometer Baseline (B_I) [m]	1.172

Table 3.1: SIRAL system characteristics specifically for operation in SARIn mode. Values adopted from Wingham et al. (2006).

3.1.2. Radar altimetry processing

A generic scheme showing the steps involved in altimetry data analysis, is shown in figure 3.2. The overall process is divided over three main steps: **Data Collection, Data Processing, and Data analysis**.

The data is collected and processed on-board before it is send to earth. This data collection and the principles behind satellite radar altimetry will be discussed in section 3.2.

After the altimeter has fulfilled its job, the raw signal data, called Full Bit Rate (FBR) data in case of Cryosat-2, is transmitted to ground, where extensive processing is performed to end up with the desired elevation measurements, denoted as Level 2. The processing steps involved from getting from FBR to L2, including the intermediate L1b level, will be further explained in 3.3.

As a large part of this thesis comprises the signal processing, a more elaborate explanation will be given here. As can be seen in figure 3.2 the processing converts the raw satellite FBR data into L1b data. This is done by means of two processes: Delay/Doppler processing in along-track direction and Interferometric processing in across-track direction.

The L1b product results from this processing are further processed, to form the L2 elevations. Different methods exist that transform the L1b products into L2 elevations. In this thesis Swath processing will be applied. The basic concept will be explained in section 3.3.2.

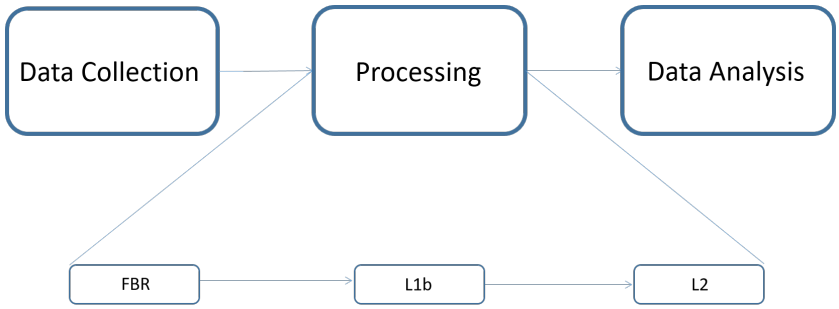

Figure 3.2: Scheme showing the steps a radar signal goes through from satellite to the eventual elevation measurement.

Finally, when the elevations are produced the analysis can start. In this case the analysis will consist of validating the found results, by comparing them to a Digital Elevation Model and to Laser Altimetry data coming from the Operation IceBridge. These aspects will be discussed in section 3.4.

3.2. Data Collection

The lowest level data which is distributed by European Space Agency (ESA) is the Full Bit Rate (FBR) data. This serves as input to the extensive data processing that is perfomed on-ground to produce the elevation.

The FBR data is produced after having undergone on-board processing and applying the required geolocation of the bursts. The on-board processing consists of deramping the received chirps and sampling the resulting signals into the In-phase and Quadrature (I/Q) phase shifted signal components. These steps are fundamental signal processing concepts which will be shortly addressed in this section.

3.2.1. I/Q data samples

Electromagnetic signals are often represented as waves, whose oscillation is characterised by its frequency f or its wavelength λ and the amplitude A. In case of SIRAL, signals are used with the radio (carrier) frequency f_c as shown in table 3.1. These signals show a sinusoidal behaviour as a function of time, and can be described as such, as shown in equation 3.1.

$$s = A\cos(2\pi f t + \phi) \tag{3.1}$$

In which A denotes the "peak" amplitude, ϕ the instantaneous phase angle, f the frequency and t the time.

In signal analysis, these sinusoids are most often represented in its in-phase and quadrature components. This follows from a trigonometric identity, as shown by equation 3.2:

$$A\cos(2\pi f t + \phi) = A\cos(\phi)\cos(2\pi f t) - A\sin(\phi)\sin(2\pi f t) = \mathbf{I}\cos(2\pi f t) + \mathbf{Q}\sin(2\pi f t) \tag{3.2}$$

In which Q and I are defined as shown in equation 3.3.

$$I = A\cos\phi, Q = A\sin\phi \tag{3.3}$$

It is thus shown that a sinusoid as shown on the left hand side in equation 3.2 can be described by two components, with amplitudes I and Q.

Simply stated these I and Q components represent the amplitude and phase of a signal or wave, but in a Cartesian manner. The components can be related to the phase and amplitude, by equations 3.3. This relation is graphically shown in the complex plane by figure 3.3.

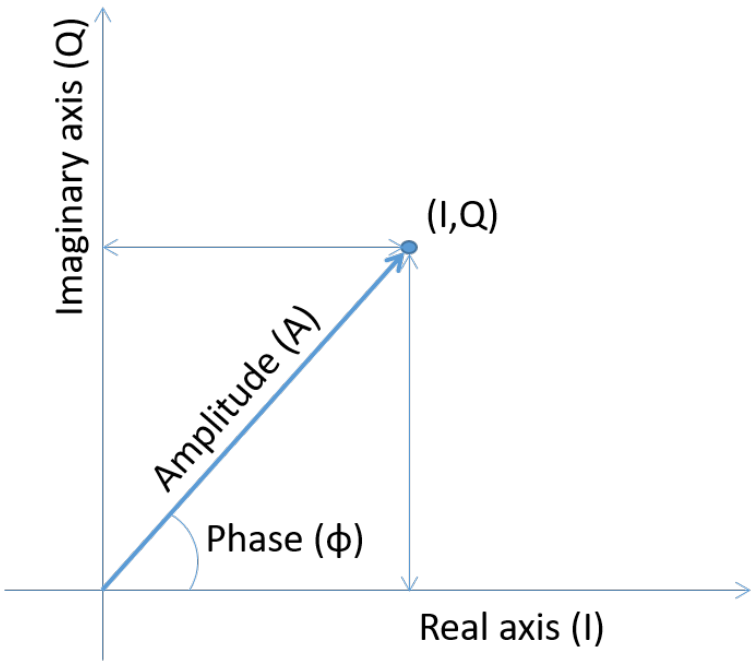

Figure 3.3: The relationship between I/Q samples and Amplitude and Phase is shown in the complex plane.

I/Q data is widely used in signal processing applications. It is used to modulate information on to carrier signals, but can also be used to describe any particular signal that has undergone modulation. In this case the the signal reflected from earth is modulated along the way of transmission to reception. This modulation is expressed in I and Q components.

One major advantage of using the I/Q samples instead of simply representing waves in terms of amplitude and phase is the fact that negative frequencies can be distinguished from positive frequencies. In practice, the I and Q samples are often given as one complex number, as is done in the Cryosat-2 FBR product, as shown by equation 3.4.

$$s = I + Qi \tag{3.4}$$

3.2.2. Chirps

The signals that are transmitted by SIRAL are called chirps. A chirp is a linearly frequency modulated signal. Hence, a signal of which the frequency increases or decreases linearly with time, over a bandwidth or frequency range, as shown in figure 3.4.

In order to achieve higher range resolutions, shorter length pulses are required. Very short pulses are hard to realize, due to the consequential power requirements. By using chirps instead and deramping these signals on reception, this issue is solved, as they allow for a longer pulse time for the same range resolution (Chelton et al., 1989).

3.2.3. Deramping

The chirps are deramped on reception, which means the signals are mixed (multiplied) with a reference chirp on-board and low pass filtered, by means of an Low Pass Filter (LPF).

This concept is shown in figure 3.5. In this figure two linearly frequency modulated signals (red and blue) are mixed. The length of the signals is equal to 3 [s], during which the frequency is increased from 2 to 20 [Hz]. This thus comes down to a chirp rate of K 6 [Hz/s]. The signals are as shown on the top line delayed relatively, by 1 [s].

It is known that multiplying two signals results in a signal comprising frequencies of the frequency differences and the frequency sum of the two input signals. Furthermore, it can be seen that the frequency difference between the two chirps is constant in time. As the signals have the same chirp rate, the relative time delay is related to the frequency difference measured by formula 3.5.

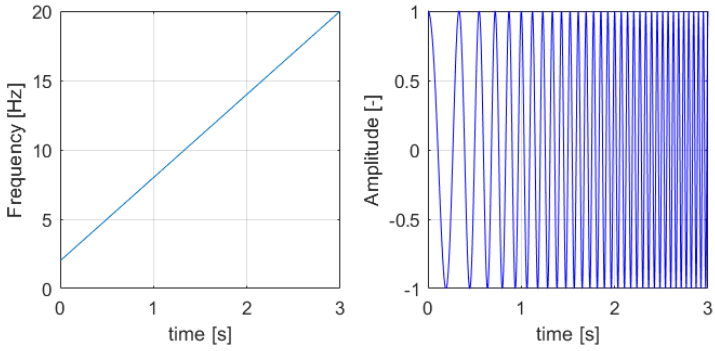

Figure 3.4: An example of a chirp signal, with a Bandwidth B equal to 18 [Hz] and pulse time τ_{pulse} of 3 [s].

$$\Delta t = \frac{\Delta f}{K} \tag{3.5}$$

In which Δf denotes the frequency difference and K the chirp rate.

Hence, the goal of deramping is to find this frequency difference between the two signals, as this leads to the time delay. This is achieved by applying a Fourier transform to the multiplied signal.

The result of applying this Fourier transform to the signals as shown in the top of figure 3.5, is the spectral distribution of the resulting multiplied signal, as shown on the bottom. As can be seen two peaks can be distinguished. One at 6 [Hz] and one distributed peak ranging from around 8 up to 34 [Hz].

Consequently, as only the 6 [Hz] signal is of interest, the signals representing the sums of frequencies need to be filtered out by applying a LPF. This LPF filters out all signals that are of frequency higher than a certain limit.

In order to simplify this filtering, the large carrier frequency to bandwidth ratio shows to be beneficial. This is shown by the 4 plots on the right of figure 3.5.

These figures show the case in which two signals, with higher mean frequencies are mixed and thus represent the case in which a large carrier frequency is used. The resulting spectral distribution shows the same peak at 6 [Hz]. However, the frequency span which represents the sum of frequencies is located at a much larger frequencies. This simplifies the LPF design, as a large range of values can be chosen.

The case on the right thus shows that using a high carrier frequency to bandwidth ratio, is beneficial for filtering out the lower frequency signal, which represents the relative time delay of the two signals. This is the case for SIRAL, where the Carrier Frequency f_c (13.575 [GHz]) is much larger than the bandwidth B (350 [MHz]).

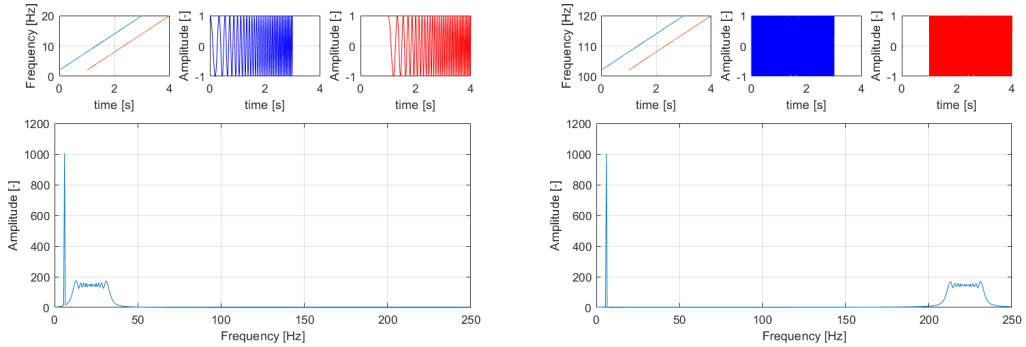

Figure 3.5: Graphical display of the manner in which deramping works. Two cases are shown, of which the one on the left shows two signals with a carrier frequency close to zero, and one with a relatively large carrier frequency to bandwidth. In both cases the bandwidth is equal to 20 [Hz]

Eventually, a 6 [Hz] signal is the result of the experiment shown above. This 6 [Hz] frequency difference, translates to the 1[s] delay in signals by applying formula 3.5. Thus, this shows that deramping results in Continuous Wave (CW) signals of which the frequency is proportional to the range (Raney, 1998).

Ensemble of scatterers In practice the situation is a little more complex. Not one signal returns at the satellite at one time instant, but a set of signals simultaneously, for which the range from surface to satellite is the same. The resulting sampled signal thus represents a summation from all received signals at the same time instant, and thus with the same frequency (Chelton et al., 1989).

The more signal return that is present the higher the power of the return signal. The power of the return signal is thus proportional to the area of the footprint and the amount of integration performed (Raney, 1998).

3.2.4. SARIn mode SIRAL

When in SARIn mode the SIRAL instrument operates in a "closed" burst arrangement. This means that 64 of these chirped pulses are transmitted within one burst, as is graphically displayed in figure 3.6. The collection of chirps is transmitted over a period of time that is shorter than the return time of the signal, after which a period follows in which all of the chirps are received. In case of SIRAL the chirps are interleaved with a short interval of around 6 [μs]. Furthermore, after transmission, a short period of time trespasses until the first transmitted signal is received. The length of this period depends on the return time, and hence the range to surface.

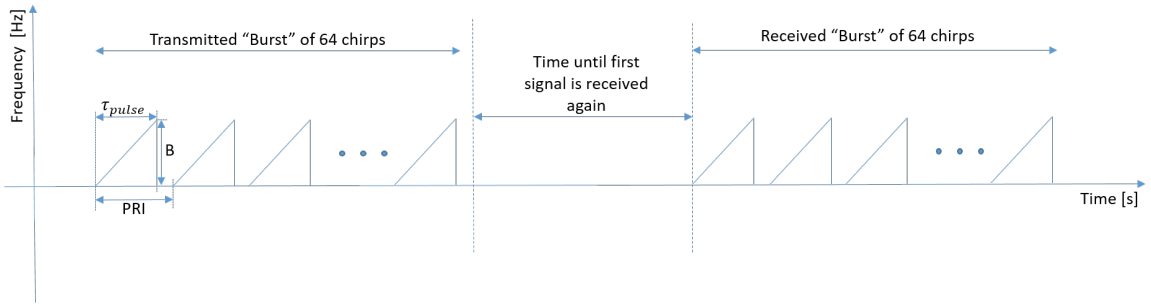

Figure 3.6: A burst as transmitted and received by SIRAL, with the corresponding timing and frequency labels of which the values can be found in table 3.1

In the particular case of the SARIn mode, the burst of chirps is followed by a set of lower bandwidth signals (40 [MHz]), as can be seen in figure 3.7. These signals are used for tracking control. In essence, these signals help predict the range to surface from the satellite for accurate timing of the deramp signal.

After deramping, the resulting signals are sampled into their I/Q data points.

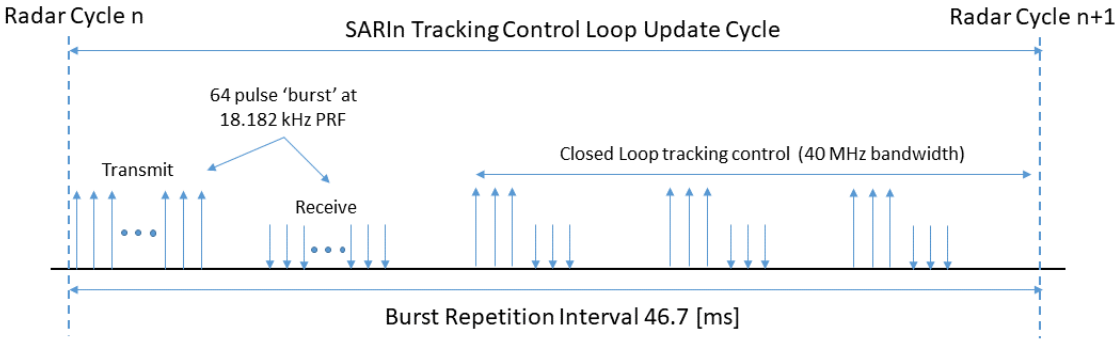

Figure 3.7: The closed-burst pulse timing within tracking control loop shown for the SARIn modes. (Wingham et al., 2006)

3.2.5. Geolocation

The geolocation of the raw telemetered data is based on the output of the Doppler Orbitography and Radio positioning Integrated by Satellite (DORIS) system and the star trackers (ESA, 2012). The exact derivation and essentials involved in the geolocation is not part of this thesis, and will not be addressed further. However, it is important for further understanding, to specify the exact meaning of the location of the bursts.

The fact is that the geolocation of the bursts is based upon the "Stop-and-Go" assumption. This means the location of the burst is assumed to be centered in between the location of transmission and the location of reception (Wingham et al., 2006). The burst location is the mid-point of these pulse locations as shown in figure 3.8. Only one location per burst is thus present. Thus, each burst of data is given one position. The pulses are not separately geolocated.

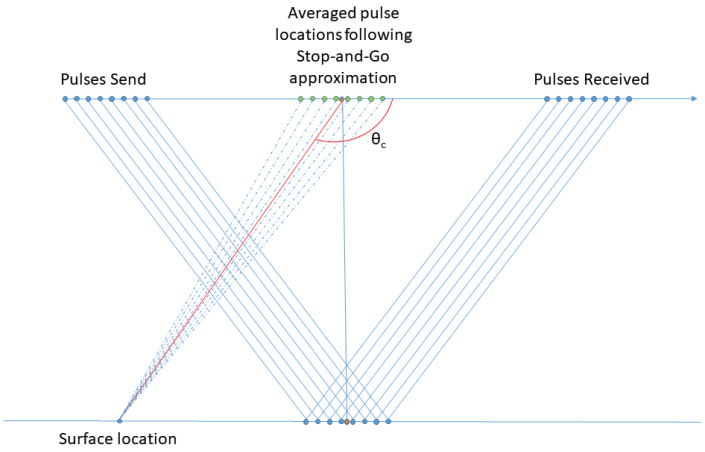

Figure 3.8: Graphical representation of stop-and-go assumption regarding geolocation of burst

3.3. Data processing

After the geolocation, the FBR data consists of matrices of 512 times 64 I/Q deramped time domain signal samples per burst location, as can be seen in figure 3.9. This is the data that serves as the input to the processing as applied in this thesis, and which is distributed by ESA as the lowest level of data available.

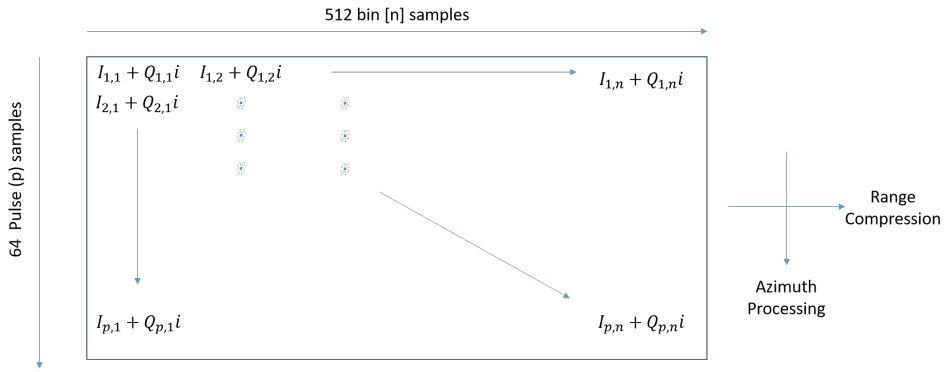

Figure 3.9: The matrix of complex data which is the SIRAL FBR dataset that serves as input to the on-ground FBR to L1b processing. Two of these FBR matrix datasets are produced within SARIn mode. Within this processing the two main steps, Azimuth processing and Range Compression are performed by means of FFT. The FFT directions are shown on the right.

The processing involved in producing surface heights from the geolocated FBR SARIn data, and the processing that will be performed in this thesis, consists of two main steps:

- The FBR to L1b processing

- The L1b to L2 processing

The first step consists of specific processing related to the SARIn mode on Cryosat-2. These steps are D/D (Delay/Doppler) processing, also known as SAR processing, and the interferometric processing. The second step relates to the Level 2 (L2) elevation determination, in this case Swath Processing.

3.3.1. FBR to L1b processing

As explained before the FBR data as provided by ESA consists of geolocated and dated bursts of 512 by 64 I and Q data samples in the time domain. In case of SARIn mode two of these packages per location, one for each receiver channel, are provided.

More data is provided in the data product. The entire list of enclosed data can be found in one of the Cryosat Specification Format documents (Mantovani, 2015). Examples of extra information are orbit altitude, error flags or correction values.

This data serves as input to the next step, the lower level processing or the FBR to Level 1b (L1b) processing. The FBR to L1b processing includes a sequence of steps that originate from conventional pulse-limited altimetry processing and Delay/Doppler (SAR) processing. The conventional pulse-limited steps will be explained first, followed by the basics of Delay/Doppler processing.

Pulse Limited altimetry Pulse-limited altimetry denotes the type of altimeters of which the footprint size in along-track and across-track direction is limited by the pulse-length of the signal (see left figure 3.12).

The same processing is applied as is outlined in section 3.2. By deramping the received chirps, a frequency spectrum can be produced, of which the frequency is proportional to the range delay. This process of converting the deramped chirps into to the frequency spectrum, is known as range compression. The resulting product is a power versus frequency waveform, as shown in figure 3.18. In order to reduce noise over the waveforms, a set of waveforms are often averaged, also known as multi-looking.

This multi-looking is required, as single waveforms often consist of a lot of speckle noise. Speckle noise is caused by the fact that an area is illuminated by the antenna and not a point on the surface. An ensemble or distribution of scatterers is thus received at the antenna. The noise arises due to constructive and destructive interference of this distribution of signal waves at the receiver, which is dependent on the relative phase of the different waves. This is an undesirable effect which arises from the fact that SAR altimetry makes use of phase coherence (Rees, 2012). The speckle behaviour changes when the geometry with respect to the resolution cell changes. Hence, by averaging different looks on the same surface patch, this behaviour can be reduced.

Cryosat-2 employs this type of altimetry as well, and is known as the Low Resolution Mode (LRM). In this mode the power waveforms are produced by deramping and range compression. Consequently, 91 consecutive power waveforms are averaged over, to form the eventual power waveform (Wingham et al., 2006).

Delay/Doppler (SAR) Processing Delay/Doppler processing, as part of the SARIn mode of Cryosat-2, applies these steps as applied in pulse-limited altimetry as well. However, additional processing is applied in along-track direction before the range compression. The Delay/Doppler processing was presented first by Raney (1998) and serves as an improvement to the pulse-limited radar altimeters.

Within Delay/Doppler processing the main antenna beam is divided into smaller sub-beams, in along-track direction, as is graphically displayed in figure 3.11. The main beam can be divided over the sub-beams by the fact that all sub-beams are experiencing a different Doppler shift. This variation of Doppler shift over the beam is related to the scatterer direction, by equation 3.6 (Rees, 2012).

$$f_r - f_t = \Delta f = \frac{2|\vec{v}_s| \sin\theta_l}{\lambda_c} \tag{3.6}$$

In which f_r [Hz] and f_t [Hz] denote the received frequency and the transmitted frequency, $\vec{v}_s$ [m/s] the satellite velocity, θ_l [Deg] the angle between the scatterer direction and the line to surface perpendicular to the velocity vector as shown in figure 3.10, and λ_c [m] the wavelength of the carrier signal.

Due to the closed burst approach as employed by SIRAL, it becomes possible to sample this frequency shift 64 times, as this are the amount of pulses within a burst. 64 samples translate to 64 FFT bins, and hence a spectral distribution consisting of 64 separate frequency steps. These frequency steps are of size PRF/64 [Hz] (Raney, 1998) (PRF [Hz] is the Pulse Repetition Frequency, 18.182 [KHz] in case of Cryosat-2). As a result 64 subbeams are created each divided by an equal angle θ [Deg]. This angular resolution can be derived from

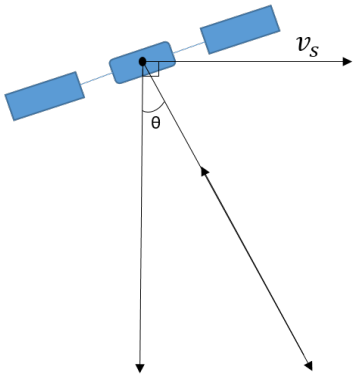

Figure 3.10: The angle θ is shown as the angle between the line pointing to earth perpendicular to the velocity vector, and the direction of the scatterer. The line perpendicular to the velocity vector is not necessarily equal to nadir.

equation 3.6, knowing the Pulse Repetition Interval PRI [s] is the inverse of PRF [Hz] and 64 times PRI [s] is the exact duration of one burst τ_B [s]. This is shown in equation 3.7 (Cipollini, 2016).

$$\theta = \arcsin(\frac{\lambda_c}{2|\overline{v}_s|}\Delta f) = \arcsin(\frac{\lambda_c}{2|\overline{v}_s|}\frac{PRF}{64}) = \arcsin(\frac{\lambda_c}{2|\overline{v}_s|}\frac{1}{64PRI}) = \arcsin(\frac{\lambda_c}{2|\overline{v}_s|\tau_B}) \tag{3.7}$$

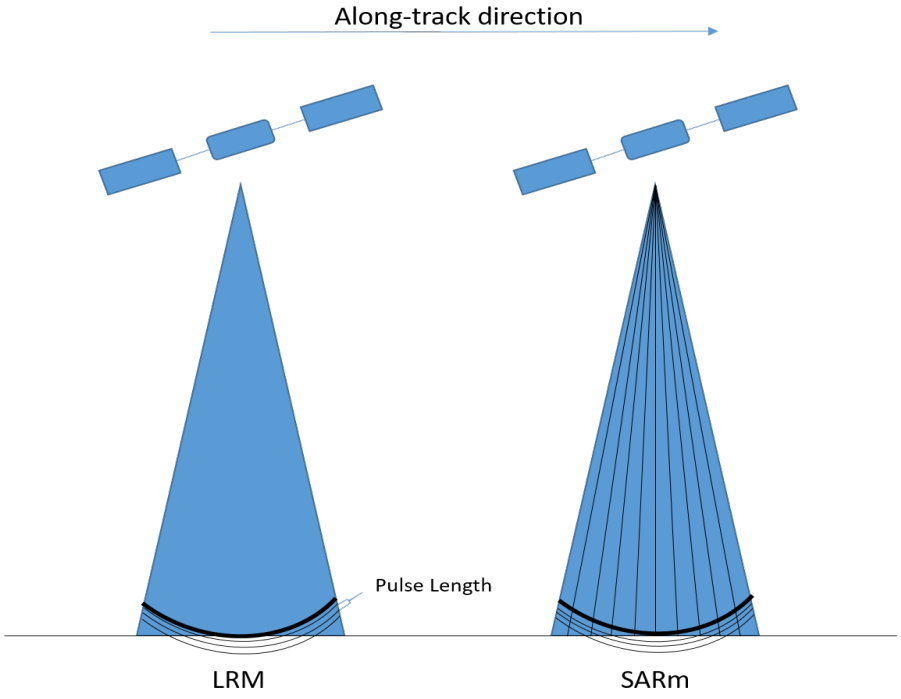

Figure 3.11: The difference between the Pulse Limited radar beam (LRM in case of Cryosat-2) and the Delay Doppler (SAR mode in case of Cryosat-2) beams. As can be seen the main pulse-limited beam is divided into several sub-beams in along-track direction.

As a result of Delay/Doppler processing the footprint changes in along-track direction compared to the pulse-limited altimeter footprint, as is shown in figure 3.12. While in across-track direction the footprint size still remains pulse-limited and thus dependent on the pulse length, the along-track footprint length is a function of system constants and design choices as the PRF, carrier wavelength λ_c and altitude of the satellite, as can be seen from equation 3.7. This resolves the along-track ambiguity that pulse-limited altimeters suffer from. Signals coming from the front or aft in along-track direction can be distinguished now. As can be seen the across-track ambiguity remains. The signal corresponding to one particular sampled Doppler shift, or Doppler cell, corresponding to the same time delay, can originate from two possible source locations in across-track direction, as is shown in 3.12.

Furthermore, it should be noted that in case of Pulse-Limited altimetry, as in LRM for Cryosat-2, multiple single pulse footprints, as shown in figure 3.12 on the left, are averaged to form the multi-looked waveform. This eventually causes the footprint to be of elliptical shape elongated in along-track direction. This elongation does not occur in case of Delay/Doppler processing, where the multi-looking is performed at synchronized locations (Raney, 1998).

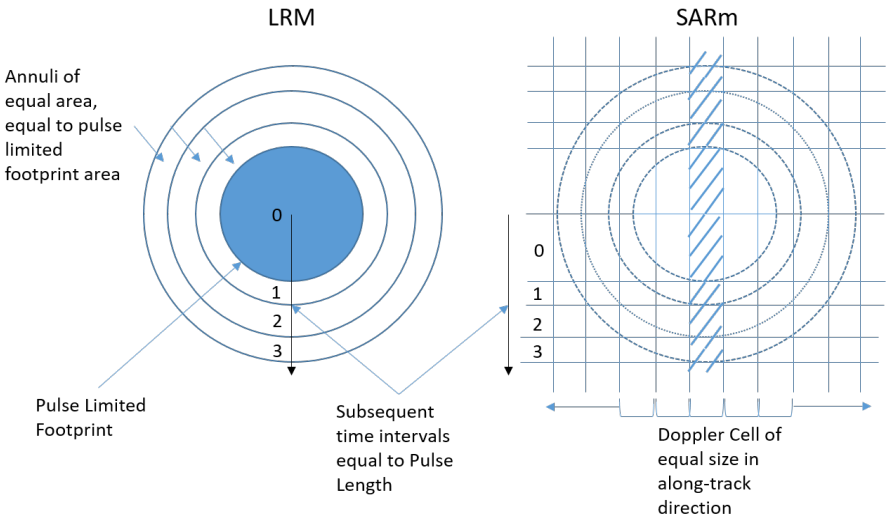

Figure 3.12: Differences in footprints between Conventional Altimeters and Delay/Doppler Altimeter (Raney, 1998)

In practice Delay/Doppler processing consists of applying four steps in addition to the steps required for pulse-limited altimetry, which are all applied during on-ground data processing.

- Beam Forming
- Surface location computation
- Beam Steering
- Delay compensation

The **beam forming** process produces the set of 64 sub-beams in along-track direction as shown in figure 3.11. The processing involved, utilizes the known phase delay over burst time (Kleinherenbrink et al., 2014).

This phase delay originates due to the satellite along-track velocity, during burst reception. The concept is most easily explained by considering single scattering locations.

For example, a scenario is shown in figure 3.13 on the left, considering strong scatterers with respect to the radar in along-track direction (Rees, 2012). As the radar flies over the scatterer the distance between scatterer and radar changes. This variation in range can be translated into a variation in phase sampled at the receiver over time. The phase change as function of along-track satellite location x is shown on the top right of figure 3.13 for two scatterers located at different locations within the along-track path. The change of this phase change over time is the Doppler frequency experienced by the radar. The corresponding Doppler frequencies as function of x are shown on the bottom right of figure 3.13). As can be seen from the two Doppler frequencies, different Doppler frequencies are experienced at the same along-track position of the radar for both scatterers. Signals scattered from different along-track surface locations can thus be distinguished by their Doppler frequency. The entire process is known as beam forming, as different sets/beams are produced pointing to different along-track Doppler cells.

As stated before, a signal is composed of an ensemble of scatterers inside the radar footprint. In order to distinguish the different frequency components of this ensemble a multiple of samples is required. This multiple of signal samples is provided by the 64 pulses within a burst, which produce 64 along-track beams. The sorting of the frequencies is performed by means of a Fast Fourier Transform (FFT), in the direction of the 64 pulses, and is thus known as the along-track FFT, as is shown in figure 3.14.

In order to reduce noise over the measurement, the SARIn waveforms produced by Delay/Doppler processing are multi-looked, similar to multi-looking in pulse-limited altimetry . This means that waveforms

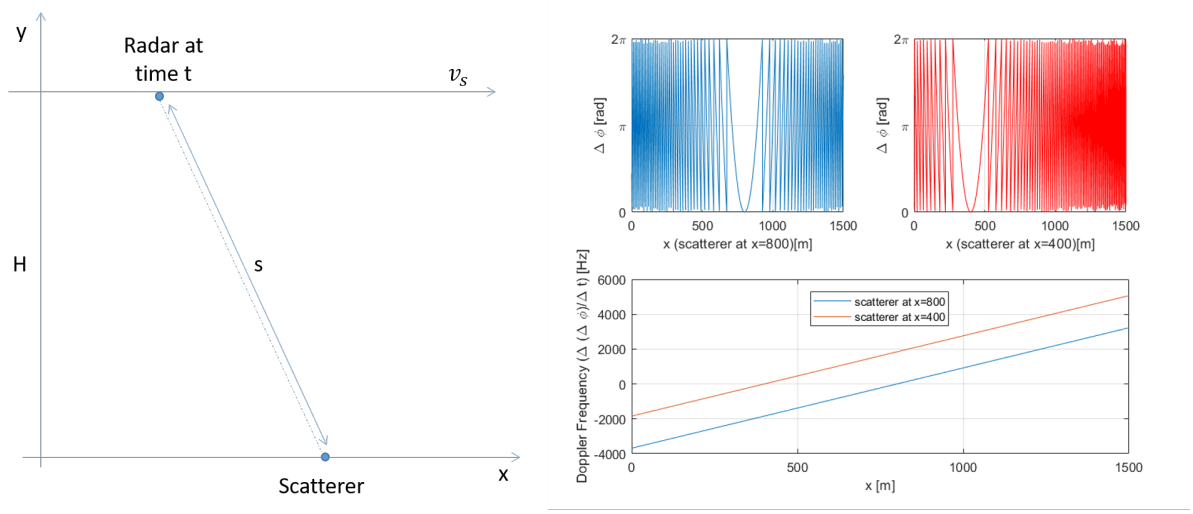

Figure 3.13: Single strong off-nadir scatterer in scenario as shown on the left, makes for a differential phase (top) and frequency over time (bottom) behaviour as shown on the right.

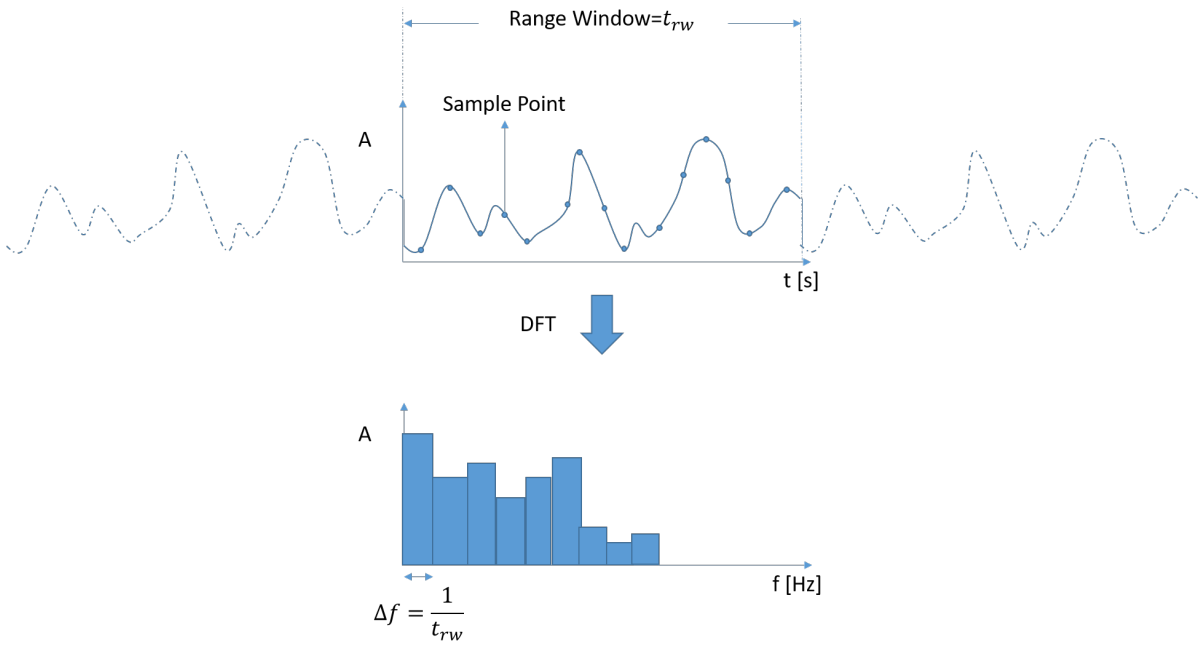

Figure 3.14: The samples of the ensemble of scattered signals are transformed into the Frequency domain by means of a FFT.

corresponding to the same surface location but to different bursts are accumulated and averaged. However, the 64 beams that are produced in the beam forming step are located relative to the corresponding burst location. The locations the beams point to on the surface differs between bursts and do not overlap.

In order to make the surface locations to which the beams are pointing overlap, **surface locations** are defined beforehand, based on the theoretical along-track resolution, as defined in equation 3.7. For Cryosat-2 this along-track resolution is equal to ~0.3 [km]. The beams originating from different bursts can now be steered towards these surface locations, by means of **beam steering**. This is done, to be able to accumulate the different waveforms from different bursts. A graphical representation is shown figure 3.15.

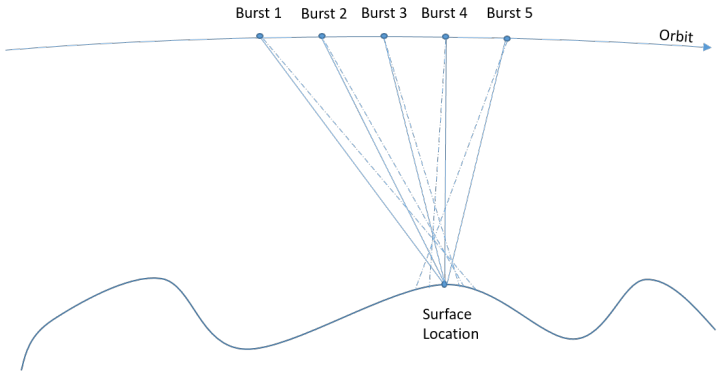

Figure 3.15: A schematic representation of Beam Steering. As can be seen the beams which are pointing at different locations are focused towards the desired surface location.

Beam steering is achieved by altering the differential phase over time, that arises due to the velocity relative to scatterer location, which was discussed previously. By increasing or decreasing the slope of the phase difference over received pulses within a burst, the beam is steered. The additional phase ramp is a function of the location to which the beams need to be steered and the distance in between the pulses per burst. The distance in between the satellite pulse locations is known. The surface locations are to be determined beforehand for the entire orbit. In this way all the beams from the different bursts can be steered accordingly.

It is easily shown that beams originated from different bursts travelled different ranges to the same surface location, as shown in figure 3.16. The **delay compensation** or Slant Range Correction (SRC) is applied to correct for this effect. The difference in range travelled is calculated by comparing the slant range to the range from the surface location to the location in orbit exactly nadir to that same surface location.

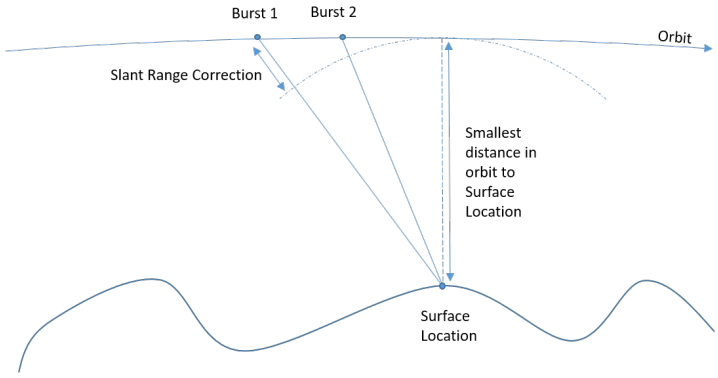

Figure 3.16: A schematic representation Slant Range Correction or Delay Compensation

Additional to the delay compensation as presented by Raney (1998), two more geometric corrections are applied, which are a Doppler correction and Window Delay Correction Window Delay Correction (WDC), which will be discussed in the following chapter.

Interferometric Processing As previously explained, the along-track ambiguity is solved by means of D/D processing, however an across-track ambiguity remains. Signals arriving with the same relative delay time can originate from two source locations located perpendicular to the sub-satellite track. A solution for coping

with this ambiguity is solved by interferometry. This capability is made possible by the two antennae installed next to each other in across-track direction for the Cryosat-2.

This configuration makes it possible to determine the across-track direction of scatterer location (Jensen, 1999) in case an across-track slope is present. This across-track angle is derived from the phase difference which is measured between the two receiver channels. The phase difference arises due to the difference in across-track scatterer range from one antenna compared to the other, as is shown in figure 3.17.

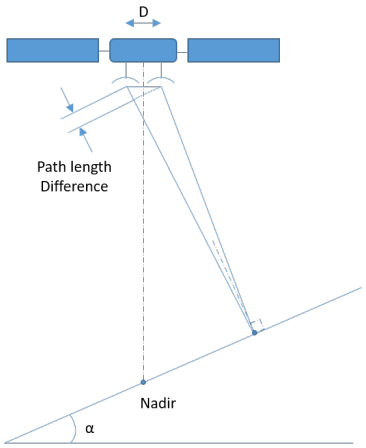

Figure 3.17: Geometry involved in interferometric capability of Cryosat-2 (Jensen, 1999)

As a quality indication for the phase difference measurement an additional value is calculated: Coherence. The coherence value represents the correlation between the two signals measured at the two receiver channels. The correlation between the two channels is affected by uncorrelated noise, consisting of thermal receiver noise and speckle (Jensen, 1999). Speckle arises due to the difference in viewing geometry for both channels, whereas thermal noise is an inherent noise to electronic devices, which is quantified by the Signal-to-Noise Ratio (SNR). The coherence values span a range from 0 to 1. The higher the coherence value the higher the correlation between the two measured signals.

L1b Product The L1b product mainly consist of power, phase difference, and coherence over bin waveforms. This means that for every sample bin, which represents a range time, a power, coherence and phase difference value is available.

An example of a power waveform is shown in figure 3.18. The waveform consists of a leading edge, where the power increases and a trailing edge where the power decreases. When the echo is not yet received, the power waveform shows a background noise level.

The sample bins represent discrete moments in time. In case of SIRAL one sample bin represents 3.125 [ns] in time. The SIRAL instrument attempts to set the timing of the receiving window, which in case of SARIn mode, is of a size of 512 samples, exactly at the moment where the signal is to be received. This timing of the range window is defined as the window delay. The window delay represents the exact two-way timing from transmission to the centre range window bin. In case of SARIn mode this is the 255th bin.

3.3.2. L1b to L2 processing

The L1b product still does not provide us with clear range information. In order to derive the surface heights the L1b to L2 processing is to be applied. Within this thesis the range is derived from the L1b power waveforms by applying Swath Processing.

Retracker The peak power of the return signal can differ in location within the range window. As such, for every waveform a sample bin needs to be picked to represent the exact timing of the received signal. After picking the right point on the waveform, the two-way signal time can be determined by correcting the window delay.

The process of picking the sample within the waveform is known as "retracking". Different types of retrackers are used in literature (Davis, 1997), all having their own advantages and specialities.

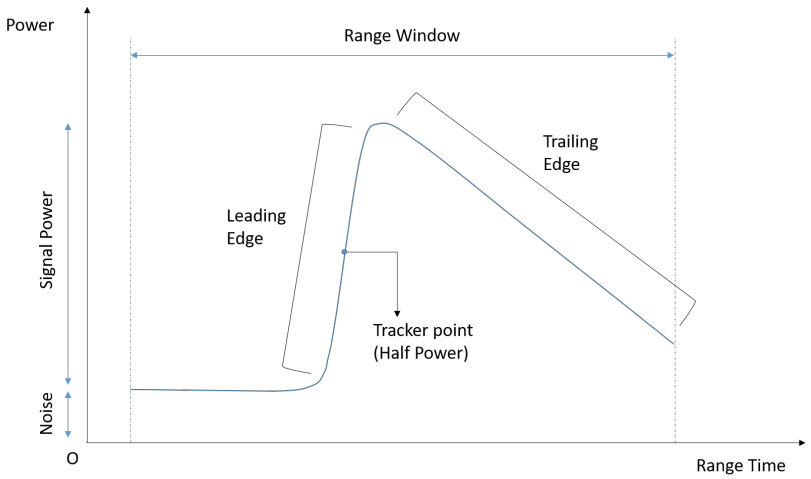

Figure 3.18: The power waveform and its characteristics

Swath Processing Swath processing can be seen as a certain type of retracker. Swath processing takes as input the L1b SARin waveforms as produced in the FBR processing. Similarly to conventional retracking, waveform samples are picked that will be used for elevation determination. In conventional retracking samples are chosen based on the peak power within the waveform. Samples that are located at the leading edge of this peak are picked based on their power level with respect to this peak. In Swath processing this is not the case. The samples that are deemed fit for elevation determination are picked out from all over the waveform, based on different criteria. The filter criteria mostly used are phase coherence, and power level (Gourmelen et al., 2017).

Swath processing makes use of interferometric phase of the signals. As can be imagined the first signal return at satellite is from the Point of Closest Approach (POCA) measurements, representing the shortest range. By making use of the interferometric two-antenna receive capability of a satellite, the differential phase corresponding to the POCA return can be determined and consequently the angle of arrival as stated before. The signal returns that follow after the POCA return have longer delays and hence represent locations that are located further from the satellite than POCA. Furthermore, these returns represent the surface scattering from both sides of the POCA. In flat surface returns, hence returns from surfaces that are perpendicular to satellite nadir, signals from equal spatial (across-track) distance from POCA, will have equal delay times. As these returns have equal delay times the across-track direction from which they originate, "left or right", can thus not be determined, as no trivial solution is present.

However, things change when there is a surface slope present underneath the satellite. As this slope of a sub-satellite surface increases, the POCA moves outwards of the main footprint (see figure 3.19). Hence, the POCA will be located further from the sub-satellite track when surface slopes are larger. When the POCA is located outside of the main beam as represented in figure 3.19 all of the returns will be coming from the main beam, which is located entirely at one side of the POCA.

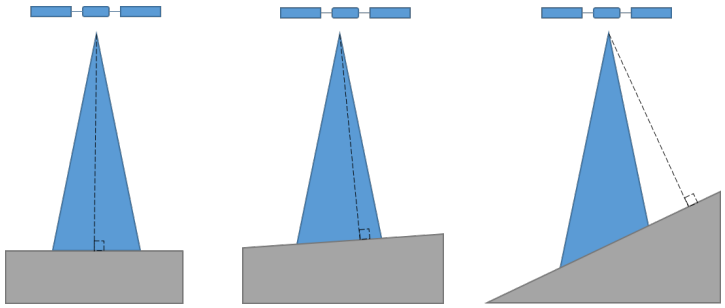

Figure 3.19: Simple representation of geometry involved in Swath Processing. Dotted line represents range from satellite to POCA.

However, figure 3.19 oversimplifies the situation. The antenna beam cannot simply be represented by a triangle. The beam shape is described by the antenna gain. This gain describes the directivity of the antenna

transmit power. The main beam is often defined by the angles at which the power transmitted has dropped to half of the maximum power, the -3 [dB] gain points. Moreover, side-lobes are present in the antenna gain pattern, as is the case as well for the parabolic antennae on the Cryosat-2. Side-lobes are undesired local optima within the antenna gain pattern, which occur at angles which deviate from the main beam direction.

After POCA signal reception, consequent signal returns will originate from both sides of the POCA in case of significant surface slope. The signal returns that return from the nadir side of the POCA are expected to be of higher power, compared to the signal returns from the other side of POCA. This is due to the higher power gain in nadir direction. Assuming that this power difference is large enough, the signal returns are thus expected to be dominated by returns from one unambiguous side of the POCA, and can thus be used for a range measurement, and consequent elevation determination.

L2 Product The result from retracking or swath processing are the Level 2 (L2) elevations. These elevations are defined as the distance between the World Geodetic System 1984 (WGS-84) reference ellipsoid and the point on the surface in meters. Along-side the elevations, the locations are provided as well.

3.4. Data Analysis

From the L2 elevations different analyses can be performed. Height change over time datasets, as well as Digital Elevation Model (DEM) can be produced.

In this case, the analysis will only comprise the validation of the product itself with an external DEM, the Greenland Ice sheet Mapping Project (GIMP) DEM (Howat et al., 2014), and with other elevation data, namely the airborne laser altimetry data. This section will give an insight in the exact specifics of these datasets. Furthermore, an essential part in analysing the elevation measurements is the interpretation. As the different datasets originate from different sources, with each their own characteristic surface or atmospheric interaction, the differences need to known. Similarly, within the coastal regions the surface types differ. The density of the ice or snow might differ which can cause an alteration of the return signal.

3.4.1. Validation

In the scope of this thesis the data analysis mostly comprises a validation of the produced elevation dataset with different datasets. These datasets are the GIMP DEM and the airborne laser altimetry data from the operation IceBridge (IB). These datasets will be addressed in this section.

Greenland Ice Mapping Project (GIMP) The GIMP has been concerned with producing high quality benchmark datasets, which all have the aim of contributing to the research into ice sheet change. Three different datasets are provided: a 15 [m] resolution image mosaic, consisting of Landsat-7 and RadarSat-1 data, ice-covered and ice-free terrain masks, at the same resolution, and a 30 [m] resolution digital elevation model (Howat et al., 2014).

The digital elevation model has been produced by combining different DEM's, and co-registering them to combined Ice, Cloud, and land Elevation Satellite (ICESat) laser altimetry data. It is important to note that the newest GIMP DEM comprises ICESat data collected over the period January 2009 and December 2015.

Operation Icebridge Operation IceBridge is a NASA airborne mission with the main goal of validating the laser altimetry data as produced by the past ICESat and upcoming ICESat-2 mission. The data is freely provided and can be downloaded over the region of interest.

The instrument that is used is the Airborne Topographic Mapper (ATM), which consist of a LIght Detection And Ranging or Laser Imaging Detection And Ranging (LIDAR). The LIDAR makes use of pulsed green laser and the geolocation is determined by means of Global Positioning System (GPS). The operating altitude of the mission is in between 500 to 750 [m]. At these altitudes the laser footprint area is equal to approximately 1[m] in diameter. The ATM produces measurements with a vertical accuracy and precision of 6.6 [cm] and 3 [cm], respectively. The horizontal accuracy and precision are 74 [cm] and 14 [cm], respectively (Martin et al., 2012).

3.4.2. Interpretation

When comparing the radar altimetry data from Cryosat-2 the differences between the different datasets need to be known, in order to give a just interpretation. Different signal types exists as well as different states of ice, which all have an influence on the signal to surface interaction.

Radar vs. laser Where Radar altimetry makes use of radio waves, Laser altimetry makes use of Laser: Light Amplification by Stimulated Emission of Radiation. Laser light is light that is highly focused due to its small divergence angle. Small footprints can be achieved due to this small beam divergence. Moreover, due to this narrow beam-width the measurements are not highly dependent on surface slopes. In combination with the capability of focusing a high amount of energy on this smaller footprint, within a short length of time, laser shows benefits over the more conventional methods of Radar altimetry.

However, Radar Altimetry shows benefits over Laser Altimetry (Wingham et al., 2006). Due to the relatively large wavelengths used in radar altimetry, the measurements suffer less from weather interference (Quartly et al., 1998) with respect to measurements obtained by laser altimeters, which are disturbed by clouds and affected by drifting snow (Helm et al., 2014). Furthermore, as the beam-width of the radar altimeter is relatively big with respect to laser altimeters, they are less sensitive to mispointing errors. As the pulse expands spherically, while it propagates from satellite to ground, the point of closest approach, the nearest point to satellite, is of high chance to be still located in the main beam-width of the radar altimeter. Only when the pointing error becomes bigger than half of the beam-width angle errors will be introduced (Fu and Cazenave, 2001).

The signal of the radar interacts with the surface off which it scatters. In case of snow and firn, radar signals mostly do not reflect of the top of the surface but on a deeper level (Simonsen and Sørensen, 2017) (Scott et al., 2006), whereas laser mostly scatters at a level closer to the real surface. The signal penetrates to a certain depth into the snow. The penetration depth is dependent on the wavelength of the signal and is mostly denoted as the ratio between subsurface and surface scattering or the Volume to Surface scattering ratio. The volume scattering is the return signal that comes from subsurface scatterers.

4

Methodology

The knowledge of the related background, makes it possible to apply the FBR to L2 processing. The steps involved will be described into detail here. Firstly, all the steps required for SARIn FBR to L1b processing are presented, followed by an outline of the steps involved in Swath processing. Finally, the validation strategy will be discussed.

4.1. Development of the SARIn FBR to L1b processor

The SARIn FBR to L1b processor is based upon a Cryosat-2 SAR MATLAB processor as developed by Cornelis Slobbe from TU Delft Civil Engineering (Slobbe et al., 2016). This processor is based on the steps described in the SAR Altimetry Coastal and Open Ocean Performance (SCOOP) document(Cipollini, 2016). As the SAR mode, is mainly used over oceanic areas, the processing steps are based upon this fact. This means large variations in topography are not taken into account.

The FBR to L1b processor for the SARIn mode differs from the SAR mode processing in the fact that two antennas are used instead of one. This means that all the steps involved in SAR processing needed to be duplicated. Moreover, additional variables are determined: the phase difference and the coherence. Of these two variables the phase differences requires additional calibration.

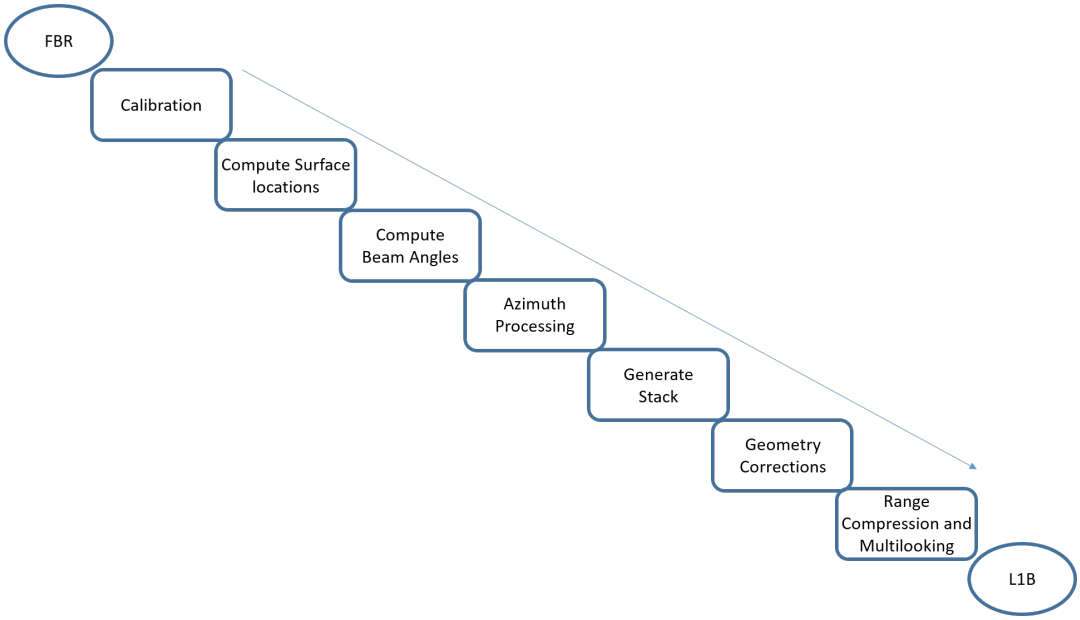

Figure 4.1: Steps involved in Delay/Doppler processing

.

Three steps are not presented in figure 4.1 which are the acquisition of data, and the initialization and finalization of the FBR to L1b processor.

Data acquisition The acquisition of the data was performed by a separate derived Python script. The data is distributed in two files per orbit: an HDR and a DBL file. The HDR file does not contain any measurement data, apart from the location of the measurements, and are hence small files. The HDR files are used to locate the datafile and see if it is contained in the area of interest. If so, the accompanying DBL file would be downloaded. In this way, one prevents having to download all larger DBL files.

The period over which the data is collected covers March, April and May 2017. This period was chosen as it is avoids periods with rapid melting and precipitation, and the ice extent can thus be considered constant over time (Gourmelen et al., 2017). The year 2017 was chosen as this was the most recent dataset available at the beginning of this thesis.

Initialization and finalization The SARIn processing steps involved are shown in figure 4.1. The initialization and finalization steps are dedicated to the reading and writing of the product files. The reading of the data is made possible by a MATLAB script as provided by ESA. This script writes all essential information into a MATLAB struct, for easy access and further processing. The constants that are required within the subsequent calculations are loaded in the initialization as well as the DEM corresponding to the area of interest. In the finalization auxiliary data is copied to the resulting data structure. These auxiliary products include the Geophysical Corrections which are to be applied in the L1b to L2 processing, as well as correction and error flags, and stack characterization parameters.

4.1.1. Calibration

The status of SIRAL is continuously monitored. A wide range of calibration data is collected to see how the instrument is changing over time (Fornari et al., 2014). The resulting calibration corrections are provided by ESA.

Two types of Calibration are performed: internal and external. The internal calibration deals with imperfections within the instrument, whereas the external calibration makes use of a ground transponder to correct for overall errors in range, the corresponding datation and interferometric baseline.

The internal instrument calibration is performed in-flight. The calibration corrections can be divided as follows

- CAL1: In this mode a direct connection between transmitter and receivers is used to calibrate for internal path delay and power gain variation. This is done for both receivers in case of SARIn mode. Furthermore, the pulse-to-pulse phase and power gain variation is calibrated in this mode as well. These latter effects are a result of hardware effects arising from power-up of the transistors at the start of each burst.

- CCAL1 (Complex CAl 1): In this mode corrections are determined for the biases induced by the Automatic Gain Control (AGC) that is used to keep signal level as constant as possible. The calibration consists of a gain correction for both receiver chains and a phase difference correction between both receiver chains.

- CAL2: Within this mode a Low Pass Filter correction mask is provided, that is produced by measuring the noise power in absence of transmission.

- CAL4: Calibration of the interferometer for the phase difference between the two receiving chains. CAL 4 is not a separate mode in contrast to the others, but interleaved in the SARIn measurements at a rate of 1 [Hz]

Calibration corrections differ in the fact that some of them are (on average) static over lifetime, whereas other need updating during lifetime. The calibration corrections which are static, are provided externally within the so-called Cryosat Users Characterization (CUC) file. The other calibration constants are provided within the FBR data product. The manner in which the calibrations are to be applied can be found in Scagliola et al. (2016), and will thus be not further discussed in this section. It should be noted that all calibration corrections are required to be applied for both channels.

Phase Cross Calibration In contrast to SAR mode data processing the phase difference is calculated between the two antenna signals. A phase cross-calibration is applied to correct for the phase differences that arise over the different receiver paths (Fornari et al., 2014).

No instructions were found for the Phase Cross calibration. The phase cross calibration is presented as consisting of two parts (Galin et al., 2013): the CAL1 and CAL4 phase difference calibration.

In case of the CAL4 calibration the satellite is put in a dedicated operational mode to measure this phase difference. When in this mode, the satellite does not transmit any signals. An attenuated connection between transmitter and receiver is used to achieve this. The phase difference is determined by applying the same procedure as is used for the interferometric phase difference, as will be shown in section 4.1.7.

The CAL4 echoes can be distinguished from the normal echoes by their CAL4 flags. In contrast to the other Calibration measurements the CAL4 measurements are performed during SARIn operation at a rate of 1 [Hz]. As a consequence, an interpolation is required to provide the CAL4 phase difference correction to all echoes. After the correction has been calculated and applied, the CAL4 echoes are removed, as to prevent them to affect the eventual waveform production.

The CAL1 phase cross calibration is not applied in this thesis, as the exact method of application remains unknown. This is to be researched in future work.

4.1.2. Compute Surface Locations

In the next step the beam angles per burst are calculated. As the beam angles will point to different surface locations for different burst locations, predetermined surface locations are defined. This determination of the surface locations is based on the Azimuth Angular Beam Resolution (AABR). This angular resolution follows directly from the satellite velocity or the Doppler frequency, as is shown in chapter 3:

$$\theta = \arcsin\left(\frac{\lambda_c}{2|v_s| \cdot \tau_B}\right) \tag{4.1}$$

In which λ_c [m] denotes the wavelength, $\vec{v}_s$ [m/s] the satellite velocity and τ_B [s] the burst duration. Respectively, with values for λ_c of 0.0221 [m], a τ_B of 3.5 [ms] and a satellite velocity of 7.5 [km/s] a θ_{AABR} of 0.0239 [deg] follows.

Computing the surface locations for an orbit is achieved by making use of coarse and fine intersection loop as shown in figure 4.2. Within the coarse intersection loop the two burst surface positions are determined in between which the surface location is located. This is achieved by determining the angles from burst position to all the surface positions that correspond to the other burst locations. This angle is described by 4.4, which follows from the definition of the dot product (eq. 4.2) between two vectors and the definition of the magnitude of the cross-product of these same vectors (eq. 4.3):

$$\vec{n} \cdot \vec{w}_{sat \to b_i, surf} = |\vec{n}||\vec{w}_{sat \to b, surf}| \cos\theta \tag{4.2}$$

$$|\vec{n} \times \vec{w}_{sat \to b_i, surf}| = |\vec{n}||\vec{w}_{sat \to b_i, surf}| \sin\theta \tag{4.3}$$

$$\tan(\alpha_i) = \frac{|\vec{n} \times \vec{w}_{sat \to b_i, surf}|}{\vec{n} \cdot \vec{w}_{sat \to b_i, surf}} \tag{4.4}$$

In which α_i denotes the angle in between the vectors $\vec{n}$ and $\vec{w}_{sat \to b_i, surf}$, of which one is the vector from orbit location in direction of corresponding "nadir" surface location and the other the vector between "orbit" towards the "i'th" burst surface location. When the AABR falls in between two of these angles, the coarse loop is stopped and the fine loop is started.

These vectors can be derived by converting the geodetic burst coordinates into Earth-Centered Earth-Fixed (ECEF) coordinates, for which the MATLAB function *geodetic2ecef* is used.

Consequently, the fine loop interpolates in between these two surface positions until the surface location and burst position make an angle that is as close as possible to the AABR, hence to a certain level of convergence.

When the first surface location is determined the corresponding orbit state is determined by means of interpolation. The same procedure is repeated starting from this new orbit position.

These two loops are run for all burst positions, until all surface locations are found. For these surface locations the datation, baseline vectors and window delay are determined by means of interpolation, as well.

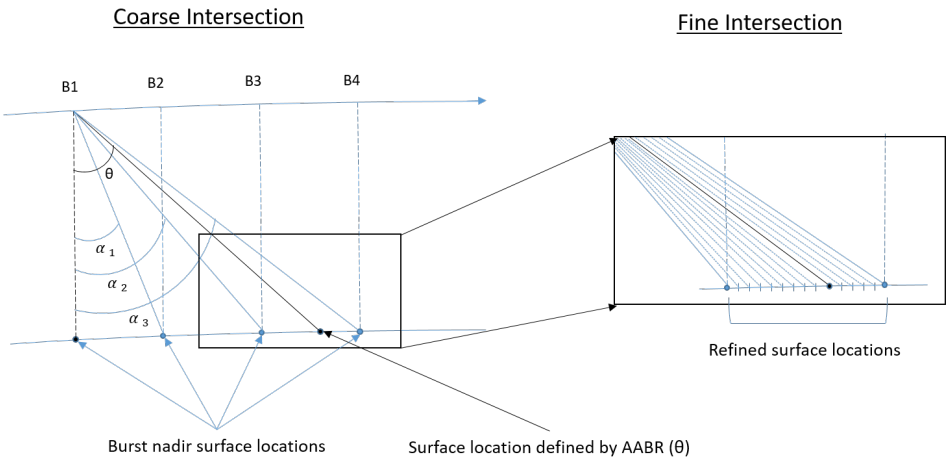

Figure 4.2: Graphical Display of Coarse and Fine intersection Loops (Cipollini, 2016)

One can choose to implement an external DEM to represent the surface at location or use the Window-Delay which is included in the dataproduct to determine the elevation at the surface locations.

4.1.3. Compute Beam Angles

After having defined the surface locations, the beam angles from all burst orbit locations to all surface locations are determined. As a direct consequence of the fact that a burst consisting of 64 pulses is transmitted, the 64 absolute smallest beam angles per burst location are stored. When beam forming is applied 64 Doppler beams are produced per burst location, with each their own surface location. Eventually this results in 32 aft-looking and 32 forward looking beams numbered with a beam identification number, as is displayed in figure 4.3. As shown in the figure the numbers lower than and equal to 32 will be aft-looking beams while the others are forward-looking.

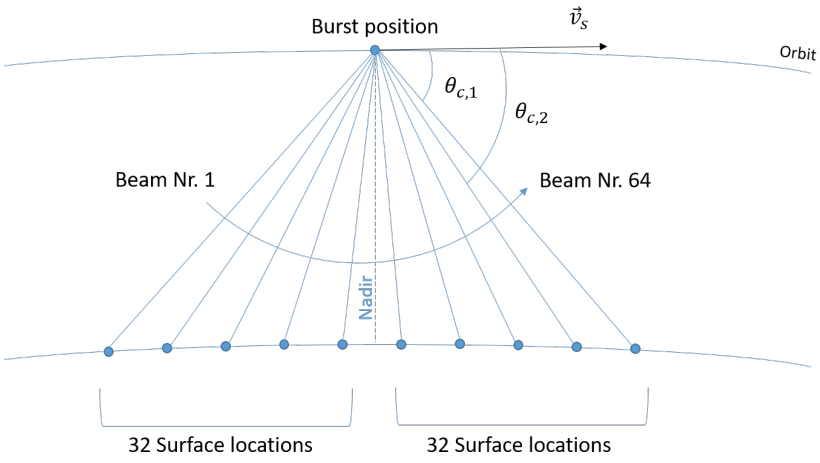

Figure 4.3: Graphical representation of beam angle determination (Cipollini, 2016)

The beam angles are computed in a similar manner as the angles that were determined for the surface locations. This is achieved by applying the definition of the dot product as shown in equation 4.5. The angle between the velocity vector $\vec{v}_s$ and the vector pointing from satellite to surface location $\vec{w}_{sat\rightarrow surf}$ can thus be calculated by applying equation 4.6.

$$\vec{v}_s \cdot \vec{w}_{sat\rightarrow surf} = |\vec{v}_s||\vec{w}_{sat\rightarrow surf}| \cos\theta_c \tag{4.5}$$

$$\theta_c = \arccos\left(\frac{\vec{v}_s \cdot \vec{w}_{sat\rightarrow surf}}{|\vec{v}_s| \cdot |\vec{w}_{sat\rightarrow surf}|}\right) \tag{4.6}$$

These beam angles are stored with their corresponding burst and surface location, as this information is required for the generation of the stacks after the beams are formed.

4.1.4. Azimuth Processing

Azimuth processing is the process in which from the burst 64 separate beams are formed in along-track direction. This is achieved by applying Beam Steering, Window application, and Beam Forming.

Beam steering Beam steering is applied before beam forming and is applied as a phase shift correction. The phase shift correction can be understood best by showing the geometry involved, as is presented in figure 4.4. At each pulse location a signal, which is not coming from nadir but from a random along-track location on the surface, is received with a relative phase delay. This phase delay over pulses can be considered a phase ramp. Steering of the beams can be achieved by altering this relative phase delay at each pulse location. For example, in figure 4.4 the dotted line represents the direction to which the original wavefront should be altered. This means an extra phase delay should be added to the 5 pulses, when rotating around pulse location $p1$. It should be noted that in figure 4.4 $p1$ is defined as the point to which the other phase delays are related. This point of rotation can be chosen at any location within the burst time, taken the relative phase delay between the different pulses is correct.

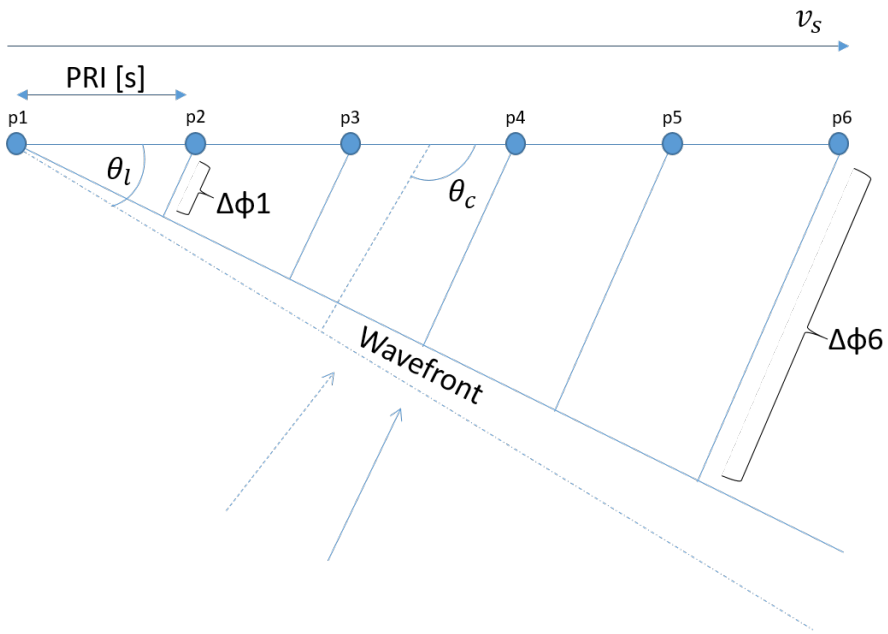

Figure 4.4: A schematic representation of the beam steering correction, based on the shown phase differences.

Whereas in (Wingham et al., 2006) look angle is used, the beam angle θ_c is applied in this case. The latter is applied in (Cipollini, 2016).

To give an example, the relative phase delay experienced at any pulse location pj relative to pulse location $p1$, as shown in figure 4.4 can be described as:

$$\Delta\phi_{bs,pi} = \sin(\theta_l) \cdot v_s \cdot (j-1)PRI - \Delta\phi_j = -\cos(\theta_c) \cdot v_s \cdot (j-1)PRI - \Delta\phi_j \tag{4.7}$$

As can be seen, this phase delay distance $\Delta\phi_{bs,pj}$ [m] becomes a phase cycle term when divided by the wavelength, and a phase term when multiplied by 2π. This is exactly the same as multiplying with the wavenumber k.

The correction is applied by multiplying the calibrated I/Q data samples in the time domain corresponding to the different pulse locations with a complex phase term based on the differential phase that is to be

applied. The beam steering can thus be considered as an added phase ramp. This complex phase term Φ_b as function of pulse index p s as shown by equation 4.8:

$$\Phi_b(p) = e^{\frac{-4\pi i|\vec{v}_s|\cos(\theta_c)PRI}{\lambda_c}p} \tag{4.8}$$

In which p varies over a range of $[\frac{-N_p}{2}, \frac{N_p}{2} - 1]$, in which N_p is the number of pulses (64) within a burst. PRI denotes the Pulse Repetition Interval [s], θ_c defines the beam angle as shown in figure 4.3.

The situation shown in figure 4.4 only considers the case in which the surface location is located, in aft-looking direction from satellite. However, the opposite case in which the surface location is located in front of the burst location is just a mirrored case of this one. In that case lag and lead are inverted.

After beam forming, the beams are angularly equispaced. However, the local topography whenever highly variable, can cause the surface locations to be not evenly spaced on the surface. This is why two different approaches are mostly applied for lower and higher variable topographies: an approximate and an exact method (Dinardo, 2013). The fact that for the exact method steers all the beams individually to the surface location, and hence per burst a FFT is performed for all surface locations. This is time consuming, and unnecessary whenever the topography is not highly variable. That is why in case of the approximate method only one beam angle, the angle corresponding to the beam closest to nadir, is applied to all beams. Thus, in this case only one FFT per burst is required.

The beam steering and beam forming is applied in loops per burst (approximate) or per pulse (exact). The method that is chosen depends on the standard deviation of the elevation in the burst.

Window application In order to reduce the effects of side lobes a weighting window can be applied prior to FFT application. According to (Dinardo, 2013) these effects mainly occur when an off-nadir beam is considered and strong nadir scattering is present. As for example close to the coast (Cipollini, 2016). A negative effect of applying a window is however a widening of the main lobe of the beam, and hence an increase in resolution. Resolution is defined here as the minimal distance between two objects at which they still can be distinguished. It was shown by Scagliola et al. (2013) a decrease in resolution could be achieved by choosing the weighting window wisely for waveforms produced over sea ice and open ocean. A Hamming window will be applied here (Cipollini, 2016) (Dinardo, 2013).

Beamforming The beam forming follows the beam steering and is in azimuth, hence along-track direction. The 64 phase weighted I/Q samples are converted into a frequency spectrum consisting of 64 frequency components. The frequency bins, or Doppler bins, are spaced at intervals of $\frac{PRF}{64}$. For SIRAL the PRF is equal to 18.182 [kHz], and thus the frequency spacing is equal to 284 [Hz]. The along-track sampling then follows to be equal to 313 [m].

The result of beam forming remains a matrix of size 64 x 512 per burst. However, at this point the 64 bins represent the different beams sorted over their along-track beam angle, pointing towards the surface locations.

4.1.5. Generate Stack

Following the azimuth processing, the stacks are generated. One beam per burst is selected and represents a look. All the looks corresponding to the same surface locations, but originating from different bursts are linked to each-other. This is achieved by running through all surface locations, which were saved in the step of computing the beam angle.

The beam indexation runs from 1 up till 64. Hence, the beam with the largest beam angle, the most aft-looking beam, is denoted beam 1. The beam with the smallest beam angle beam, which is forward-looking is given the index 64 (see figure 4.3)).

When desired, a selection can be applied here which removes beams with (along-track) beam angle higher or lower than a certain threshold value, as can be seen in figure 4.5. The threshold angle is denoted θ_{SSW}. This is called Sample Stack Weighting (SSW) as first introduced in the Cryosat Baseline C products (Scagliola and Fornari, 2015) and is applied to increase the SNR.

It should be known that in Baseline C the ESA L1b are stack weighted by a θ_{SSW} of 0.7 [deg]. This will be the value used as well for the verification and validation in chapters 5 and 6.

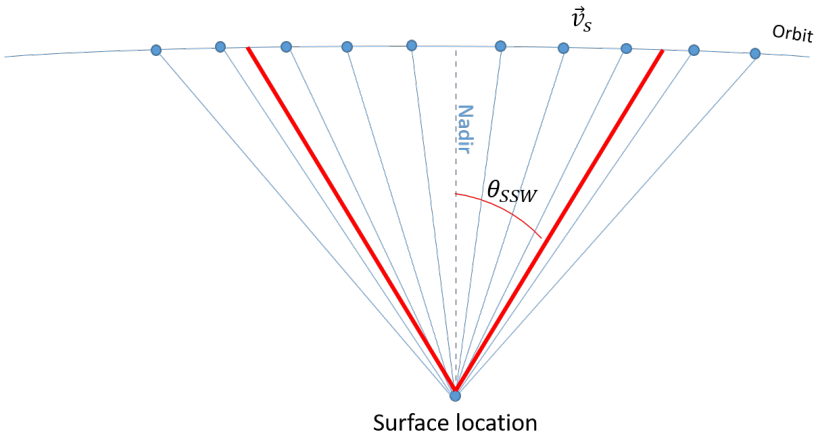

Figure 4.5: Graphical representation of surface stack sample weighting angle (Cipollini, 2016)

4.1.6. Geometry Corrections

The three geometry corrections are calculated for each beam within a stack. For each such a beam a specific correction is determined, which is a summation of the tree geometric corrections: the Doppler Correction, the Slant Range Correction (SRC) and the Window Delay Correction (WDC). This summation is shown in equation 4.9, where each correction is shown to be a function of the specific beam index within a stack b'. The unit of Δs is the amount of range bins that the samples need to be shifted.

$$\Delta s(b') = \Delta s_{Dopp}(b') + \Delta s_{WDC}(b') + \Delta s_{SRC}(b') \tag{4.9}$$

These corrections are thus applied as shifts in time, represented as an equivalent number of range bins. As was done for the beam steering, the correction is applied by multiplication of the original signal with a complex phase term Φ_{gc}. Multiplication with a complex phase term in the time domain is equal to a frequency shift in the frequency domain. This complex phase term is as shown in equation 4.10.

$$\Phi_{gc} = exp(i\frac{2\pi}{N_s} \cdot \Delta s(b')) \tag{4.10}$$

In which $N_{s,FBR}$ denotes the number of samples within a power waveform before zero-padding, which is equal to 512 [bins] in SARIn mode.

The range corrections are determined in their range bin equivalent by using the range resolution S_R as defined by (Chelton et al., 1989):

$$S_R = \frac{c\tau_{eff}}{2} = \frac{c}{2B} \tag{4.11}$$

In which τ_{eff}s is the effective two-way travel time resolution. S_R is thus the range [m] of one range bin (when the zero-padding has not been applied yet). By dividing the extra range delay in [m] as follows from the correction, by this range resolution, the same range delay can be expressed in the amount of range bins.

Doppler Correction Due to the velocity of the satellite during transmission and reception a Doppler Shift is induced. As a frequency shift in the initial received chirp translates directly into an frequency offset when the signal is deramped, a correction is required to counteract this effect. The correction is applied in the time domain.

The delay induced by the Doppler shift in [m] is described by equation 4.12 (Prats-iraola et al., 2014):

$$\Delta r_{DOPP}(b') = \frac{c}{2} \cdot \frac{\tau_{pulse}}{B}(-\frac{2}{\lambda}|\vec{v}_s \cos\theta_c(b')|) \tag{4.12}$$

The correction as expressed in the unit of range bins then becomes, when dividing equation 4.12 with the range resolution 4.11:

$$\Delta s_{DOPP}(b') = \frac{2\tau_{pulse}}{\lambda_c}\vec{v}_s \cos\theta_c(b') \tag{4.13}$$

In which τ_{pulse} denotes the pulse time.

Slant Range Correction The slant range correction (described as Delay Compensation by Raney (1998)) is applied to correct for the distance, that is travelled in between bursts. This correction in [m] can be described as follows:

$$\Delta r_{SRC}(b') = |\vec{r}(b')| - |\vec{h}(l)| \tag{4.14}$$

In which the $\vec{h}$ [m] is the nadir range from surface location l to satellite location, which is derived from the DEM. This correction can be described as function of range bins by division with the (compressed) range resolution (Chelton et al., 1989), as shown by equation 4.15.

$$\Delta s_{SRC}(b') = \Delta r(b') \frac{2B}{c} \tag{4.15}$$

Window delay misalignment correction The window delay defines the timing of the range window. The window delay is the two-way time between pulse emission and the reference point at the centre of this range window. For SARIn mode this point corresponds to the 255th bin number. Bins counting starts from 0 (ESA, 2012). This window delay is provided within the product, but varies over bursts. In order to be able to average over different waveforms these window delay differences thus need to be corrected for.

The Window Delay Correction (WDC) consist of shifting the measurements with an amount of sample bins, which makes sure the power waveforms are aligned accordingly. The equation giving the amount of samples to be shifted is given as (Cipollini, 2016):

$$\Delta t_{WDC}(b') = \tau_{WD,ref} - \tau_{WD}(b') \tag{4.16}$$

Which can be expressed in the amount of range bins by applying equation 4.17.

$$\Delta s_{WDC}(b') = \frac{\tau_{WD,ref} - \tau_{WD}(b')}{\tau_{eff}} \tag{4.17}$$

$\tau_{WD,ref}$ [s] denotes the reference window delay towards which the other window delays are shifted, and τ_{WD} [s] the window delay corresponding to the burst it originates from.

The reference window delay can be chosen differently. In the original SAR script as provided by Dr. Ir. Slobbe the reference window delay is interpolated to the nadir orbit location of the specific surface location. This interpolation has been applied in the computation of the surface locations, using a spline. It is shown in chapter 5 that this method does not show the best results over significant topography. In this case the best method of correcting for the window delay differences is picking the reference window delay as the delay corresponding to the highest power beam. This will be further explained in chapter 5.

The result up to this point still consists of complex data in the time domain and is denoted ψ_{gc}.

4.1.7. Range Compression and Multi-looking

Within this step, the multi-looked power, phase difference and coherence are derived. The latter two are derived from the multi-looked crossproduct as shown in equation 4.18.

For SARIn mode the Range compression and multi-looking step are combined for convenience. As described in Wingham et al. (2006) and Kleinherenbrink et al. (2014) the multi-looked power waveform $\Psi\overline{\Psi}^{(+,-)}_{ml}$, also known as the multi-looked cross-product, is determined as follows:

$$\Psi\overline{\Psi}^{(+,-)}_{ml} = \frac{1}{N_L} \sum_i \Psi^{(+)}_{masked}(i) \overline{\Psi}^{(-)}_{masked}(i) \tag{4.18}$$

In which N_L is the number of looks within the stack, defined by their specific look index i, the (+,-) denotes the two different receiver channels and $\Psi^{(+)}_{masked}$ and $\overline{\Psi}^{(-)}_{masked}$ denote the Fourier transform and the complex conjugate of the masked fourier transform of ψ_{gc}, where $\Psi^{(+/-)}_{masked}$ is calculated as follows:

$$\Psi^{(+/-)}_{masked} = (\mathscr{F}_{zp}(\psi^{(+/-)}_{gc})) \cdot H_{mask} \tag{4.19}$$

In which ψ_{gc} denotes the geometry corrected complex data samples in the time domain corresponding to one specific beam for one of the two channels (+/-). The resulting $\Psi^{(+/-)}_{masked}$ is the cross-channel waveform

corresponding to one beam, or one look. The $\mathscr{F}_{zp}$ denotes the FFT which is applied alongside the Zero-padding (ZP). Instead of 512 range samples the resulting waveforms will consist of 1024 samples, which is the size in which ESA provides their waveforms.

The masking is applied to filter out the samples that suffered wrapping due to the application of the phase shifts in the former step. This mask H_{mask} is produced by picking out the samples that go beyond the sample limits of "1" and "1024".

Power The multilooked power from the two channels is derived by taking the average of the powers of the two channels as shown by equation 4.20.

$$P_{ml} = \frac{1}{2}(\frac{1}{N_L}\sum_i \Psi^{(+)}_{masked}(i)\overline{\Psi}^{(+)}_{masked}(i) + \frac{1}{N_L}\sum_i \Psi^{(-)}_{masked}(i)\overline{\Psi}^{(-)}_{masked}(i)) \tag{4.20}$$

Different approaches were described in Wingham et al. (2006) and Kleinherenbrink et al. (2014), in which the multi-looked power was derived from the multi-looked cross-product. However, no exact description of this procedure was found. As a consequence the approach as described by 4.20 was preserved.

Phase difference The multi-looked phase difference is derived by taking the argument of the multi-looked cross-product $\Psi\overline{\Psi}^{(+,-)}_{ml}$ (Wingham et al., 2006) and correcting for the phase offset as found during CAL4 calibration, as shown by eq. 4.21.

$$\Delta_{ml} = Arg(\psi\overline{\psi}^{(+,-)_{ml}}) - \Delta_{CAL4} \tag{4.21}$$

It can be shown that the argument of the multilooked cross-product provides the phase difference by considering two example signals:

$$s_1 = a + bi, s_2 = c + di \tag{4.22}$$

From basic mathematics the phase difference between the two signals can be computed by:

$$\Delta_{s1-s2} = Arg(s1) - Arg(s2) = atan2(b,a) - atan2(d,c) \tag{4.23}$$

This is equal to taking the argument of the cross-product of the two signals as stated in equation 4.21 by making use of the following rule :

$$atan(x) \pm atan(y) = atan(\frac{x \pm y}{1 \mp xy}) \tag{4.24}$$

Which gives when considering signals with phases larger than $\pi/2$:

$$atan2(b,a) - atan2(d,c) = atan2(bc - ad, ac + bd) \tag{4.25}$$

The CAL4 phase difference which was calculated early on in this chapter is applied here as well. This phase difference cross calibration term Δ_{CAL4} is subtracted from the phase difference as given in equation 4.21.

Coherence The multi-looked coherence is calculated by applying the following formula:

$$K_{ml} = \sqrt{\frac{|\Psi\overline{\Psi}^{(+,-)}_{ml}|^2}{\Psi^{(+)}\overline{\Psi}^{(+)}_{ml}\Psi^{(-)}\overline{\Psi}^{(-)}_{ml}}} \tag{4.26}$$

In which the numerator denotes the multi-looked cross-product magnitude squared and the denominator the multiplication of both channel complex signals $\Psi^{(+)}\overline{\Psi}^{(+)}_{ml}$ and$\Psi^{(-)}\overline{\Psi}^{(-)}_{ml}$.

This definition is derived from the definition of the magnitude squared coherence and is shown to be most similar to the coherence which is provided in the Cryosat L1b products, which will be shown in chapter 5. Different formulas were given on the coherence in literature (Wingham et al., 2006) (Jensen, 1999), however implementing these formulas as presented did not produce the correct results. As equation 4.26 produced the most similar results to the coherence as found in the ESA L1b product it was adopted as the method to calculate coherence.

4.1.8. Finalization

As a final step, data that is included within the FBR product but has not been altered and are required in higher level processing need to be copied to the resulting L1b datafile. This includes interpolating all low frequency values as corrections to the new surface locations. Finally, the file is saved in a structure format for easy accessibility for the next processing step.

4.2. Implementation of L1b to L2-Swath processing

The exact implementation of Swath Processing will be elaborated here. The explanation will not be as extensive as the FBR to L1b processing steps discussed in the former sections, as this is not the main part of the thesis. However, in order to be able to interpret the L2 Swath processed results an understanding of the steps is required.

The steps that the processor consist of are as shown in figure 4.6. These steps were used as written in MATLAB by Slobbe et al. (2016). It should be noted here that the first 4 steps, from Phase Smoothing up to Global Phase Unwrapping are as described by Gourmelen et al. (2017), where the Optimization and the Filtering are not. These latter two steps were written by Slobbe et al. (2016), alongside several routines used within the geolocation.

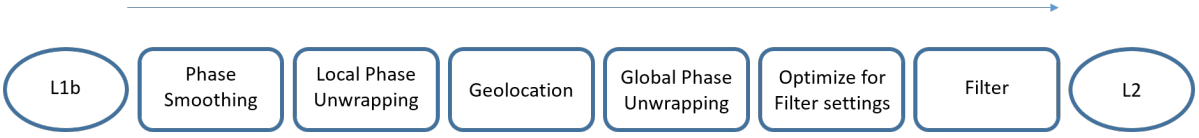

Figure 4.6: The Swath processing steps, from the L1b waveforms to the L2-Swath elevations.

Before the swath processing is applied data editing is applied on the raw waveforms. This data editing consists of filtering data out which are flagged erroneous within the data product. Furthermore, waveforms are filtered out when the first 80 power samples are higher than 10 % of the max power. Similarly, the waveform energy is calculated by integration over samples. If waveform energy is higher than a certain level the waveform is filtered out. For a start this level is set at 150 [-], normalized energy, as this was applied in the previous SAR mode version.

4.2.1. Phase Smoothing

Noise is present in the phase difference measurements. These errors propagate into the across-track geolocation and thus need to be removed. As such, the phase difference needs to be filtered. A difficulty encountered when filtering the phase differences is the sudden phase wraps equal to 2π. In order to overcome this, the complex exponential of the phase is determined and the real part and complex part are filtered separately, as these do not suffer from wrapping (Nilsson et al., 2016).

The interferogram I is produced by applying the following formula:

$$I = e^{i\Delta_{ml}} \tag{4.27}$$

In which Δ_{ml} denotes the interferometric phase [rad].

A moving average filter is applied to the real and imaginary components of the phase difference. Dependent on the size of the moving average filter the slant range resolution is decreased (Gray et al., 2013) and hence, the across-track surface resolution. However, the across-track footprint dimension still is much smaller compared to non-interferometric POCA results.

4.2.2. Local Phase unwrapping

After having smoothed the phase difference, the phases are unwrapped. As mentioned before, jumps of size 2π are present in the measurements and need to be corrected for.

This is done by adding positive or negative 2π to the phase difference at locations where such a phase jump is found. The MATLAB function "unwrap" is applied to achieve this. The procedure is started from the centre sample (512 for SARIn) in both directions. The centre sample is picked as starting point as this is expected to have a high coherence value (Nilsson et al., 2016), and high coherence means a high quality measurement. This is done as the first and final samples of the waveforms are very noisy and mostly do not provide valid phase difference measurements.

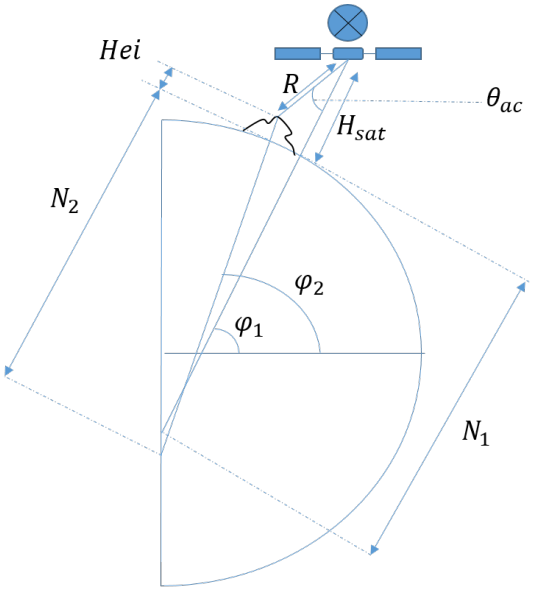

Figure 4.7: A graphical representation showing the method in which the height is determined

4.2.3. Geolocation

The height and coordinates are calculated for all valid waveform points. No filtering has yet been applied. The height and coordinates are derived from the range and across-track angle.

Range and Across-track angle The range is calculated as described in (ESA, 2012) and follows from the window delay τ_{WD}, the retracking correction τ_{ret}, and the geophysical corrections $\epsilon_{Geophysical}$.

$$R = \frac{c\tau_{WD}}{2} + \frac{c\tau_{ret}}{2} + \epsilon_{Geophysical} \tag{4.28}$$

The retracking correction is determined from the sample bin number that is picked times the sampling interval τ_{eff} (3.125 [ns]) minus the 512 in case of SARIn processing. Different geophysical corrections need to be applied dependent on the surface types that are overflown (ESA, 2012).

As with conventional SARIn POCA measurements the phase difference can be used to determine the angle of arrival. The formula states:

$$sin(\theta_{ac} + \beta) = -\Delta_{ml}/kB \tag{4.29}$$

Where β the roll angle of the baseline, θ_{ac} the look angle, k the wavenumber and Δ_{ml} the differential phase. The differential phase is corrected as well for errors in the Star Tracker measurements. These mispointing errors are provided by ESA (Gourmelen et al., 2017).

Elevation and coordinates In combination with the computed range for the selected across-track look angles the across-track locations and the corresponding Elevation can be determined. The coordinates are determined by applying the function *Reckon* in MATLAB. This function computes the Latitude and longitude when given an initial position on a sphere, an "arclength" and the azimuth direction.

For both computations the ellipsoid coordinate system is used. The associated height H_{surf} [m] to ellipsoid are determined by applying formula 4.30, which can be derived by applying the Cosine Rule to the geometric situation as shown in figure 4.7:

$$H_{surf} = \sqrt{R^2 + (H_{sat} + N1)^2 - (2Rcos(\theta_{ac})(H_{sat} + N1))} - N2 \tag{4.30}$$

In which H_{sat} denotes the orbit altitude of the satellite with respect to the WGS-84 ellipsoid, N [m] denotes the equatorial radius and is described by the following formula:

$$N = \frac{a}{\sqrt{1 - e^2 \sin^2 \phi_{geod}}} \tag{4.31}$$

In which a and e are the semi-major axis and eccentricity of the Earth's ellipsoidal approximation and ϕ_{geod} the geodetic latitude of the satellite.

An assumption that is applied here is that the ellipsoid at the location of the satellite can be approximated by a sphere, as the across-track angle is so small. As a consequence N2 an N1 can be considered equal to N. At the same time, as the satellite flies in a nearly polar orbit (92.3°), and the look angle can be considered small (~ 1 [Deg]) the latitudes of the side-looking measurements in across-track direction will not vary much. The altitude is considered constant in across-track direction and hence $Rcos(\theta_{ac})$ can be considered to be perpendicular to the surface.

This simplifies formula 4.30 into:

$$H_{surf} = \sqrt{R^2 + (H_{sat} + N)^2 - (2Rcos(\theta_{ac})(H_{sat} + N))} - N \tag{4.32}$$

4.2.4. Global Phase Unwrapping

Finally, a global phase unwrapping is required in order to correct for left over phase wraps (Gourmelen et al., 2017). For a range of phase differences with added jumps of 2π and -2π the heights and locations are calculated. The height value that matches the DEM at the location the best is chosen as final measurement. The steps are added over a range of -10 up till 10 times 2π

4.2.5. Quality Filtering

The quality filtering can be performed using different criteria.

The most common criteria for filtering are power, coherence and across-track look angle. Methods which make use of different criteria as across-track look-angle do exist but will not be tested in this thesis, as it is outside of the scope of the research.

In order to choose the optimal threshold levels a trade-off is required. The amount and the quality of the data depends on the thresholds chosen. The quality of elevation data is mostly the standard deviation of the elevation difference with the DEM. This is desired to be as low as possible. At the same time, an advantage provided by Swath processing is the increase in data points.

In order to cope with this trade-off a criterium needs to be set. A criterium that was proposed by personal communication with Cornelis Slobbe to optimize the thresholds is $\frac{\sigma_{DEM}}{log(N_{Meas})}$. The σ_{DEM} denotes the standard deviation of elevation difference with the DEM and N_{meas} denotes the number of data points produced. By choosing the settings that produce the minimum ratio the optimal thresholds are chosen. For now, this criterium will be used in further analyses.

The algorithm loops over filter values for coherence, across-track look angle and power. The range and step size for these loops are found in table 4.1.

Optimization Criterion	Start	end	Step Size
Power	0	0.9	0.05
Coherence	0	0.9	0.05
Across-track Look angle	0	2.4	0.2

Table 4.1: Filter settings over which optimization loop is run

4.3. Verification and Validation strategy

The SARIn processor will be verified by comparing interim results to the results ESA provides. This verification will give a rough insight into the correctness of the calculated L1b variables. It is expected that minor differences will still be present. Due to these differences, it is not possible to apply the same filter settings for the Swath Processing algorithm. As a consequence, the optimization needs to be run separately for both datasets.

4.3.1. L2-Swath comparison to GIMP DEM

As a first quality assessment, the validation of the eventual L2-Swath heights will be performed by making a comparison with the GIMP digital elevation model (Howat et al., 2014). Comparing the L2-Swath elevation to the DEM is relatively straightforward, as the DEM can be interpolated to the measurement locations.

The desired result is a low standard deviation of the differences, as this indicates a small spread, and thus high precision. It should be noted here that a distribution with a mean close to zero is not a good quality indicator, and it does not indicate a high precision. As explained in chapter 3, the DEM is composed of different older datasets. Hence, a difference between the two datasets is expected. At the same time, seasonal changes can cause differences to exist as well.

4.3.2. L2-Swath comparison to IceBridge

The precision of the datasets can be better assessed by comparing the datasets with the Ice Bridge Laser Altimetry data. Within this comparison the standard deviation and the mean of the differences both are indicators for the quality.

The Laser altimetry data will be compared to the radar altimeter data by picking out the radar points that are within a 50 [m] distance from the IB laser points. A limit can be set on the difference in time between the two measurement points. Nevertheless, this is expected to have little impact as the months March, May and April are not known for its rapid changes over time (Gourmelen et al., 2017).

The differences between laser and radar altimetry need to be taken into account when observing the results. As was discussed in chapter 3 the surface interaction of laser and radar waves differ. It is expected that the on average a lower mean will be found for the radar measurements due to their deeper penetration compared to Laser altimetry.

The measurements as presented by Gourmelen et al. (2017) and shown in table 4.2 over the Petermann already showed a negative valued mean for his L2-swath to IceBridge elevation differences. These results were serve as reference at the end of the validation. It should be noted though, that the extent of the area of interest used by Gourmelen is not known. This means the exact amount of data points found cannot be clearly compared. Similarly, the exact period over which this comparison was made is unknown. It is expected due to comparisons in amount of POCA data points in a period covering March till May, in one specific year in the range of 2011 up to 2014. This is in contrast to the period covering March till May 2017 over which the current analysis has been taken place.

Swath Elevation to IB difference [m]	POCA Elevation [m]	Swath/POCA number of measures (10^3)	Period
-1.3 ± 1.2	-1.1 ± 0.8	44.9/1.4	Expected: March-May (2011/2012/2013/2014)

Table 4.2: Results as found by Gourmelen over the Petermann Glacier (Gourmelen et al., 2017)

5

Verification

The implemented processor will be verified by comparing the results to the L1b products as processed by ESA. Furthermore, a period covering March, April and May 2017 of data, will be processed over the the Petermann Glacier, for both ESA L1b and ESA FBR. The results will be compared with a DEM and Laser Altimetry measurements as provided by the Operation Icebridge campaign.

5.1. Full Bit Rate (FBR)

The Cryosat-2 orbits which were found overpassing Cryosat-2 in the period of time of our interest are shown in figure 5.1. It follows from the inclination of the orbit (92°) that the orbits which are tilted to the right (for example the orbit corresponding to 26-04-2017) are the descending orbits and the orbits tilted to the left are the ascending orbits. The locations of the markers show the locations at which FBR data bursts are found. Each point corresponds to approximately 3 bursts. The map reveals data gaps to exist in several descending orbits.

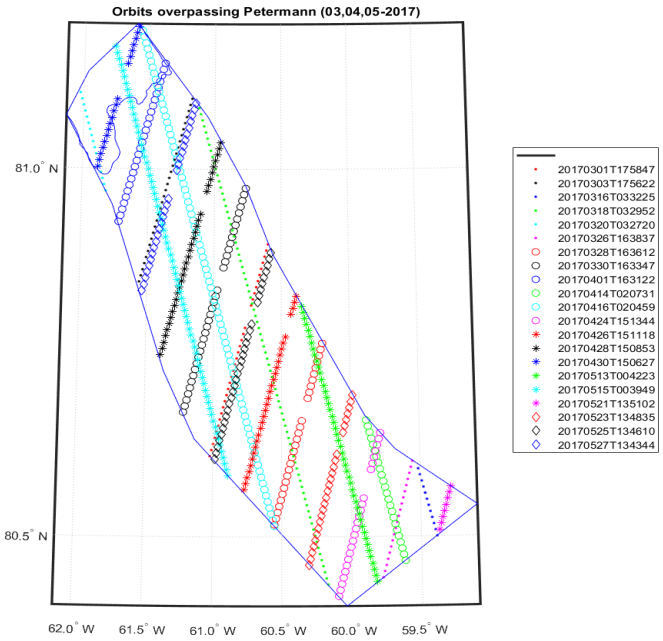

Figure 5.1: The orbits that overpass the Petermann Glacier over the period of March till May 2017

5.2. Level 1b

Within this section the FBR to L1b processor will be verified. Furthermore, it will be checked whether the CAL4 calibration as described in section 4.1.1 is applied correctly.

5.2.1. Waveforms

The echograms for one entire orbit which passes over the Petermann Glacier are shown for the ESA L1b product (right) as well as for the FBR derived product (left) in figure 5.2. As a first impression, one can conclude that the echograms show little similarity.

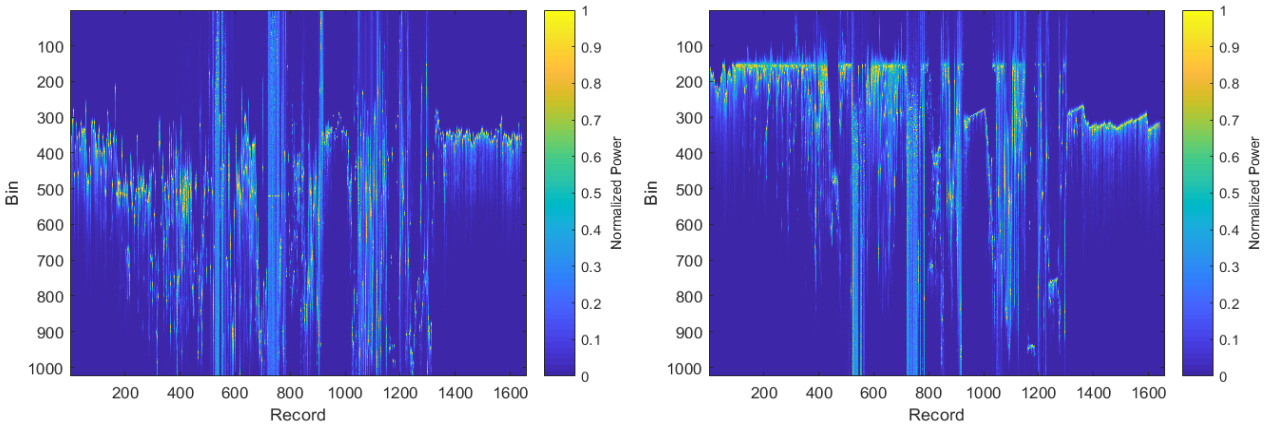

Figure 5.2: Echogram corresponding to one entire SARIn orbit (01/03/2017) overpassing Petermann Glacier, as derived from the FBR product (left) and as provided within the ESA L1b product (right)

If a look is taken at a single power waveform within the same echogram, as shown on the left of figure 5.3, it can be seen that the waveforms produced are of similar shape, however shifted in range time. Such a shift can be found to be present for all waveforms in the echogram. It is expected that ESA (Dinardo, 2013) applies a sample shift to all the waveforms to align the peaks of the power waveforms closer to the front of the range window. This difference does however not cause any difference in the resulting elevation measurement as the window delay is accordingly corrected for.

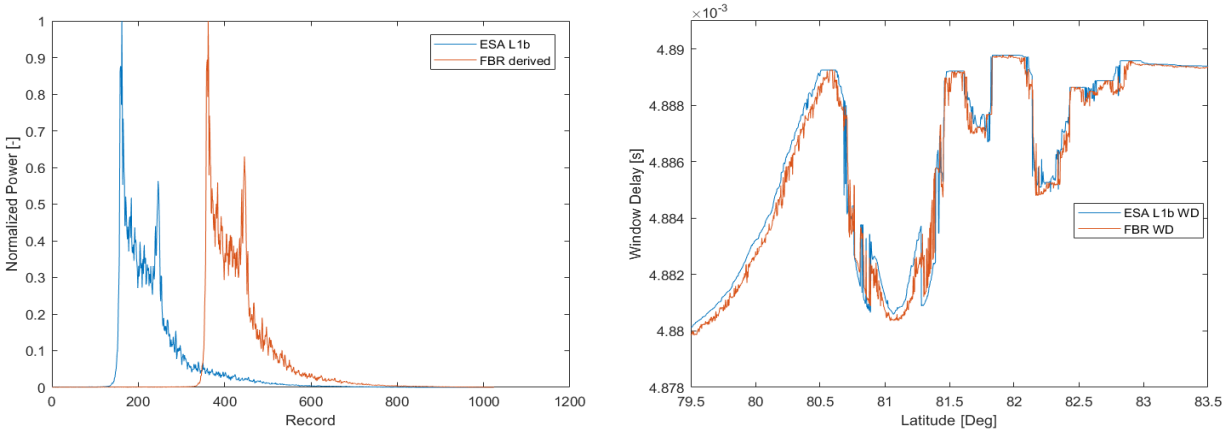

Figure 5.3: Single record of the (normalized) power waveform derived from the FBR (Red) and as provided in the ESA L1b product (Blue) on the left. Window delay for entire SARIn pass as function of latitude, for the FBR derived and ESA L1b case.

This shift is visible as well in the window delay, as can be seen in 5.3 on the right. It was found, by correlating all power waveforms as shown in figure 5.2, that the shift expressed in number of bins, is generally equal to the difference in Window Delay. This is shown in figure 5.4, where the difference between the two is shown

to be equal to zero for a large part of the SARIn orbit. The records at which the difference is not equal to zero, correspond to cases in which the correlation is not properly achieved due to high noise levels.

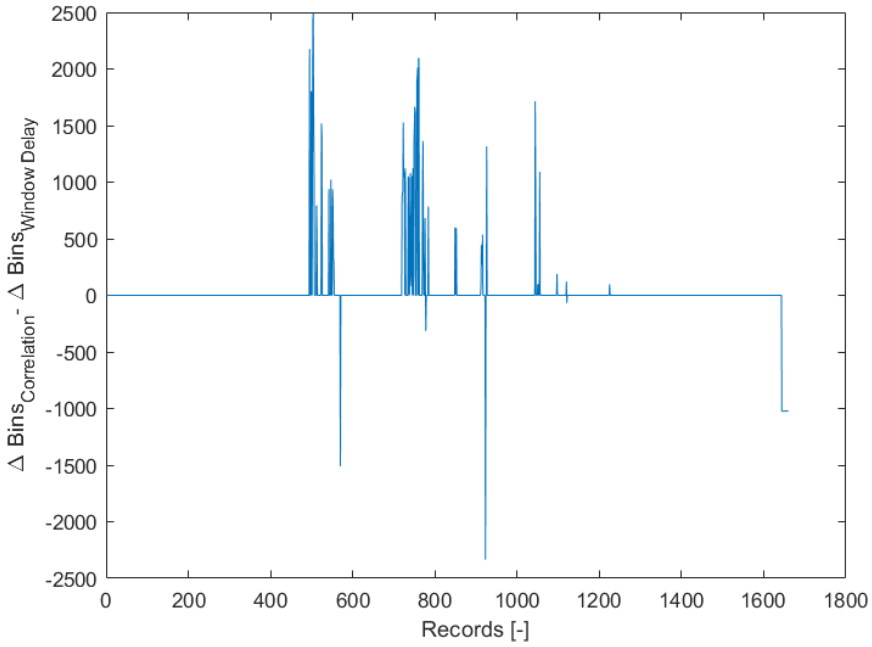

Figure 5.4: Difference between the number of bins that the power waveforms from the ESA L1b product and the FBR derived product are shifted with respect to eachother, which are acquired by means of correlation $\Delta Bins_{Correlation}$, and the number of bins equivalent window delay difference $\Delta Bins_{WindowDelay}$.

By shifting the FBR produced waveforms an equal amount of bins to the amount of bin difference found when differencing the window delay, the product as shown on the left of figure 5.5 is produced.

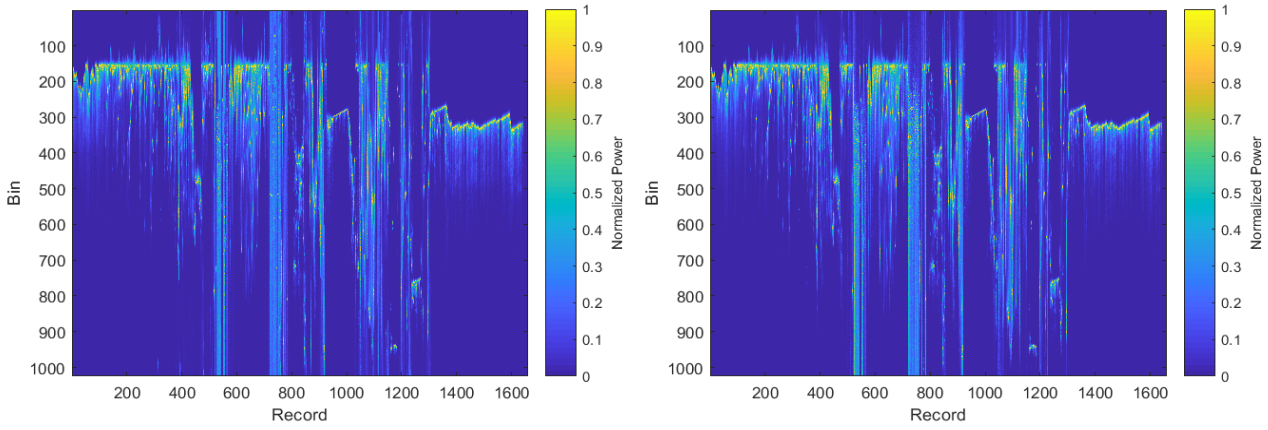

Figure 5.5: Echogram corresponding to one entire SARIn orbit overpassing Petermann Glacier, as derived from the FBR product (left) and as provided within the ESA L1b product (right), but now shifted with the difference in window delay

The same analysis is shown for the other main Level 1b variables Coherence and Phase Difference in the appendix A. The same conclusions can be drawn for these variables.

Example of single L1b result As it is to cumbersome to compare all waveform samples that are generated, the L1b products for one single surface location are shown here. The Swath Processing algorithm will eventually show how well the data compares on a bigger scale.

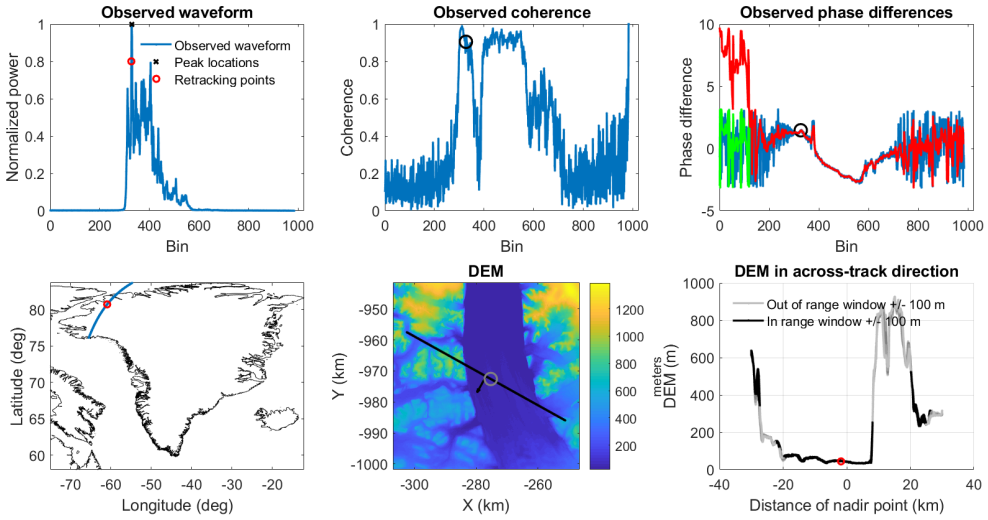

Figure 5.6: Waveform characteristics following from ESA L1b product. In the top line the power waveform, and corresponding coherence and phase difference (blue: wrapped, unfiltered; green: wrapped,filtered; red:unwrapped, filtered) are shown. The bottom figures give the location of the measurement overall, zoomed in at the glacier, and relative to the DEM.

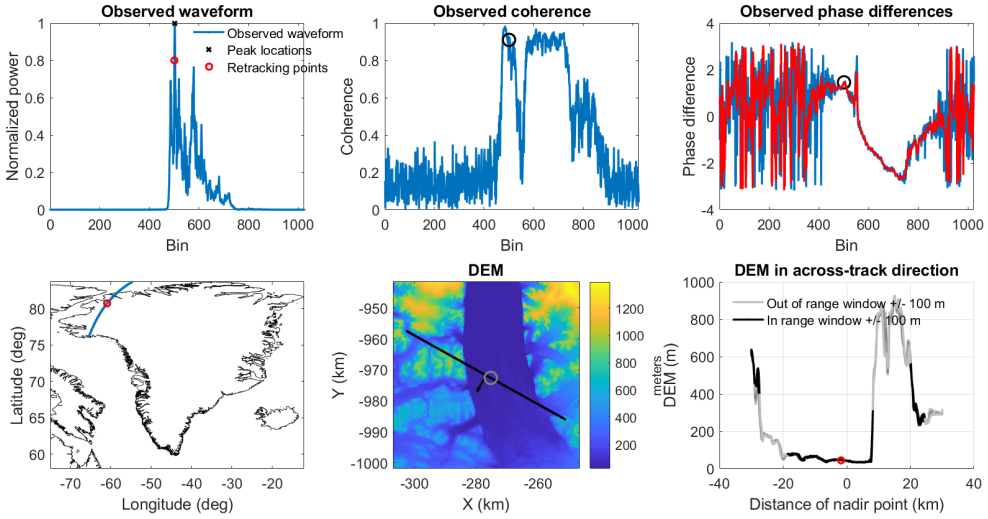

Figure 5.7: Waveform characteristics following from the FBR to L1b processing. In the top line the power waveform, and corresponding coherence and phase difference (blue: wrapped, unfiltered; green: wrapped,filtered; red:unwrapped, filtered) are shown. The bottom figures give the location of the measurement overall, zoomed in at the glacier, and relative to the DEM.

It can be seen from figure 5.6 and 5.7 that all the waveform characteristics for this one waveform look alike, but differ at a few locations.

Furthermore, the power waveform shows two large peaks in both cases, however different behaviour is present in between these two peaks. It should be noted that the circle represents the threshold (0.8) retracked sample and height. The coherence follows approximately the same shape in both cases, however the coherence is slightly lower overall, and does not reach as close to the value '1'.

5.2.2. Window Delay

Within the FBR to L1b processing, little processing is actually performed on the window delay. The only processing involved in the SCOOP (Cipollini, 2016) processing scheme is the interpolation of the Window Delay to the computed surface locations. The window delay, as derived from the FBR data product, does show differences from the window delay as provided in the ESA L1b, related to the locations within the descending orbits in which data is missing, as shown in figure 5.1.

Window Delay Differences The window delays for such a particular Petermann fly-over are shown in figure 5.8. Four different cases are shown: the window delay as provided in the FBR data product, the window delay as provided in the ESA L1b product, the window delay as derived from the FBR product with the SCOOP processing as described in 4, and the window delay corresponding to a case in which the window delay correction is applied with respect to the Maximum Power Stack sample (MPS), which will be explained in the following.

It can be seen that the FBR derived L1b window delay is the interpolated version of the FBR WD. The ESA L1b Window Delay shows a different pattern. Apart from the fact that at the lower latitudes the ESA L1b window delay is relatively constant in contrast to the FBR and the FBR derived Window Delay, the Window Delay is higher closer to the border of the Petermann Glacier. This difference can be related to the correction of the window delay, as part of the Geometric Corrections.

Window Delay Correction When a look is taken at the values of the Window Delay Correction (WDC) in this region, as shown in figure 5.9, it can be seen that large corrections are applied, up to positive or negative 2000 [bins]. These amounts of shifts cause the waveforms to be completely removed from the stack, as the range window only contains 1024 sample bins.

When a look is taken at a corresponding stack with and without the WDC applied (see figure A.3), this effect is shown. The high power returns are filtered out. In contrast the low power noisy signals are kept and only shifted a little. The WDC apparently, applies a shift to the high power waveforms, which is so big that the stack samples are lost. This is caused by the large jump in window delay present over this specific area, as can be seen in figure 5.8.

Geometry Involved The beams that are shown in figure A.3 originate from different bursts with different window delays. Normally, the Window Delay does not vary too much over a stack. However, due to the large cliff present at the area of interest, a large window delay jump is present within the stack. Currently, the Window Delay Correction is applied based on the interpolated window delay at location. However, the high topographic jump is not captured by this interpolation. Hence, an incorrect Window Delay is applied.

The situation can be explained by showing a geometric representation of the situation (see figure 5.10). Normally, the window delay is correctly defined due to the closed loop tracking control, as shown in the nominal case top left of figure 5.10. In this case data is missing after passing the large cliff (top right of figure 5.10).

It is expected that this data gap is actually caused by the fact that the closed loop tracking control loses track of the surface, and puts in extra effort to find it back by varying its range window timing randomly. During this period no data can be received, hence causing a data gap. Nevertheless, a measurement can be still recovered on the locations of the data gap due to the beams at larger look angles.

The window delay correction, as explained in chapter 4, is referenced with respect to one specific window delay in the stack. However, no Window Delay is available at these locations (see top right of fig. 5.10). In the SCOOP processing the reference Window Delay of this location is thus assumed to be equal to the interpolated Window Delay at this location (see bottom left 5.10). This interpolation is achieved by applying a cubic spline. However, the Range Window corresponding to this Window Delay does not correspond at all to the ranges as expected from the surface location (as shown on the bottom right). As a consequence, a WDC is applied which is much too large, and the signal is lost.

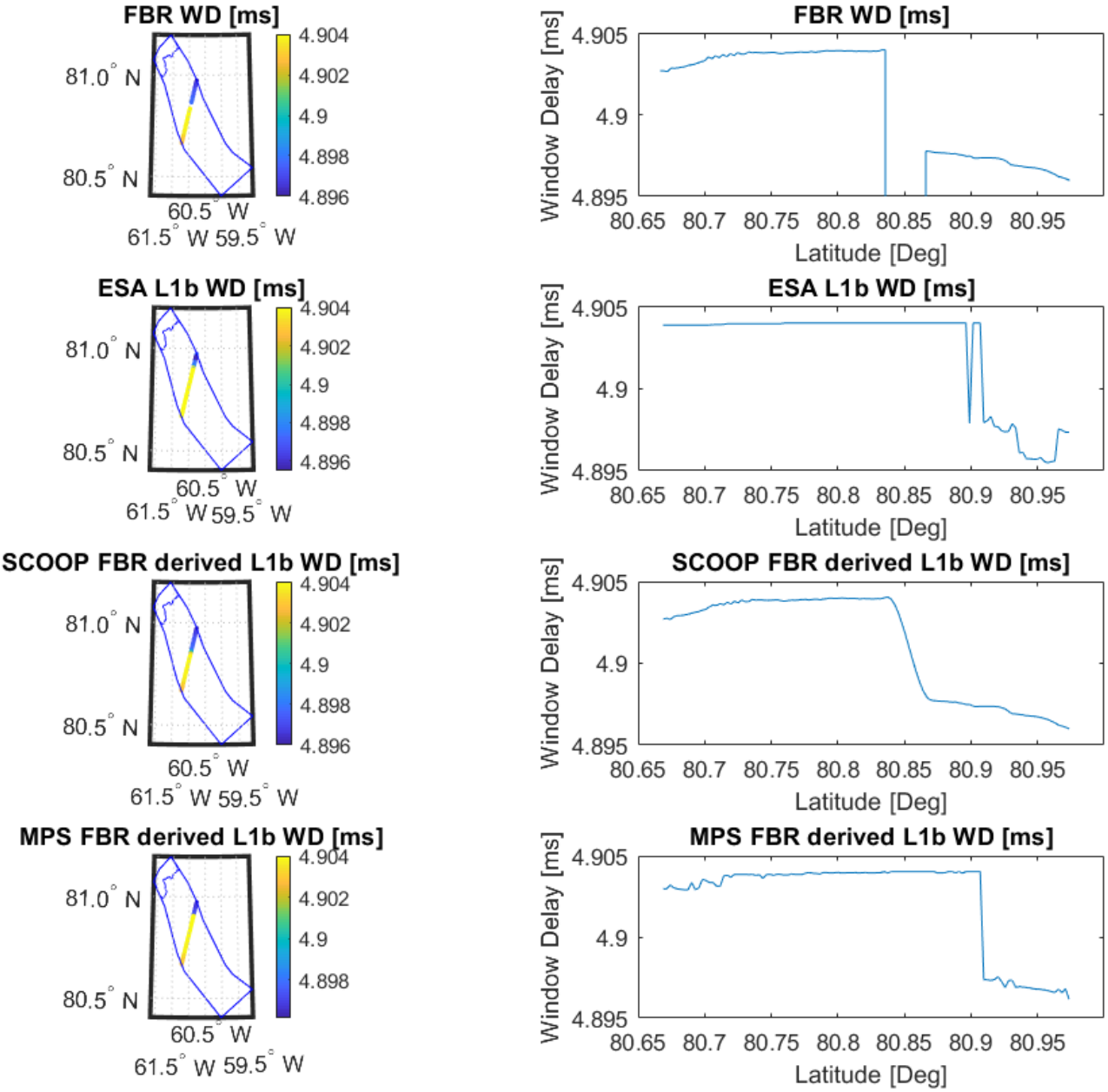

Figure 5.8: The window delay when it passes over the Petermann Glacier. At the left the orbit is shown over the Petermann Glacier and at the right the window delay in [ms] as function of latitude. From top to bottom: Window Delay as included in the FBR product; Window Delay as included in the ESA L1b product; Window Delay as follows from SCOOP processing (interpolated version of FBR WD); Window Delay that follows from picking the Maximum Power waveform within the stack (Max Power Sample (MPS)

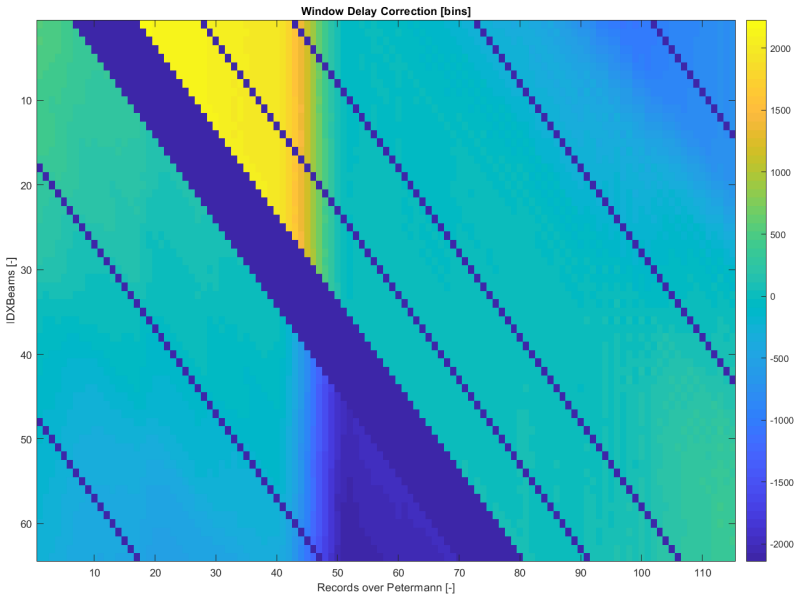

Figure 5.9: The Window Delay Correction presented as number of bins for the piece of orbit which trespasses the Petermann Glacier. The Beam indexation counts from 1 to 64, from aft-looking beams to forward looking beams.

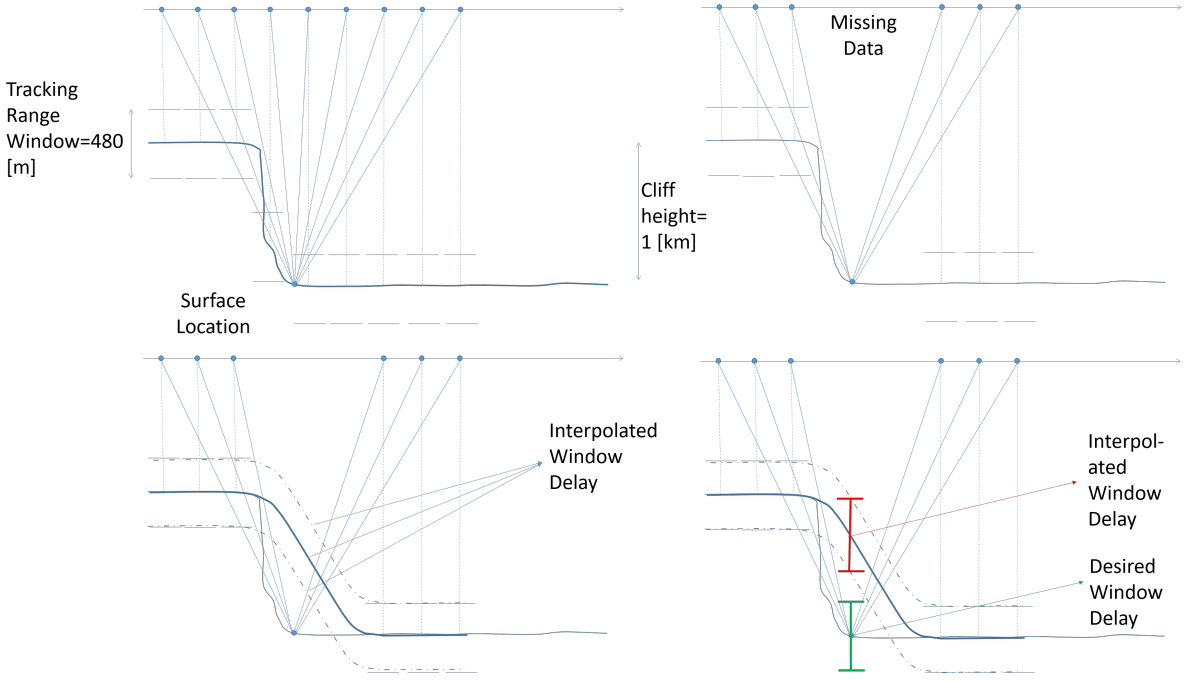

Figure 5.10: The scenario involved as encountered over the Petermann Glacier.

In essence, the expected timing of the return signal is incorrectly defined. As such, no signal is received.

Maximum Power Stack Sample As a consequence, this data is lost and no measurements are found at all for one surface location. However, a measurement can be recovered at the corresponding surface location, when a correct window delay reference is used within the window delay correction, as seems to be applied by ESA.

The reference window is chosen, to be the window delay corresponding to the stack power waveform with the maximum power. This is based on the assumption that the most valuable measurements within a stack are of the highest power. This assumption makes sense as stack samples which are received within an incorrect range window consist of noise.

The effect of picking the max power stack sample (MPS) for the window delay correction is shown in figure 5.11. At the location of the cliff (sharp increase of green line), both derived Window Delays show a delay with which the nadir range to surface is centered within the range window. The Max Power Sample (MPS) window delay (Blue lines) however changes abruptly, at the first moment it receives a signal from the lower elevated glacier. From this point onwards the range to surface at nadir is centered again in the range window. In the case of the interpolated Range Window this occurs a little while later in time.

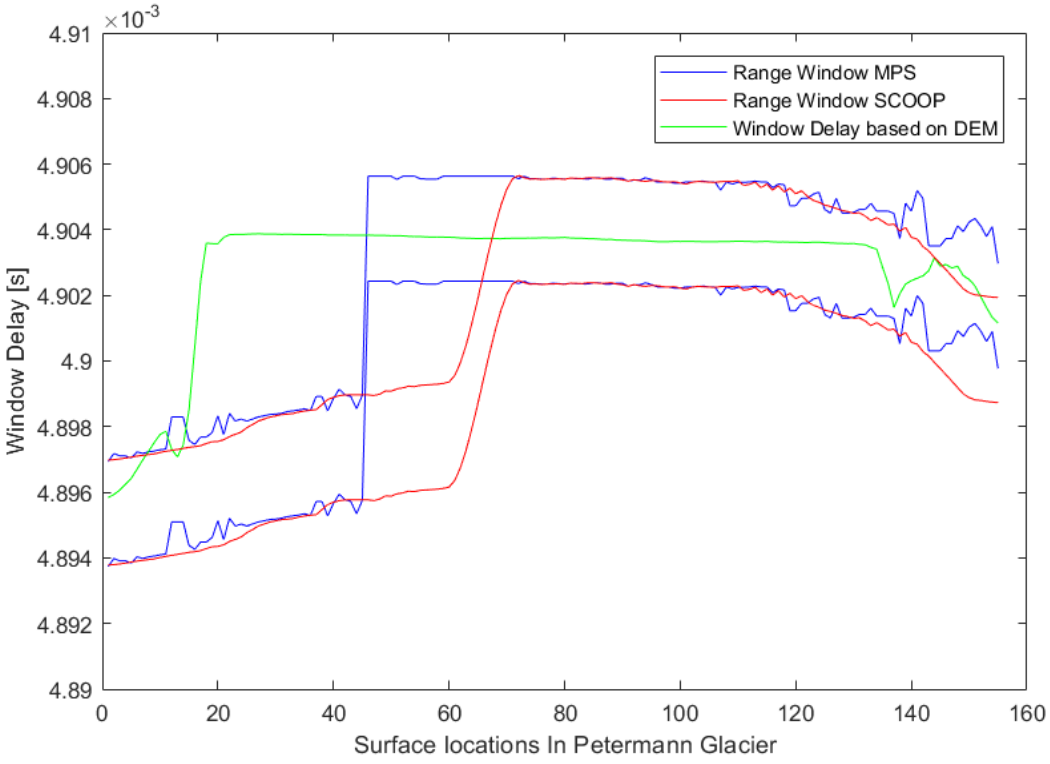

Figure 5.11: The range window boundaries shown for the MPS (blue) case and the SCOOP (red) (interpolated)case. The two way timing from satellite to DEM elevation at the surface location is shown as well (green). The sharp increase in Window Delay based on DEM is due to the cliff present at the side of the Petermann Glacier.

The consequence of using the window delay is shown in figure 5.12. In the figure, the extended power stack is shown on the top left, accompanied by the corresponding averaged power over the stack, as well as the locations of the burst which contribute to the stack. The dotted red area shows the range window based on the interpolated version of the window delay, whereas the dotted green box shows the range window as based on the MPS window delay. As can be seen little useful power is received in the red area, compared to the green.

This small alteration of the window delay correction showed to result in a Window Delay that shows large similarities to the Window Delay as provided in the ESA L1b product. As a result an increase in unfiltered L2-swath data points for the orbits of interest as is shown in figure 5.14.

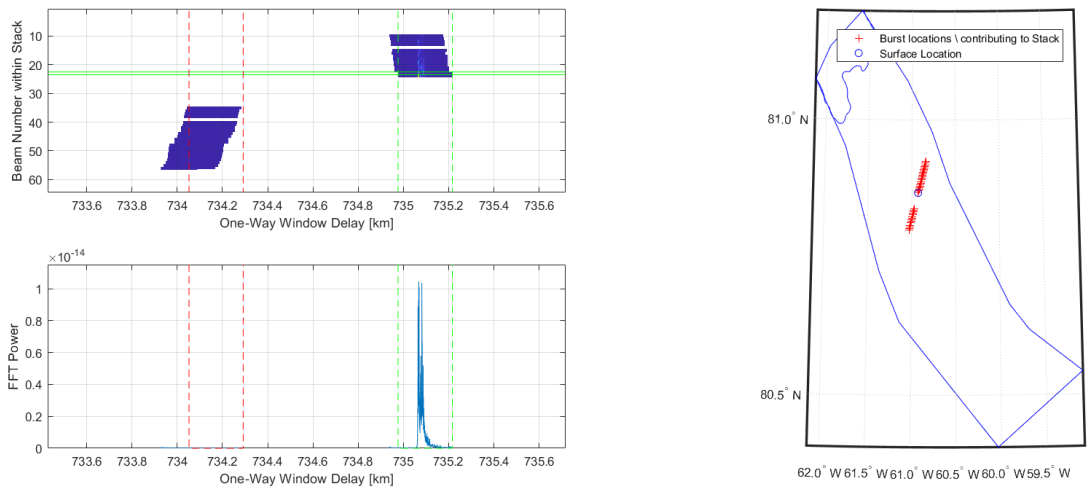

Figure 5.12: An extended stack collected over the Petermann Glacier, showing the effect of the large cliff. On the left, the extended stack is shown corresponding to a surface location located in the Petermann Glacier, as shown on the right. The dotted red and green boxes denote the range windows as derived from the SCOOP window delay and the MPS window delay. The solid green box shows the beam within the stack with the Maximum Power. On the bottom left the power waveform is shown, that results from averaging the power waveforms over the stack in the range window.

5.2.3. CAL4 Calibration

As no documentation was found regarding the exact manner of the CAL4 calibration, the results following from applying this calibration will be verified in this section. This is most easily achieved by comparing the geolocations which are derived from the phase-differences for the ESA L1b case and the FBR derived L1b case.

For one ascending Cryosat-2 overpass of Greenland a part of the orbit is shown in figure 5.13. The location with respect to northern Greenland is shown on the left. The particular part of the orbit is located on open ocean. This location was chosen as the measurements should be located at nadir of the orbit. It should be noted here that in between two subsequent measurements a distance of around 300 [m] is present.

The individual measurements are derived by means of a threshold retracker set at 0.8, with the maximum amount of peaks retracked per waveform set to 1. This means that the retracked sample is picked at 80 % of the biggest peak that is present in the waveform. This retracker is applied to both the ESA L1b waveforms as well as the FBR derived waveforms.

It can be seen that the CAL4 phase difference calibration when not applied, causes a large deviation. When applied however, the FBR derived geolocations show to be largely similar to the ESA L1b derived geolocations.

5.3. Level 2

In this section, the level 2 results which are derived from the L1b products will be verified. As a first indicator of relative quality, a threshold retracker is applied to both the ESA L1b products and the FBR derived L1b products as collected over the Petermann Glacier area.

Consequently, the Interferometric Swath Processing will be applied to both products. Two products within the Swath Processing process will be considered here: the Swath processed product before filtering based on the Swath filter parameters as coherence, power and across-track angle, an after this filtering.

5.3.1. Threshold retracked L2

The threshold retracker (Davis, 1995) picks out an amount of peaks within the power waveform. The amount can be set beforehand as a Maximum Number of Peaks (MNP). per waveform. Dependent on the threshold chosen, a point on the leading edge of this power peak is picked out for the further range measurements. The threshold is defined as a percentage above the basic noise level. The basic noise level is defined as the average power of the first 12 bins of the waveform.

By applying a threshold retracker, with different input settings for both the ESA L1b product as well as the

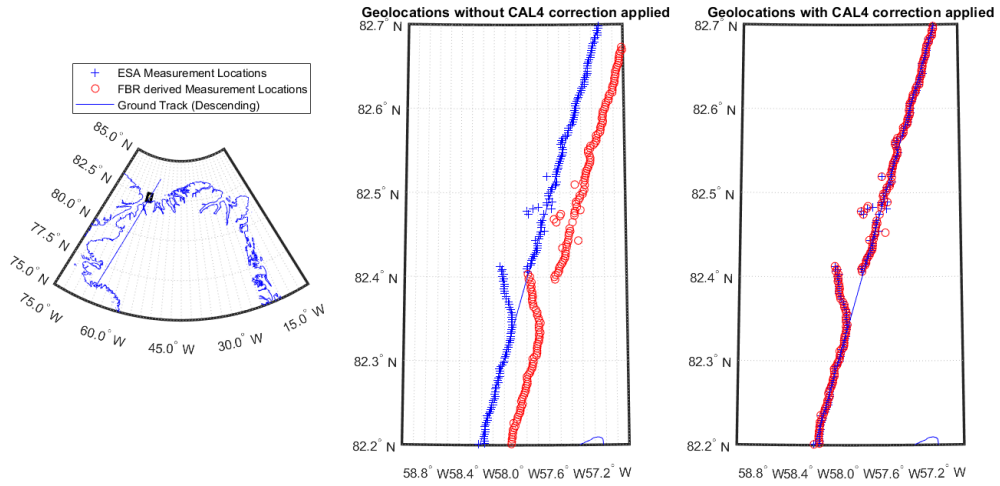

Figure 5.13: Geolocations derived from the FBR derived Phase Differences as well as the ESA L1b Phase Differences

FBR derived L1b, a rough verification is performed. In this case three thresholds are used: 0.6,0.7,0.8. The MNP is set to 1 and 10 to give an indication into the amounts of data associated to this kind of retracker.

	DEM Comparison		IceBridge Comparison			
Thresh.; MNP; ESA/FBR	σ [m]	N	median [m]	μ_{IB}[m]	σ_{IB}[m]	N
0.6, 1 ESA	24.07	1594	0.0905	0.3382	6.085	129
0.6, 1, FBR	23.44	1640	0.1546	0.6649	7.370	140
0.7,1, ESA	24.06	1597	-0.1622	0.2233	5.932	134
0.7,1, FBR	23.10	1647	0.3481	1.055	7.223	143
0.8,1, ESA	23.87	1592	0.0122	0.3869	5.553	130
0.8,1, FBR	23.06	1637	0.2019	1.269	6.244	141
0.6,10, ESA	14.17	8429	-0.1527	0.04096	8.253	768
0.6,10, FBR	14.41	8448	-0.0909	0.07954	8.682	788
0.7,10, ESA	14.22	8465	-0.0909	0.1245	7.896	763
0.7,10, FBR	14.22	8772	-0.0132	0.1848	8.097	787
0.8,10, ESA	14.38	8453	-0.1084	0.4863	8.577	785
0.8,10, FBR	14.06	8784	0.0427	0.5548	8.160	800

Table 5.1: Verification results following from threshold retracking of the ESA L1b waveforms and the FBR derived Waveforms. Thresh is the Threshold percentage applied and MNP is the Max. number of peaks that are picked out of a waveform.

It can be seen from the results as listed in table 5.1 that they compare well w.r.t. the DEM. Approximately the same number of measurements are found for both datasets, as well as standard deviation following from the DEM comparison.

However, the ESA L1b waveforms give slightly better results when compared to the FBR derived waveforms. This is shown by the lower μ_{IB} and σ_{IB} following from the IceBridge comparison. It should be noted though that lower amounts of data points are associated with the IB comparison. Outliers can have a large influence on the eventual statistics. When MNP is increased to 10 the differences in μ become smaller.

It should be noted here that the amount of data points as produced for a MNP of 1 is the amount of data points that would be found over the Petermann Glacier when only the POCA is retracked. This amount of POCA data points is approximately equal to the amount of data points as used in the research of Gourmelen as POCA comparison to the Swath Processed L2 data points, as shown in table 4.2. It is thus expected that the area of interest as defined in this thesis and the period of time over which the analysis is fulfilled is approximately the same as done by Gourmelen et al. (2017).

5.3.2. Unfiltered L2 Swath

The input to the optimization scheme is the unfiltered L2 Swath data. This data follows from Swath Processing without setting any restrictions to coherence, across-track angle or power. The input to swath processing consists both for the FBR as well as the ESA L1b derived products of 2187 bursts, coming from the 21 different orbits, as shown in figure 5.1. These orbits are Swath Processed separately and eventually combined to form one large set of measurements covering the Petermann Glacier. The amount of data points will be discussed in the following. Furthermore, the resulting FBR derived Coherence, Power and Across-track distributions will be compared to the ESA L1b derived values, as verification.

Amount of unfiltered L2-Swath It was found that per orbit less data was produced from the FBR derived products as compared to the L2-swath data derived from the ESA L1b when the interpolated window delay was used as applied in the SCOOP processing (Cipollini, 2016). The effects of picking the window delay corresponding to the maximum power sample resolved this issue. Both distributions are shown in figure 5.14.

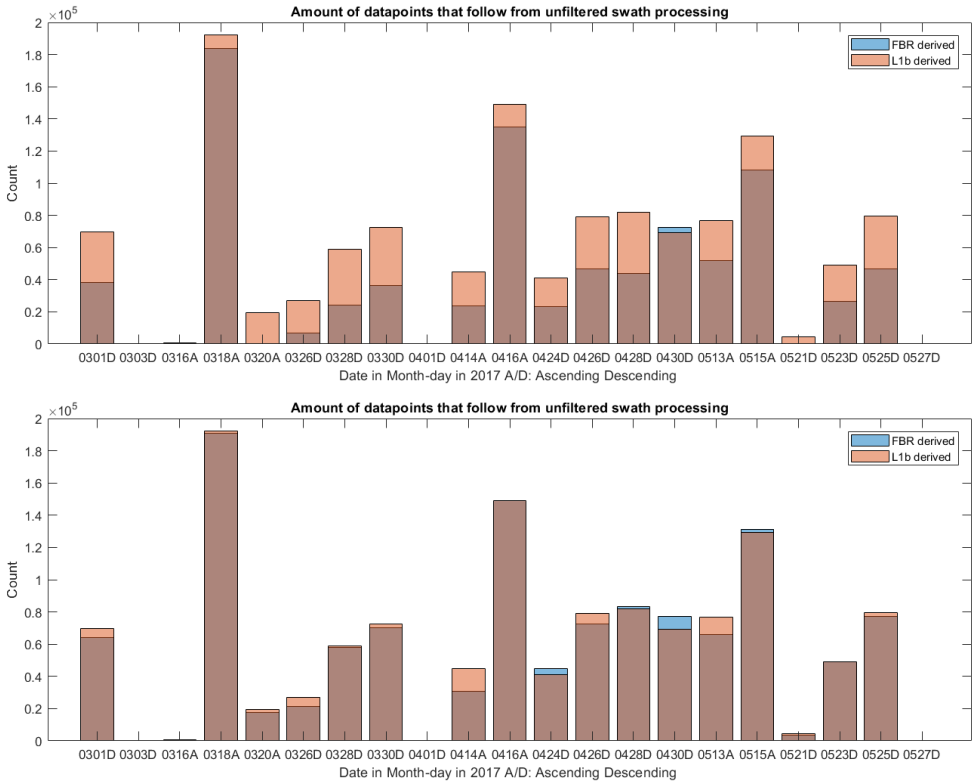

Figure 5.14: The relative amount of data produced by the FBR to L2 processing per orbit without any swath filtering settings applied. In the top the case is shown where the interpolated version of the Window Delay Correction is applied, whereas the bottom shows the Window Delay Correction applied case of the Maximum power stack sample.

The differences in amounts of data points per orbit is clearly visible, when looking at the unfiltered L2-Swath results corresponding to one orbit pass over the Petermann Glacier, as shown in figure 5.15. It is shown that the lack of data is present after the satellite, in descending orbit, has crossed the cliff. It is shown as well that the location corresponds to the data gap as is shown in figure 5.1.

Coherence The coherence values are shown in figure 5.16. It can be seen that a peak exist at the coherence value equal to '1'. It was found that these waveform samples are set to '1' as a default value, probably as a consequence of one of the geometry corrections, that ESA applies. The coherence values are filtered out when they are exactly equal to 1.

Furthermore, more measurements are found at lower coherence values for the FBR derived dataset, where at higher coherence values more ESA L1b measurements are found. It could be that these low coherence values are filtered out by ESA within the FBR to L1b processing.

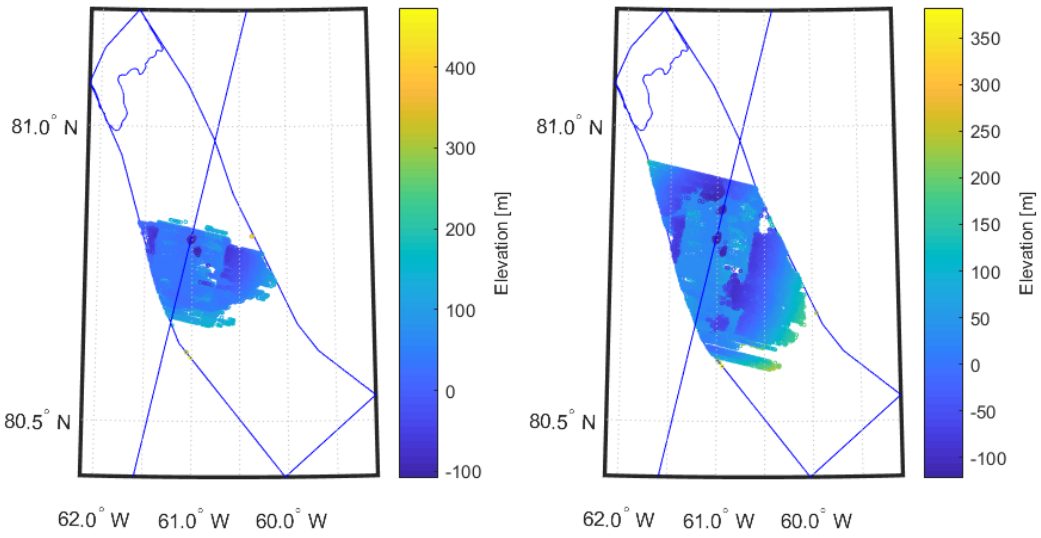

Figure 5.15: The 30/03/2017 Cryosat-2 overpass of the Petermann Glacier and the resulting unfiltered L2-Swath Heights. On the left the results are shown corresponding to the Own L1b derived elevations, and to the right the ESA L1b derived elevations. Clearly, a difference is present in amount of data present.

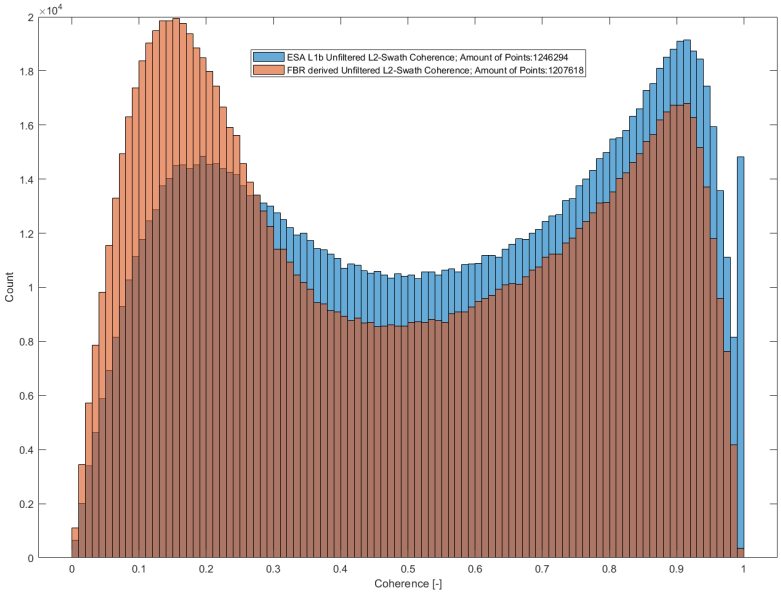

Figure 5.16: Distribution of FBR derived Coherence values before Swath Processing filter is applied.

As can be seen in figure 5.17, the coherence distributions and their geographical locations do still differ. However, the geographic distribution does show similarities.

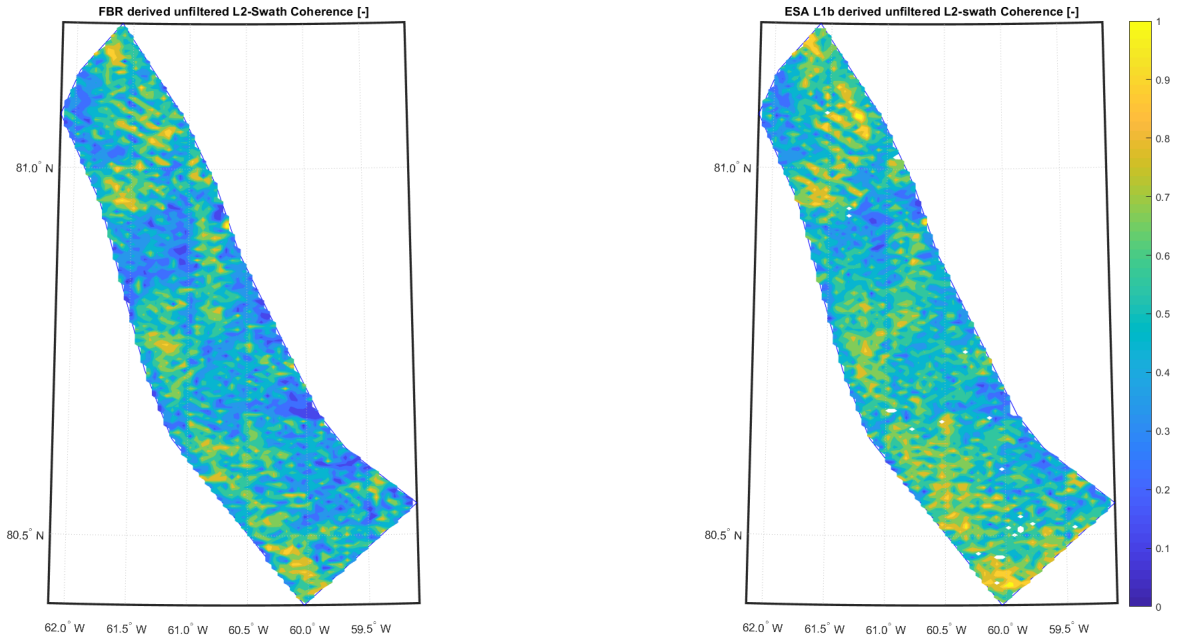

Figure 5.17: Geographical Coherence distribution over Petermann Glacier, as present in the unfiltered L2-swath product derived from the FBR product (left) and as provided within the ESA L1b product (right)

Across-track angle The across-track angle distribution over the Petermann Glacier is shown in figure 5.18 on the left. As can be seen the overall distributions follow the same shape. Apart from the main peak at nadir across-track angle two smaller peaks are found at |0.54| [Deg]. This angle corresponds to a phase difference of $|\pi|$. It is not known why the algorithm finds these large measurements at these locations besides nadir. It could be related to the phase wrapping and unwrapping that occurs at these exact angles.

A difference that can be observed is the higher amount of ESA L1b derived across-track angles which are larger than |0.54| [Deg], whereas there seem to be more FBR derived across-track angles lower than |0.54| [Deg].

Power The power distributions for both L2-swath datasets are shown in figure 5.18 on the right. As can be seen, a large portion of the entire normalized power dataset (>80%) is lower than 0.1. This is the case for both the ESA L1b dataset as well as the FBR derived dataset. No big differences are found further, between the two different power distributions.

5.3.3. Filtered L2-Swath

As can be seen from the distributions of the swath threshold variables some differences remain. In order to verify that the threshold variables are calculated correctly, it is checked by applying swath processing. If similar elevation results are found when applying the same thresholds to ESA L1b unfiltered L2-Swath and FBR derived unfiltered L2-Swath, it is proven that the variables are calculated correctly. This is shown for certain random threshold settings in table 5.2.

As can be seen the results from swath processing ESA L1b and FBR derived waveforms, are in agreement. Even at lower coherence thresholds where the coherence values vary most, similar results are found.

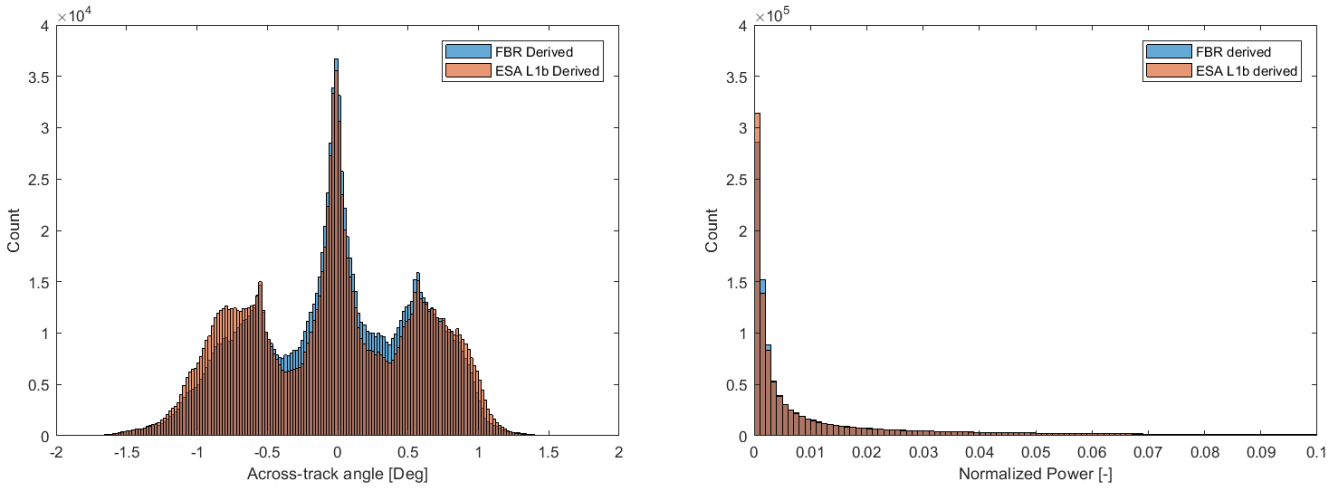

Figure 5.18: Distribution of FBR derived Across-track angles [Deg] and Power values before Swath Processing filter is applied.

Thresholds Power; Coherence; θ_{ac}	DEM Comparison σ_{DEM} [m]	N_{meas}	IB Comparison median [m]	μ_{IB} [m]	σ_{IB} [m]	N_{IB}
0.25; 0.65; 0.2; ESA	6.442	49692	-0.5536	-0.4106	5.008	4247
0.25; 0.65; 0.2; FBR	6.370	48053	-0.5533	-0.4447	4.743	4064
0.2; 0.65; 0.2; ESA	6.703	56968	-0.6332	-0.5679	5.308	4840
0.2; 0.65; 0.2; FBR	6.5902	54805	-0.6397	-0.5714	4.956	4588
0; 0.8; 0.8; ESA ∗	7.381	292934	0.0324	0.1335	6.436	25941
0; 0.8; 0.8; FBR ∗	6.947	227021	0.1789	0.7950	5.767	19621
0; 0.85; 0.8; ESA ∗	7.1691	221400	0.0879	0.2712	6.018	19147
0; 0.85; 0.8; FBR ∗	6.875	162336	0.2137	0.8860	5.546	14043
0.3; 0.3; 0.3; ESA	6.909	67220	-0.6308	-0.5502	6.358	6280
0.3; 0.3; 0.3; FBR	6.885	68372	-0.6167	-0.4500	6.356	6259
0.8; 0.8; 0.8; ESA	7.215	4456	-0.1373	0.2408	3.475	367
0.8; 0.8; 0.8; FBR	7.299	4350	-0.2790	-0.06039	2.815	372
0.2; 0.1; 0.2; ESA	7.098	78503	-0.9040	-1.064	6.620	7238
0.2; 0.1; 0.2; FBR	7.105	80502	-0.8465	-0.9171	6.548	7218

Table 5.2: Verification results following from Swath processing of ESA L1b and FBR derived L1b waveforms. The ∗ denotes cases in which data editing is applied, at a filtering setting of 50 [m] (See chapter 6).

6

Validation

An FBR to L1b processor has been developed up to this point. The result as produced in chapter 5 will serve as baseline. Different runs will be performed with the FBR to L1b processor while altering certain input parameters. The results will be analysed and presented.

6.1. Basic L2-Swath validation

Within this section the L2 swath elevations will be compared to the GIMP DEM and the IceBridge laser altimetry data. This will be done for both the ESA L1b derived L2 Swath measurements as well as the FBR derived L2 swath measurements. The optimization will be run for both unfiltered L2 swath datasets. Before running the optimization the input datasets will be compared. Consequently, the optimization results will be presented.

6.1.1. FBR to L1b processing settings

A reference dataset will be processed with the following FBR input settings. In the following sections these settings will be changed to observe the differences with this reference.

- Initially, the DEM is **not** applied in surface location computation and application of Geometric Corrections. Instead, the window delay as provided in the FBR product is used.
- The 64 "nearest" points are defined by the size of the beam angle and not on the absolute distance to the surface location.
- The SSW criterium is set to an angle of **0.7 [Deg]**. This criterium is based on the same criterium as has been applied on the ESA Baseline C L1b products.
- The Window Delay Correction is applied, by setting the reference window delay equal to the window delay corresponding to the stack sample with the highest power. The motivation behind this choice is explained in chapter 5.
- In the azimuth processing step, the beam steering step is applied in the exact or approximate manner based on the surface roughness. The surface roughness is defined as the standard deviation of the ellipsoidal heights at the surface locations corresponding to the burst that is processed. These heights follow from the DEM or from the window delay, dependent on the first item in this list. This roughness is compared to a **roughness threshold of 40 [m]**.
- The weighting window that is applied during azimuth processing is a **Hamming** window.

6.1.2. L2-Swath validation

For data acquired over the period of March till May 2017 over the area of the Petermann Glacier, the L2-Swath Heights derived from ESA L1b will be compared to the L2-Swath Heights derived from the raw FBR product. The DEM that is used for comparison is the GIMP DEM NSIDC-0715, which is a model comprising data from January 2009 until December 2015 (Howat et al., 2014). The Swath Processing thresholds for the single

pass are set by optimization as described in section 4.2.5. These settings are set individually for the swath processing of both datasets.

Running the optimization analysis, thresholds are found for both L2-Swath derived from ESA L1b data (L1b ESA), and L2-Swath derived from the raw FBR data (L1b Own). The results are listed in table 6.1:

Optimization Criterion	$\sigma_{DEM}/log(N_{meas})$		σ_{DEM}	
Settings	ESA L1b	Own L1b	ESA L1b	Own L1b
Power	0.25	0.20	0.6	0.55
Coherence	0.65	0.65	0.7	0.7
Across-track Look angle	0.20	0.20	0.20	0.20
Min. Criterion	1.3978	1.3855	6.4058	6.4314
Corresp. N_{meas}	49572	54588	12973	15744
Corresp. σ_{DEM} [m]	6.5628	6.5632	6.4058	6.4314

Table 6.1: Input settings for the Swath Processing

Data Editing	No		Yes, 50 [m]		Yes, 75 [m]		Yes, 25 [m]	
Settings	ESA L1b	Own L1b	ESA L1b	Own L1b	ESA L1b	Own L1b	ESA L1b	Own L1b
Power	0.25	0.20	0	0	0.25	0	0	0
Coherence	0.65	0.65	0.85	0.8	0.65	0.8	0.80	0.80
Across-track Look angle	0.20	0.20	0.80	0.80	0.20	0.60	0.80	0.80
Min. Criterion	1.4028	1.3907	1.3412	1.2970	1.3799	1.3612	1.2274	1.1902
Corresp. N_{meas}	49706	54805	221400	227021	49699	183156	290635	225096
Corresp. σ_{DEM} [m]	6.588	6.590	7.1691	6.9470	6.4806	7.1640	6.7059	6.3703

Table 6.2: Input settings for the Swath Processing

When comparing the results for the L1b Own and the L1b ESA, it can be seen that a slightly lower optimum Criterium is found for the FBR derived elevations. In this case, when optimized for $\sigma_{DEM}/logN_{meas}$ more points and a lower standard deviation is found for the FBR derived surface heights, than for the ESA L1b derived heights. The higher amount of data points which are found in the case considering Own L1b is thought to be mainly related to the lower power threshold equal to 0.2. In case the same thresholds are applied, as shown as first on the list in table 5.2, less Own L1b points are found. When comparing results it shows that 6000 points are located in the region covering power values of 0.2 to 0.25. This amount affects the criterium.

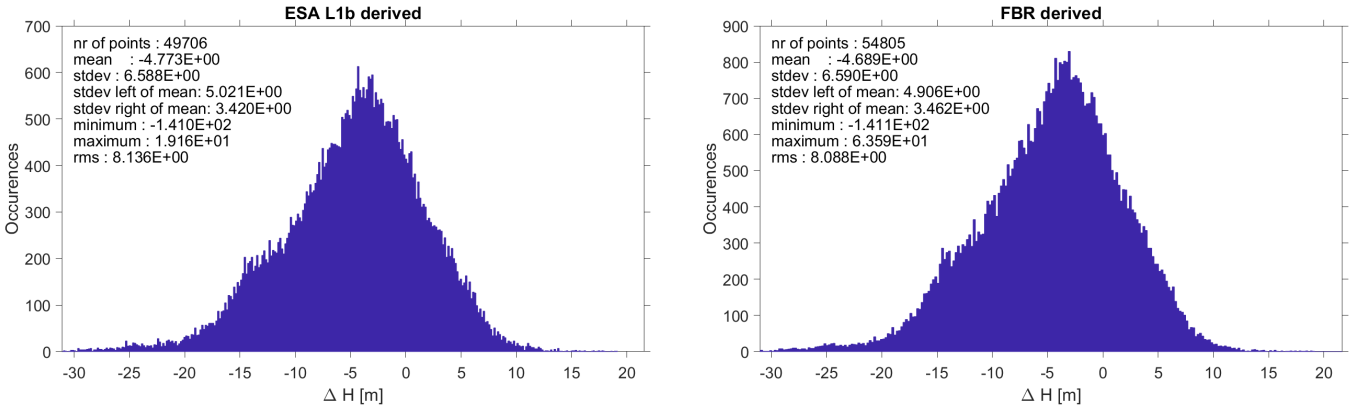

Figure 6.1: Distribution of differences between measured elevations and DEM elevations over Petermann Glacier, when optimized for $\sigma_{DEM}/log(N_{meas})$.

The distributions corresponding to the differences between the Cryosat-2 and the DEM are shown in figure 6.1. The negative mean shows that the Cryosat elevations are on average lower than the DEM elevations.

The optimal swath filter settings as found in previous section will now be implemented. The resulting elevations are compared to the IceBridge laser altimetry points to show the exact validity. The essential variables resulting from this comparison are listed in table 6.3, whereas the distributions are shown in figure 6.2. It should be noted that N denotes the amount of data points that fulfil the 50 [m] horizontal displacement requirement, and thus are used for the comparison.

It can be seen that a slightly lower mean and median are found for the FBR derived dataset. This is the case as well for the standard deviation, which is 5 [cm] smaller in case of the Own L1b. In contrast, the amount of data points is higher for the FBR derived Own L1b elevations. In both cases this is equal to around 8% of the total amount of Cryosat-2 measurements, which followed from the optimization.

Optimization Criterion	$\sigma_{DEM}/log(N_{meas})$		σ_{DEM}	
Parameters	ESA L1b	Own L1b	ESA L1b	Own L1b
Median [m]	-0.5536	-0.6397	-0.1737	-0.1380
μ_{IB} [m]	-0.4106	-0.5714	0.2753	0.2452
σ_{IB} [m]	5.008	4.956	4.051	3.961
N	4247	4588	1212	1517

Table 6.3: Results from the CS to IB comparison for the two criteria used in the optimization. N denotes the number of CS measurements that was compared with an IB measurement.

Data Editing	No		Yes, 50		Yes, 75	
Parameters	ESA L1b	Own L1b	ESA L1b	Own L1b	ESA L1b	Own L1b
Median [m]	-0.5536	-0.6397	0.0879	0.1789	-0.5536	0.2183
μ_{IB} [m]	-0.4106	-0.5714	0.2712	0.7950	-0.4106	0.8796
σ_{IB} [m]	5.008	4.956	6.018	5.767	5.008	6.085
N	4247	4588	19147	19621	4247	15784

Table 6.4: Results from the CS to IB comparison for the two criteria used in the optimization. N denotes the number of CS measurements that was compared with an IB measurement.

Data Editing	No		Yes, 50	
Parameters	ESA L1b	Own L1b	ESA L1b	Own L1b
Median [m]	-0.5536	-0.6397	0.0879	0.1789
μ_{IB} [m]	-0.4106	-0.5714	0.2712	0.7950
σ_{IB} [m]	5.008	4.956	6.018	5.767
N	4247	4588	19147	19621

Table 6.5: Results from the CS to IB comparison for the two criteria used in the optimization. N denotes the number of CS measurements that was compared with an IB measurement.

Data Editing	No		Yes, 50		Yes, 75		Yes, 25	
Parameters	ESA L1b	Own L1b	ESA L1b	Own L1b	ESA L1b	Own L1b	ESA L1b	Own L1b
Median [m]	-0.5536	-0.6397	0.0879	0.1789	-0.5536	0.2183	0.0330	0.1789
μ_{IB} [m]	-0.4106	-0.5714	0.2712	0.7950	-0.4106	0.8796	0.1903	0.7136
σ_{IB} [m]	5.008	4.956	6.018	5.767	5.008	6.085	5.690	5.175
N	4247	4588	19147	19621	4247	15784	25757	19518

Table 6.6: Results from the CS to IB comparison for the two criteria used in the optimization. N denotes the number of CS measurements that was compared with an IB measurement.

The distributions of the IceBridge comparison are shown in figure 6.2. These distributions do show to be more noisy, due to a decrease in the amount of data points. It can be seen as well that the absolute differences are not larger than 30 [m], in both cases.

Data editing during optimization In order to check the effect of outliers on the eventual results, all data points with an absolute difference between derived surface height and DEM height larger than 50[m] are

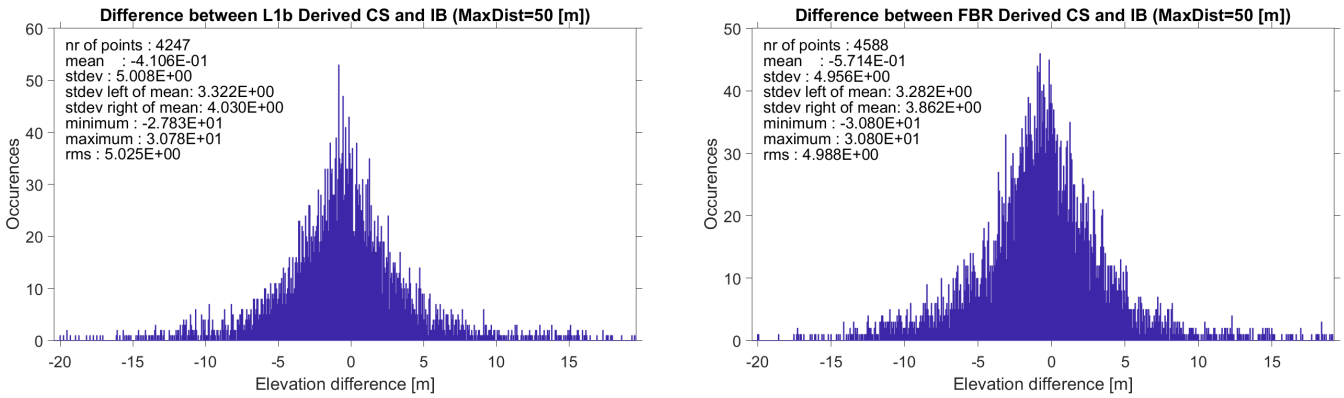

Figure 6.2: Distribution of differences between measured elevations and IceBridge elevations over Petermann Glacier, when optimized for $\sigma_{DEM}/log(N_{meas})$ and with outlier data editing applied.

edited out. This is done during optimization. The results from the optimization are shown in table 6.7.

Optimization Criterion	$\sigma_{DEM}/log(N_{meas})$		σ_{DEM}	
Settings	ESA L1b	Own L1b	ESA L1b	Own L1b
Power	0.0	0.0	0.4	0.4
Coherence	0.85	0.8	0.7	0.7
Across-track Look angle	0.8	0.8	0.2	0.2
Min. Criterion	1.3412	1.2970	6.2782	6.2590
Corresp. N_{meas}	221400	227021	28105	27075
Corresp. σ_{DEM} [m]	7.1691	6.9470	6.2782	6.2590

Table 6.7: Input settings for the Swath Processing with data editing applied

In this case a lower optimal Coherence setting is found for the Own L1b dataset in comparison to the ESA L1b dataset, when optimized for $\sigma DEM/log(N_{meas})$. Furthermore, in contrast to the unedited case the power threshold is not used entirely, whereas the across-track angle is relaxed. The amount of measurements after data editing is found to be ~4 times higher than without data editing applied, while the standard deviations go up by 0.5 [m]. This combination results in a lower optimal criterium than compared to the case without data editing, for both the ESA L1b and Own L1b cases.

The lower Own L1b filter settings for Coherence in case of the $\sigma_{DEM}/log(N_{meas})$ criterium, could be explained by the difference in coherence distribution as shown in figure 5.16. In order to optimize for a higher N_{meas} the filter settings for coherence are relaxed.

The elevation difference with respect to the DEM distributions as shown in figure 6.3, show two peaks. The left, more negative peak is expected to be related to a missing chunk of glacier, which was still present in the period the DEM was created.

Optimization Criterion	$\sigma_{DEM}/log(N_{meas})$		σ_{DEM}	
Parameters	ESA L1b	Own L1b	ESA L1b	Own L1b
Median [m]	0.0879	0.1789	-0.3631	-0.3625
μ_{IB} [m]	0.2712	0.7950	-0.0977	-0.1308
σ_{IB} [m]	6.018	5.767	4.211	3.944
N	19147	19621	2498	2381

Table 6.8: Results from the CS to IB comparison for the two criteria used in the optimization. N denotes the number of CS measurements that was compared with an IB measurement.

The results in table 6.8 show that small differences still exist between the ESA L1b derived L2-swath and the FBR derived L2-swath. Nevertheless, the results approach each other. It is remarkable that the results are not on average negative, as is expected due to the difference in penetration depths in radar versus laser

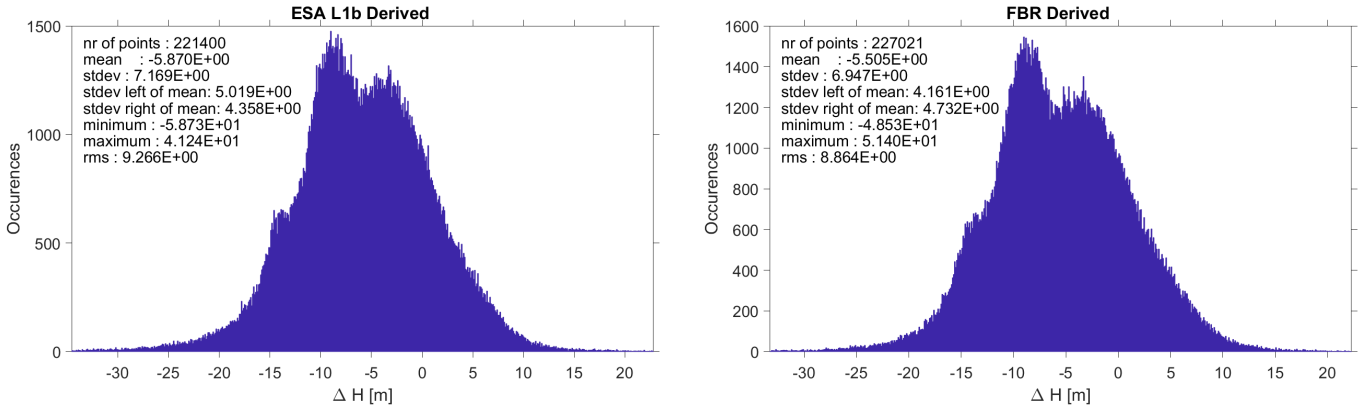

Figure 6.3: Distribution of differences between measured elevations and DEM elevations over Petermann Glacier, when optimized for $\sigma_{DEM}/log(N_{meas})$ and with outlier filtering applied.

altimetry when measuring over ice, as is shown by Gourmelen et al. (2017). Furthermore, a similar single peak is presented as shown in Gourmelen et al. (2017) when looking at the CS-IB differences in figure 6.4.

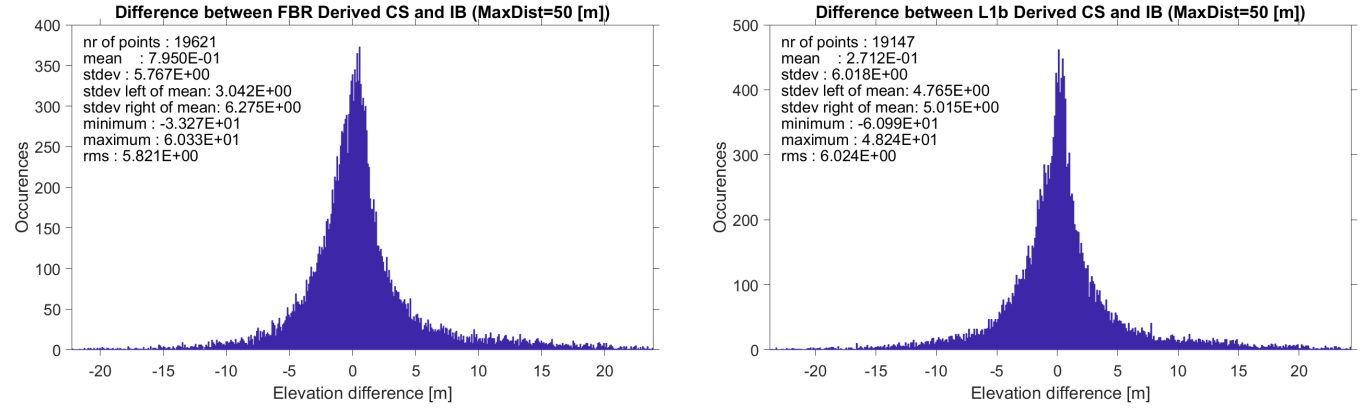

Figure 6.4: Distribution of differences between measured elevations and IceBridge elevations over Petermann Glacier, when optimized for $\sigma_{DEM}/log(N_{meas})$ and with outlier filtering applied.

Distance and Time Difference As was previously stated, the maximum allowed distance between a Cryosat L2-Swath Measurement and a IceBridge laser altimetry data point is set to 50 [m]. The time difference between two measurements which are compared is not limited. However, the maximum time between the two types of measurements can reach 60 days. It needs to be checked whether the measured elevation differences do not show a distinct distance or time relationship.

In figure 6.5 and figure 6.6 the IB differences as function of Time in days and Horizontal Distance [km] is shown for the edited and non-edited cases. When looking at mean values per day and per [m] horizontal distance, it can be concluded that there exists no relation between the IB differences and these two variables.

L2-Swath height to IceBridge Height difference as function of Thresholds The resulting L2-Swath to IB differences are shown as function of the three thresholds are considered here.

The distributions of the IB differences in case all filter settings are set to 0 are shown in figure 6.7. No filtering has taken place yet. Some differences can be distinguished. More positive CS-IB elevation differences are found in the FBR case, compared to the ESA L1b case. Furthermore, the larger difference are mostly found at low normalized power values.

The distributions as shown in figure 6.8 correspond to the unedited case, as presented in tables 6.3 and 6.1. No distinct difference can be observed in the unedited case. The distributions as shown in figure 6.9

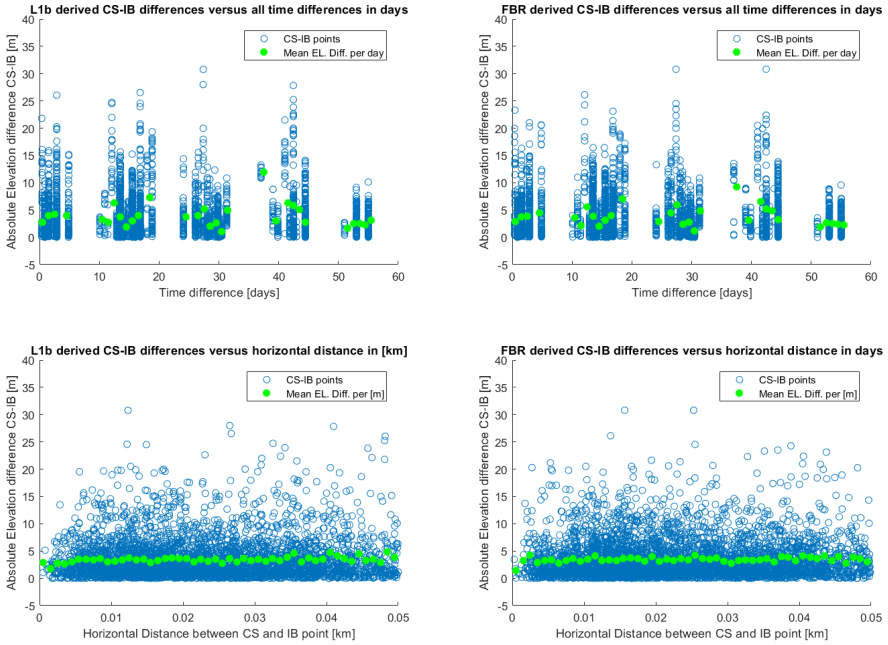

Figure 6.5: Distribution of L2-Swath to IB elevation differences as function of time in days and distance [km]. The fitted line shows the L2-Swath to IB difference in [m] per [km] horizontal distance. No data editing is applied

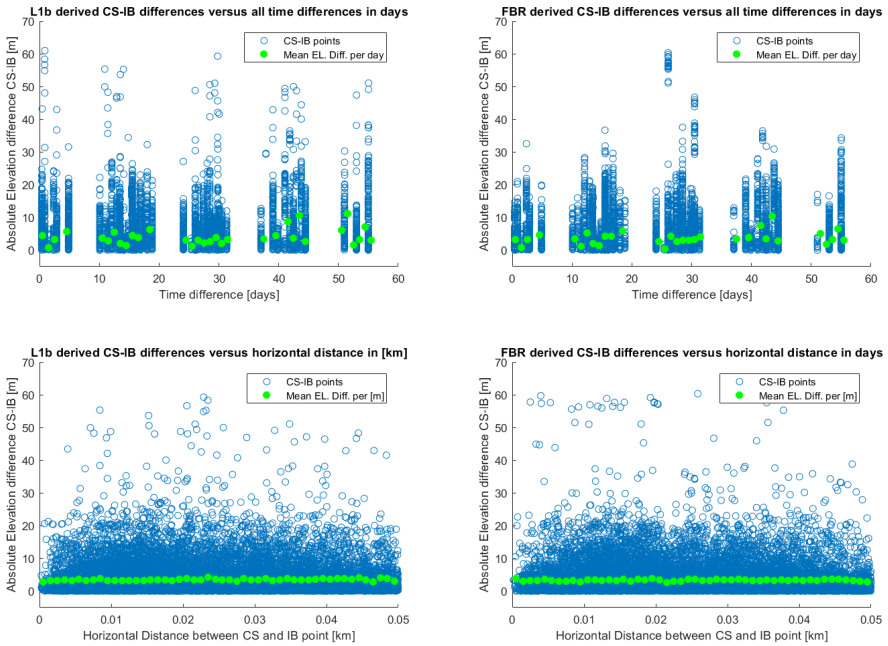

Figure 6.6: Distribution of L2-Swath to IB elevation differences as function of time in days and distance [km]. The fitted line shows the L2-Swath to IB difference in [m] per [km] horizontal distance. Data editing is applied.

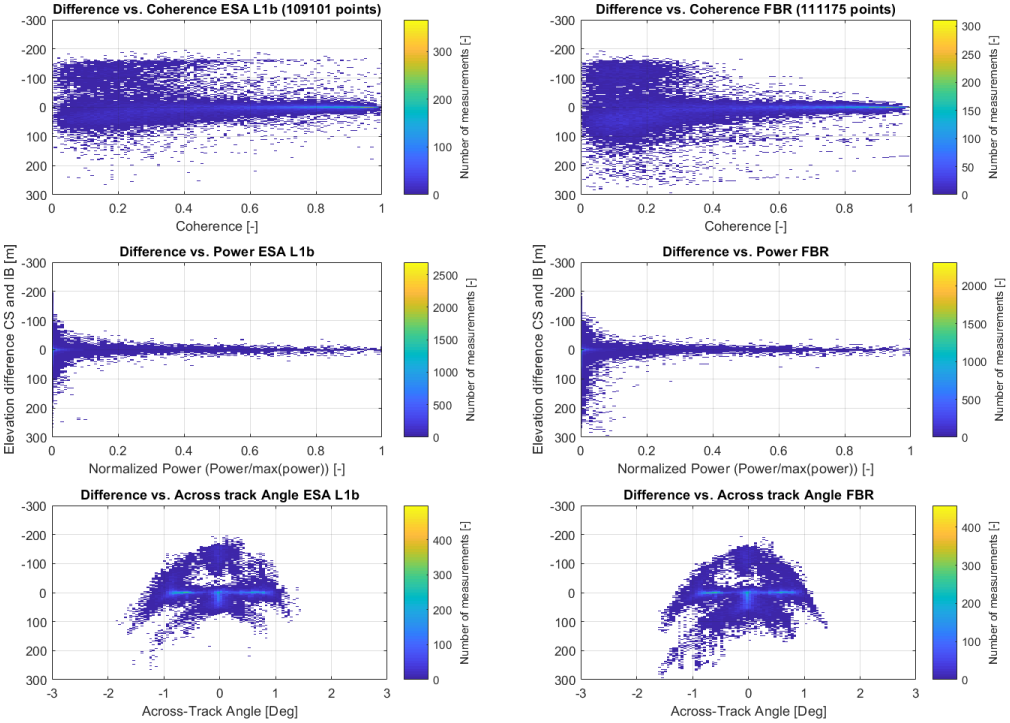

Figure 6.7: Scattered distributions of CS to IB difference as function of Coherence, normalized power and Across-track angle, before the swath processing filter is applied.

correspond to the data edited case, as presented in tables 6.8 and 6.7.

When comparing these differences as function of coherence, it is shown that the ESA L1b derived L2-Swath IB differences show more negative outliers, whereas the FBR derived L2-Swath to IB differences show more positive outliers. It is shown as well that the higher the coherence, on average the difference values become smaller. Nevertheless, the high coherence L1b derived L2-Swath differences show bigger differences than the FBR derived L2-Swath to IB differences.

When looking at the power versus IB difference, it can be observed that the lower the power the larger the difference. This proves why the unfiltered optimization finds an optimum at a power threshold of 0.2 [-]. Furthermore, the absolute largest outliers for both ESA L1b and FBR derived L2-Swath correspond to small power values.

The IB differences shows a similar distribution as function of the across-track angle in the ESA L1b case versus the FBR derived case. However, it is clear that less negative outliers are present at larger across-track angles in the FBR case.

6.2. Improvement of results

In this section the impact is tested on the results, of changing 3 different parameters. First a short description will be given on the alterations applied, and consequently the results will be presented.

6.2.1. Alterations

Three different types of alterations are applied in order to improve the results. Firstly, the power thresholds as used in the optimization will be refined in the region close to zero. Secondly, the application of a DEM during FBR to L1b processing will be tested. Lastly, the beam selection, based on the along track angle, will be varied. The argumentation will be explained shortly in the following sections after which the results will be presented.

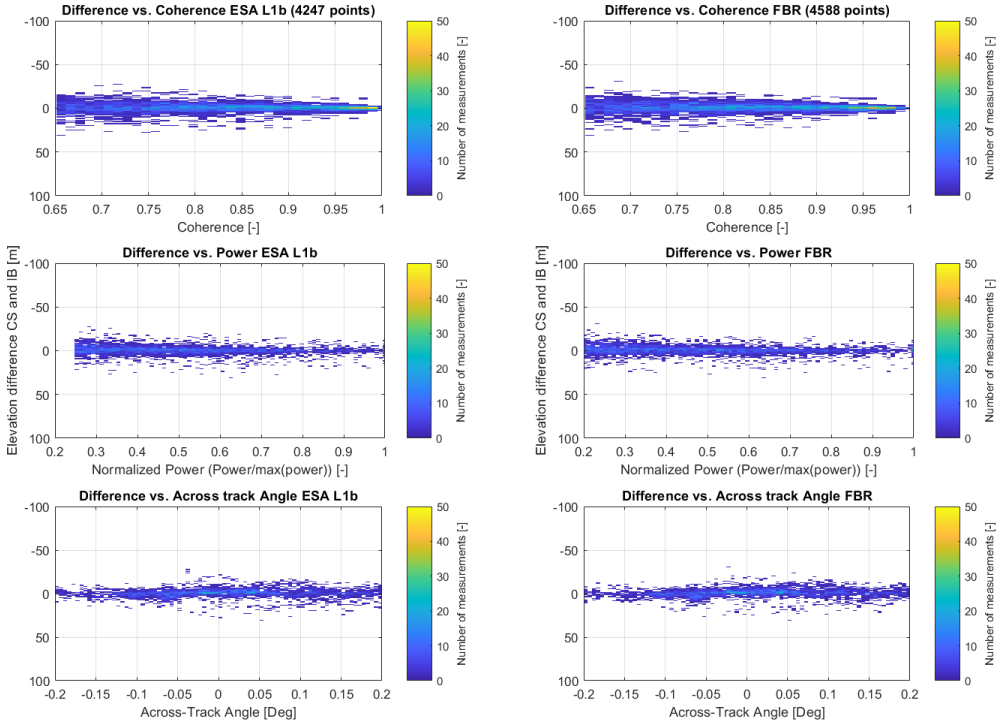

Figure 6.8: Scattered distributions of CS to IB difference as function of Coherence, normalized power and Across-track angle, after the Swath processing optimization is performed without data editing

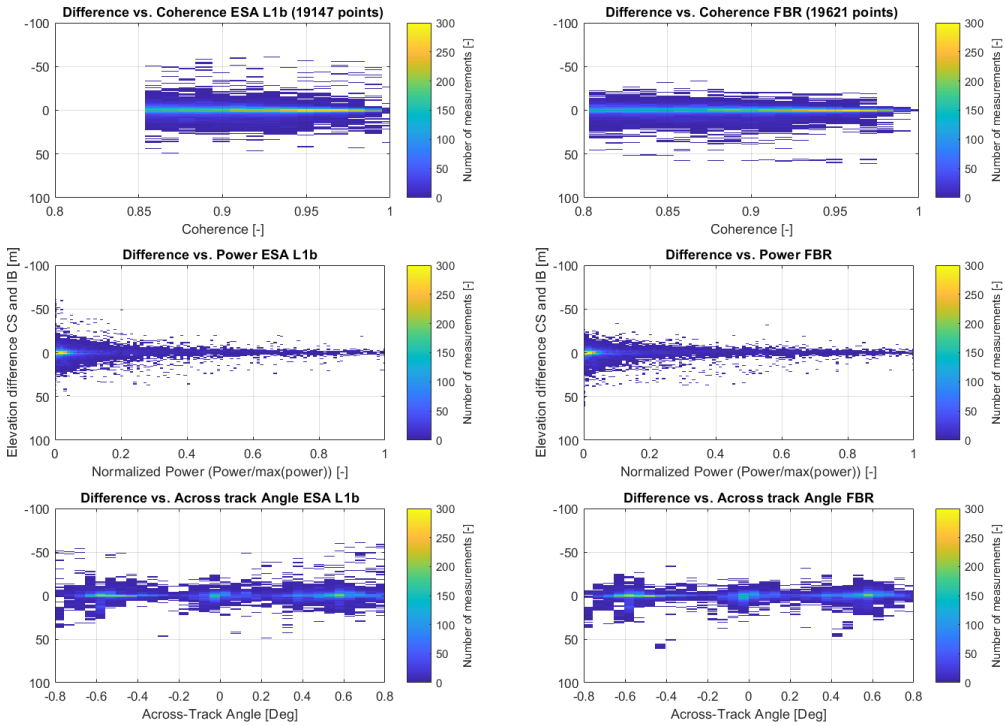

Figure 6.9: Scattered distributions of CS to IB difference as function of Coherence, normalized power and Across-track angle, after the Swath processing optimization is performed with data editing

Refined Power thresholds It was found that the size of the L2-Swath to IceBridge Elevation differences increased towards lower power. It was shown as well that most of the samples, more than 80 %, is lower than 0.1. At the same time, the optimization, in the filtered case finds its optimal criterium when no power filtering is applied at all. This might be due to the fact that the power threshold steps are too rough. By refining the power thresholds from 0 till 0.1, new optima can be found.

Application of DEM The FBR to L1b processing algorithm gives the option to implement a Digital Elevation Model. Consequently, this DEM is used to compute the surface locations, as well as the slant range correction. When no DEM is implemented the window delay is used instead. From the window delay an elevation is determined, and interpolated to the surface locations. In case a DEM is implemented, the DEM is interpolated to the surface locations. It is expected that implementing a DEM increases the quality of the product.

Variation of along track angle During the generation of the stacks a Sample Stack Weighting (SSW) is applied. Dependent on the SSW criterium beams within the stack are filtered out.

As an example the behaviour of a set of waveforms over the Petermann Glacier for one orbit is shown when the beam selection criterium is changed. The effect can be seen in figure 6.10. When a less strict beam selection criterium is applied, it can be seen that the set of waveforms that seem to be affected by the large drop in topography becomes smaller. This is caused by an increase of stack samples that are combined within the multi-looking of the stacks. Changing the SSW angle thus is seen to have the highest effect in regions where high topographic variations are present, due to the smaller size of the stacks.

Due to a stricter SSW along-track angle less beams make up a stack. A drawback of making the beam selection criterium more strict is the loss of looks within a stack. Due to the multi look speckle reduction is achieved. When there are less looks over which to average, more speckle will be present in the waveform.

6.2.2. Results

The results will be presented for the unedited as well as the edited case. As in the unedited case no power thresholds equal to zero followed from the optimization, no extra refinement of the power thresholds is applied.

Case without Data editing The results following from the unfiltered case are shown in tables 6.9 and 6.10. A few remarks can be given on these results:

- The threshold values vary around the same values. The across-track angle threshold is always set to 0.2, whereas the Coherence and Power Thresholds vary in between 0.6 to 0.65 and 0.2 to 0.15 respectively. The lower Power threshold is located at the lowest SSW along track angle. This could be explained by the fact that at this low along-track angle less low powered signals contribute to the eventual result. However, as was seen in figure 5.18, relaxing this filter does include a lot more data points, as most of the data points are located in the lower power regions. As a consequence, the coherence threshold goes up to filter out some extra low power errors.
- The minimum optimization criterium for both without DEM and with DEM can be found at a SSW angle of 0.6 [Deg]. This criterium is lower than the Criterium found for ESA.
- The lowest standard deviation of the L2-Swath to IB differences with and without DEM can be found at a SSW angle 0.7 [Deg]. These Standard deviations are on average smaller for the unfiltered case in which a DEM is used, and are in that case lower than the standard deviations found for the ESA L1b derived IB differences.
- The means and median of the IB differences are all negative. This is expected, due to the difference in penetration depth between Laser and Radar signal interaction with ice or snow. This was shown as well by Gourmelen et al. (2017). The medians are mostly more negative than the mean values. This difference is most probably caused by a plurality of positive outliers. Similarly, the mean and median values are all more negative compared to the ESA L1b result.
- At high and low along-track angle SSW values the standard deviation of the differences goes up. This could be related to less noise reduction at the low SSW angles, due to less looks, and due to the contribution of ambiguities in the high angle SSW area.

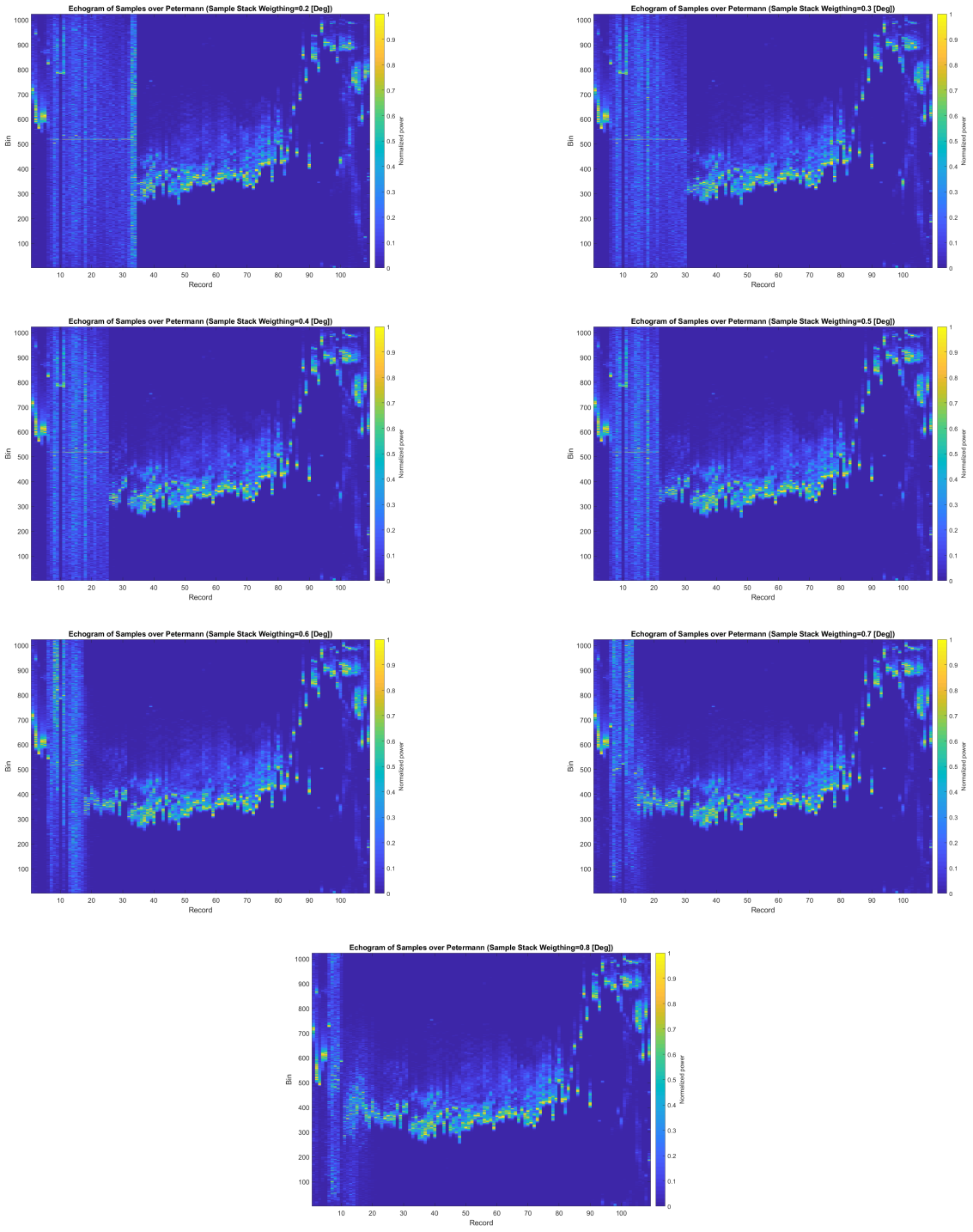

Figure 6.10: Sequence of Echograms over Petermann glacier, when along-track beam stack weighting goes from 0.2 [deg] (top left) to 0.8 [deg] (bottom)

No DEM, unfiltered	SSW angle [Deg]	0.8	0.7	0.6	0.5	0.4	0.3	0.2	ESA(0.7)
Optim. for $\frac{\sigma_{DEM}}{log(N_{meas})}$	Coh.	0.65	0.65	0.6	0.65	0.6	0.6	0.65	0.65
	Pow	0.2	0.2	0.2	0.2	0.2	0.2	0.2	0.2
	θ_{ac}	0.2	0.2	0.2	0.2	0.2	0.2	0.2	0.2
	σ_{DEM}	6.6441	6.5902	6.6277	6.5812	6.6982	6.7520	6.8629	6.5883
	N_{meas}	54438	54805	59226	52742	55499	51855	43624	49706
	Crit.	1.4029	1.3907	1.3887	1.3937	1.4118	1.4321	1.4792	1.4028
IB	Median	-0.6213	-0.6379	-0.6341	-0.6560	-0.6994	-0.6088	-0.7299	-0.5536
	μ_{IB}	-0.5540	-0.5714	-0.5214	-0.5825	-0.5483	-0.5970	-0.7161	-0.4106
	σ_{IB}	5.009	4.956	5.380	5.058	5.450	5.446	5.280	5.008
	N_{IB}	4569	4588	5141	4563	5019	4674	4087	4247

Table 6.9: Results from the CS to IB comparison for the two criteria used in the optimization. N denotes the number of CS measurements that was compared with an IB measurement.

Yes DEM, unfiltered	SSW angle [Deg]	0.8	0.7	0.6	0.5	0.4	0.3	0.2	ESA(0.7)
Optim. for $\frac{\sigma_{DEM}}{log(N_{meas})}$	Coh.	0.65	0.65	0.65	0.65	0.6	0.6	0.65	0.65
	Pow	0.2	0.2	0.2	0.2	0.2	0.2	0.15	0.25
	θ_{ac}	0.2	0.2	0.2	0.2	0.2	0.2	0.2	0.2
	σ_{DEM}	6.6751	6.5942	6.5560	6.5838	6.6839	6.7561	6.9162	6.5883
	N_{meas}	54424	54818	54355	53286	55291	51864	51210	49706
	Crit.	1.4095	1.3915	1.3866	1.3929	1.4093	1.4329	1.4686	1.4028
IB	Median	-0.6595	-0.6652	-0.6579	-0.6835	-0.7537	-0.6239	-0.7633	-0.5536
	μ_{IB}	-0.5539	-0.5532	-0.5837	-0.6235	-0.6782	-0.6209	-0.9341	-0.4106
	σ_{IB}	4.864	4.782	4.895	4.914	5.260	5.426	5.433	5.008
	N_{IB}	4535	4565	4601	4514	4873	4707	4705	4247

Table 6.10: Results from the CS to IB comparison for the two criteria used in the optimization. N denotes the number of CS measurements that was compared with an IB measurement.

Case with Data editing The results from the variation of FBR to L1b input settings to the eventual validation result, in case the optimization includes a filtering, are shown in tables 6.11 up to 6.14.

- A difference that can be observed in comparison is again the power thresholds close to zero, as was shown before. The across-track angle is almost for all analyses set to 0.8 [Deg]. This means that measurements are included which have undergone unwrapping, as the wrapped maximum phase difference π is equal to a angle of 0.54 [Deg]. This was not the case in the unfiltered case.
- The coherence thresholds increase from 0.8 to 0.85 with stricter along-track SSW angles. It should be noted here again, that coherence is an indication of the averaged correlation over a stack between the two phase measurements contributing to the phase difference. Due to the smaller stacks, at lower SSW angle, a high coherence is probably more easily achieved, but might not always indicate a high quality range measurement.
- The refined power threshold does improve the results, as expected. Higher power thresholds are found for the FBR derived product compared to the ESA L1b product. The power threshold when refined, decreases with the SSW along-track angle. This can be explained by the fact that less low powered beams contribute to the stack, when the along-track look is narrowed. A consequence is the substantial loss of data points at higher along-track angles.
- Lower optimum criteria are found for the filtered case than compared to the unfiltered case. The lowest optimum criteria are found at 0.4 or 0.5 SSW along-track angle. The lowest one, is found when a DEM is applied as well as the refined power threshold optimization.
- A remarkable difference with the unfiltered case are the higher mean and median values coming from the L2-Swath to IB comparison, as was seen before. The FBR derived, as well as the ESA L1b derived, means and median values are positive. This is unexpected as negative values are expected on average. The ESA L1b derived mean and median values are lower than the FBR derived ones. The means and

median values do as well show a lot of difference among each other. This might indicate the presence of a lot of outliers.

- The standard deviations following from the IB comparison are in each case lower for the FBR derived heights than for the ESA L1b derived heights.
- The best results, in terms of low mean and median IB comparison values, are found in the case where a DEM is applied, with a refined optimization grid for power. In this case the mean and median IB differences decrease with the SSW along-track angle.

6.3. Overall Validation Results

A lot of results are presented up to this point. In order to draw some conclusions, the main important findings regarding the validation will be discussed here. Two main comparisons were made in this chapter. These are the comparisons between the ESA L1b and the Own L1b derived L2-Swath elevations, and the comparison between these two and the result as presented by Gourmelen et al. (2017).

ESA L1b versus Own L1b derived L2 Swath Following the validation, it is shown that similar results are produced from the L2-Swath optimization for the ESA L1b and FBR derived products. No large discrepancies are found. The standard deviations do show an improvement over the ESA L1b derived L2-Swath, for as well the case with data editing as without. Following this method of optimizing for the filter settings, thus gives the best L2-Swath results when using the FBR derived Own L1b dataset.

The optimal filtering setting found for the ESA L1b and FBR derived products compare well. In the unedited case a difference is found in optimal power filtering setting: 0.2 for the Own L1b and 0.25 for the ESA L1b. In the data edited case the power threshold is set to 0, and the Coherence threshold differs between the two: 0.8 for the Own L1b and 0.85 for the ESA L1b. A critical note could be given on the filter threshold step size. Decreasing this step size could mean that the results derived from ESA L1b and from Own L1b approach each other better. However, when refining the power and coherence thresholds in-between these found optima no big changes were found.

When data editing is applied during the optimization, four times more data points are found. The standard deviation following from the GIMP DEM comparison are ~0.5 [m] higher. The sequential IceBridge comparison shows positive mean and median values. This shows that the height values calculated are on average overestimating the elevation, in contrast to the non-edited case. The standard deviation of L2-Swath to IceBridge differences increases for both the ESA L1b derived as well as the Own L1b derived L2 Swath case.

The fact that the FBR derived product mean and median values are on average higher than the ESA L1b derived ones, indicates a difference in the FBR to L1b processing. This difference between ESA L1b and FBR derived L1b can be clearly seen as plotted in figures 6.7 and 6.9. The ESA L1b derived L2-Swath measures show a large amount of negative IB differences, whereas in contrast the FBR derived L2 Swath show slightly more positive IB differences. As the filter setting for power is set to zero a lot of large positive CS-IB differences are included in the dataset.

Furthermore, it is shown that optimizing for the along-track (SSW) angle is shown to have an effect on the quality of the product. The standard deviations as well as the mean and median values showed on average a 10 % difference over the range of applied angles.

L2-Swath elevations versus results Gourmelen et al. (2017) It is seen that the quality of the results, in terms of standard deviation and mean of the differences with respect to IceBridge, as presented by Gourmelen et al. (2017) are not even nearly reached in this chapter, and thus not improved. It is difficult to give an exact reason for this difference. A few hypotheses will be given here.

First of all, this difference is not expected to be caused by a difference in FBR-to-L1b processing. The resulting FBR derived L1b results and the elevations compare well to the ESA L1b provided products as well as ESA L1b derived elevations, and it is stated by Gourmelen et al. (2017) that the ESA L1b product was used.

This difference may be caused by a difference in geographical area or time periods for which the analysis is run. It is uncertain what the area is that the analysis of Gourmelen et al. (2017) was done for. This can thus not be checked. However, it can be hypothesised what effect analysing a smaller/larger area or a different part of the Petermann Glacier would have on the results. It is expected that running the analysis over the parts more towards the ice sheet, would result in lower standard deviations. The reason for this is the smoothness of the

No DEM, no ref. Power	Al. Tr. Angle	0.8	0.7	0.6	0.5	0.4	0.3	0.2	ESA(0.7)
Optim. for $\frac{\sigma_{DEM}}{log(N_{meas})}$	Coh.	0.8	0.8	0.8	0.8	0.85	0.85	0.85	0.85
	Pow	0	0	0	0	0	0	0	0
	θ_{ac}	0.8	0.8	0.8	0.8	0.8	0.8	0.8	0.8
	σ_{DEM}	6.9850	6.9470	6.9266	6.9583	6.8259	6.8681	7.0755	7.1691
	N_{meas}	209506	227021	248917	264353	211086	221078	226988	221400
	Crit.	1.3127	1.2970	1.2836	1.2833	1.2820	1.2851	1.3210	1.3412
IB	Median	0.1695	0.1789	0.1794	0.1500	0.1523	0.1737	0.1101	0.0879
	μ_{IB}	0.7648	0.7950	0.7556	0.6728	0.7256	0.6630	0.6426	0.2712
	σ_{IB}	5.689	5.767	5.791	5.709	5.472	5.409	5.773	6.018
	N_{IB}	18234	19621	21635	23146	18428	19436	20005	19147

Table 6.11: Results from the CS to IB comparison for the two criteria used in the optimization. N denotes the number of CS measurements that was compared with an IB measurement.

No DEM, yes ref. Power	Al. Tr. Angle	0.8	0.7	0.6	0.5	0.4	0.3	0.2	ESA(0.7)
Optim. for $\frac{\sigma_{DEM}}{log(N_{meas})}$	Coh.	0.8	0.8	0.8	0.8	0.85	0.85	0.85	0.85
	Pow	0.003	0.002	0.0015	0.002	0.002	0.0015	0.0005	0.0005
	θ_{ac}	0.6	0.8	0.8	0.8	0.8	0.8	0.8	0.8
	σ_{DEM}	6.7451	6.8450	6.8261	6.6737	6.7038	6.7627	6.9495	7.4170
	N_{meas}	157046	209379	231911	183351	194831	205294	219125	219686
	Crit.	1.2981	1.2864	1.2723	1.2680	1.2673	1.2730	1.3012	1.3323
IB	Median	0.1469	0.1221	0.1264	0.1224	0.0884	0.1084	0.0521	0.0822
	μ_{IB}	0.5857	0.6829	0.6260	0.6800	0.6292	0.5422	0.3994	0.2735
	σ_{IB}	5.045	5.670	5.621	5.274	5.343	5.380	5.415	5.891
	N_{IB}	13259	17770	19829	15824	16808	17821	19245	19013

Table 6.12: Results from the CS to IB comparison for the two criteria used in the optimization. N denotes the number of CS measurements that was compared with an IB measurement.

Yes DEM, No ref. Power	Al. Tr. Angle	0.8	0.7	0.6	0.5	0.4	0.3	0.2	ESA(0.7)
Optim. for $\frac{\sigma_{DEM}}{log(N_{meas})}$	Coh.	0.8	0.8	0.8	0.8	0.85	0.85	0.85	0.85
	Pow	0	0	0	0	0	0	0	0
	θ_{ac}	0.6	0.8	0.8	0.8	0.8	0.8	0.8	0.8
	σ_{DEM}	6.8693	6.943	6.9269	6.9601	6.8168	6.8722	7.0567	7.1691
	N_{meas}	172229	227357	249718	265334	209926	220848	227377	221400
	Crit.	1.3119	1.2962	1.2834	1.2833	1.2809	1.2859	1.3174	1.3412
IB	Median	0.1938	0.1863	0.1802	0.1644	0.1691	0.1708	0.1401	0.0879
	μ_{IB}	0.7261	0.8006	0.7311	0.6775	0.6983	0.6156	0.6572	0.2712
	σ_{IB}	5.423	5.727	5.655	5.655	5.400	5.339	5.689	6.018
	N_{IB}	15060	19805	21714	23213	18387	19518	20025	19147

Table 6.13: Results from the CS to IB comparison for the two criteria used in the optimization. N denotes the number of CS measurements that was compared with an IB measurement.

Yes DEM, Yes ref. Power	Al. Tr. Angle	0.8	0.7	0.6	0.5	0.4	0.3	0.2	ESA(0.7)
Optim. for $\frac{\sigma_{DEM}}{log(N_{meas})}$	Coh.	0.8	0.8	0.85	0.85	0.85	0.85	0.85	0.85
	Pow	0.0025	0.0025	0.002	0.002	0.0015	0.0015	0.0005	0.0005
	θ_{ac}	0.6	0.6	0.8	0.8	0.8	0.8	0.8	0.8
	σ_{DEM}	6.6135	6.6926	6.6321	6.6373	6.6873	6.7491	6.9249	7.4170
	N_{meas}	158861	169420	170708	183897	196935	204972	219453	219686
	Crit.	1.2928	1.2799	1.2675	1.2608	1.2631	1.2706	1.2965	1.3323
IB	Median	0.1227	0.1529	0.1433	0.1284	0.1261	0.1102	0.0840	0.0822
	μ_{IB}	0.5234	0.6377	0.6623	0. 6133	0.6005	0.4814	0.4153	0.2735
	σ_{IB}	5.078	5.321	5.054	5.164	5.297	5.292	5.372	5.891
	N_{IB}	13470	14235	14671	15847	17047	17864	19258	19013

Table 6.14: Results from the CS to IB comparison for the two criteria used in the optimization. N denotes the number of CS measurements that was compared with an IB measurement.

terrain, which is expected to be higher the closer to the ice sheet one gets. Furthermore, the steeper surface angles are expected to be better suited for swath processing, following the logic as given by (Gray et al., 2013).

As for the difference in time periods one reason that could cause a difference in standard deviation to exist is the longer set of data. It is understood from Gourmelen et al. (2017) that a period covering March till May for the years 2010 till 2014 is used for analysis. A lower standard deviation over a longer period of time is found only when the standard deviations of the distributions corresponding to the other years are much lower compared to the standard deviations as presented in this chapter, assuming these distributions are independent of each other. Furthermore, the standard deviations would require to be very small to compensate for the standard deviations as found in this thesis. This is unlikely, considering that the Cryosat-2 data has become more accurate over time with the development of new Baselines (Bouffard, 2015), and quality analyses concerned with this did not find prove for any such degradation up till the year 2016 (Fornari et al., 2014) (Bouffard et al., 2018). As such it is not expected that the different time periods have caused this discrepancy.

Moreover, the difference may be caused by a difference within the L1b-to-L2 processing. Several steps within this processing can be related to this difference. Firstly, the application of the attitude correction angles is considered. These attitude corrections are applied in this thesis as provided in Scagliola (2018). It is stated by Gourmelen et al. (2017) that these corrections should largely correct for the roll bias present in Baseline C data. Moreover, it is stated that a roll bias present would cause the CS-IB distribution to be double-peaked, as the roll-bias would have a mirrored effect on measurements originating from descending and ascending orbits. This effect is not shown by the CS-IB distributions as found in this thesis. It is thus not expected to be the cause of the difference.

It is not known whether Gourmelen et al. (2017) apply an optimization scheme as applied in this thesis to determine the optimal filter settings. Furthermore, the across-track angle is not mentioned as a threshold variable. The data is mostly only qualified on power and coherence. The L1b-to-L2 processing chain was applied as developed by Slobbe et al. (2016) and described in chapter 4. Differences may still exist between the algorithm as described in Gourmelen et al. (2017) and this algorithm. For example, no exact description is given on the computation of the height from the range and angle measurement. Similarly, during the global phase unwrapping a second dispersion metric is used by Gourmelen et al. (2017) to add robustness to the phase ambiguity measurement. This has not been applied in this thesis.

When looking at the corresponding increase in data points, it can be seen that approximately the same amount of data points are found for the three months in 2017 in this thesis as the 4 times 3 months in Gourmelen et al. (2017). The ratio of POCA to Swath measures is approximately the same, namely equal to a ~5. This can be deducted when looking at the the amount of measurements found during verification with the threshold retracker (see table 5.1) which would represent the POCA case. This is only the case when no data editing is applied. The relatively low amount of data points over the same period could mean that a high amount of data editing is applied by Gourmelen et al. (2017) to get the result that is presented.

7

Conclusion and Recommendations

Within this chapter I first give a summary of the main results, followed by a short discussion. Then I state the conclusion of this study followed by some recommendations.

7.1. Summary of the main results

The goals as stated at the start of this thesis are considered here,

1. A FBR to L1b Cryosat-2 SARIn processor was successfully developed. The theory and methodology behind the processor are documented to the best of our knowledge within this thesis. The SARIn processor was implemented in MATLAB, based on a previously developed SAR processor (Cipollini, 2016). The biggest changes to the SAR processor are the dual channel capability, and the computations involved to correctly derive the Phase Difference and the Coherence.

2. The Swath processing algorithm was implemented, as written by Slobbe et al. (2016) of which a large part based on Gourmelen et al. (2017).

3. FBR datasets were collected over the Petermann Glacier, covering a period from March till May 2017, to produce the FBR derived L1b datasets. An ESA provided L1b dataset was collected, as well over the Petermann Glacier. These two datasets served as input to the Swath processing algorithm. Application of Swath processing to these datasets, produced two L2-Swath datasets. For verification and validation purposes, the datasets are analysed in an unfiltered L2-Swath state and a filtered L2-Swath state. The filtering here denotes the Swath processing filtering based on the three Swath processing criteria: Coherence, Power, and across-track angle.

4. The processor was verified by comparing the resulting L1b waveforms with ESA provided L1b waveforms. It is shown that ESA applies an artificial shift in range bins in order to align the waveforms. This shift in range does not result in different elevation values, as the window delay is corrected for accordingly. By applying a threshold retracker, and comparing the results to the GIMP DEM the results are verified. The results compare well when looking at the standard deviations with respect to the DEM.

   The coherence, across-track angles and power values, are compared before the Swath Processing filtering is applied. By comparing the resulting distributions collected over the Petermann Glacier, it is verified that these values are calculated correctly.

   Due to a lack of documentation, uncertainties remain regarding the Phase Cross Calibration. However, it has been proven that the CAL4 calibration does correct the phase differences in a correct manner. The across-track angle that follows from the phase difference compares well to ESA L1b results. The coherence values still showed a small discrepancy. More high valued coherence measurements were found when deriving the L2-Swath from the ESA L1b product compared to the FBR derived Swath measurements. This discrepancy does not have a big effect on the Swath processing results, as was shown by applying different distinct threshold settings.

   The unfiltered power values showed that more than 80 % of all data over the Petermann Glacier consisted of power values lower than 10 % of the maximum power.

5. The validation was performed by means of a comparison with IceBridge Laser altimetry data. In order to compare validation results derived from the ESA provided and the FBR derived L1b waveforms, an optimization was performed. This was achieved by optimizing the filter thresholds for the lowest $\sigma_{DEM}/log(N_{meas})$, where σ_{DEM} denotes the standard deviation of the differences between the Cryosat elevations and the GIMP DEM elevations, and N_{meas} the number of measurements.

   It was found that the optimized filter settings for the ESA L1b and FBR derived L2-Swath compare well. Almost identical swath processing filtering settings were found for Coherence, Power and Across-track angle when comparing ESA L1b derived L2-Swath and FBR derived L2-Swath. The effects of the discrepancy in Coherence distributions as found during verification on the consequential swath processing are minimized due to the optimization, which still resulted in highly similar threshold settings.

   The sensitivity of the L2 results with respect to IceBridge was tested for two variable inputs. The effects of applying a DEM during the FBR-to-L1b processing, and changing the Stack Sample Weighting criterium are shown.

   Two additional effects were tested during optimization: the filtering out of L2-Swath to DEM elevation differences of more than 50[m] and refining the power thresholds over which the optimization was run.

   A small sensitivity of the L2-Swath results is shown, on sample stack weighting, refining the power threshold steps and using a DEM in the FBR-to-L1b processing. The corresponding improvements are minor and the results found by swath processing the ESA L1b waveforms are not trumped in terms of the comparison to IceBridge.

   It was found that filtering out outliers during the optimization can increase the amount of data points found drastically. The resulting elevations consequentially show an increase in mean and median elevation difference, compared to IceBridge elevations, however accompanied by a minor increase in standard deviation. For both ESA provided L1b and FBR derived L2-Swath the elevations are on average positive.

   The optimal criterium $\sigma_{DEM}/log(N_{meas})$ is found when outlier filtering, refined power steps, a DEM and a SSW of 0.5 [Deg] is applied. The most accurate, in terms of standard deviation of the elevation differences with respect to IceBridge, is found when no outlier filtering is applied, a DEM is included, and with a SSW angle of 0.7 [Deg]. This combination results in a σ_{IB} of 4.782 [m]. This does trump the standard deviation as found by ESA L1b, however not the standard deviation as found in previous research (Gourmelen et al., 2017) (see table 7.1). The highest precision, in terms of smallest negative median difference with respect to IceBridge, for the FBR derived L2-Swath elevations was found without outlier filtering, by applying a DEM and at a SSW angle of 0.6 [Deg]. The result is a median of -0.6579 [m].

   In table 7.1 the results are listed, when optimization for $\sigma_{DEM}/log(N_{meas})$ is performed. The results that are shown are the results corresponding to the lowest criterium, and the results following optimization for $\sigma_{DEM}/log(N_{meas})$ but showing the best results in comparison to the IceBridge Data in terms of standard deviation.

ESA/FBR;	Number of Swath measurements	IB median	μ_{IB}	σ_{IB}
ESA; Min. Crit.	219686	0.0822	0.2735	5.891
FBR; Min. Crit.	183897	0.1284	0.6133	5.164
ESA; Min. σ_{IB}	49706	-0.5536	-0.4106	5.008
FBR; Min. σ_{IB}	54818	-0.6652	-0.5532	4.782
ESA; Gourmelen et al. (2017)	44900	-	-1.3	1.2

Table 7.1: Listing of the optimal solutions found.

7.2. Discussion

It was found that the highly variable topographic changes in the area of the Petermann Glacier causes data gaps to exist in the raw FBR data. This affects the window delay correction, and should be accounted for. As the stack samples originate from bursts with different window delay values, the window delay correction aligns the different samples of a stack to correct for this difference. One reference window delay needs to be chosen to which the other stack samples are corrected. The large topographic changes produce large window

delay alterations over a stack, that cause several high quality power waveforms to be removed. As a solution to the issue, the window delay was not interpolated over these data gaps and used as the reference window delay for the window delay correction. Instead, the stack sample with the highest power was chosen to represent the stack sample with the reference window delay. This approach showed to produce a similar amount of ESA L1b and Own L1b unfiltered L2-Swath data points over the Petermann Glacier, suggesting that this MPS strategy is applied as well in the ESA FBR-to-L1b processor. Whether ESA applies this strategy with the same theory in mind as explained here, remains a question, as no ESA documentation has been found regarding their FBR-to-L1b processor.

The difference between the ESA provided L1b and the FBR derived coherence distributions suggests that the variable come about in a slightly different manner. This idea is strengthened by the threshold values resulting from the optimization. In most cases the threshold values are slightly more relaxed in case of the FBR derived L2-Swath compared to the ESA provided L1b derived L2-Swath. This is expected to be related to the difference in coherence distributions, as less high coherence values are present in the FBR derived L2-Swath datasets.

It can be concluded that similar results are found for the ESA provided L1b waveforms compared to the FBR derived L1b waveforms. However, the precision of the measurements is hard to qualify, as slightly negative mean and median difference values are expected, due to the difference in surface interaction between the IceBridge Laser and Cryosat's Radar signals. This effect is shown by the results as presented by Gourmelen et al. (2017). These median values were calculated alongside the mean values, as the median values are expected to be less dependent on outliers. Nevertheless, the median an mean values do not differ much, suggesting that the positive average value found for lower optimization criteria is not caused by outliers but by a consistent overestimation of the elevation by the L2-Swath datasets. This overestimation is found for both ESA provided L1b derived and FBR derived L2-Swath results, suggesting that this overestimation is caused by a difference in application of the Swath Processing algorithm described by Gourmelen et al. (2017).

In Gourmelen et al. (2017) the same version of ESA L1b data is used, but most probably over a slightly different region and most definitely over different (set of) year(s), compared to this study. It is expected that this difference in study area may cause the differences as found between the results following from this study compared to the results from Gourmelen et al. (2017). Increasing the amount of years over which to run the analysis, is expected not to decrease the standard deviation of the elevation differences with IceBridge.

The sensitivity of the overall results to the application of a DEM or a change in SSW angle is small. ESA's choice for application of a SSW of 0.7 [Deg] in general does makes sense, following the results in this study. In contrast, the effects that follow from a different swath processing application, as the outlier filtering, seem to have much larger impact, mostly in terms of the amount of L2-Swath data points produced.

7.3. Conclusion

To draw a conclusion on this study the questions as stated in the introduction are answered. Firstly, the question was stated whether a FBR-to-L1b SARIn processor could be developed optimized for the marginal areas.

In this study a FBR-to-L1b processor was developed based on the SCOOP SAR processing as described by Cipollini (2016). This SAR processing scheme is originally designed for oceanic applications. Verification showed that the development of the FBR-to-L1b processor in this study was performed successfully. The largest processor alteration with respect to the original, was found to be related to the handling of data gaps which existed in the Cryosat-2 FBR files. These data gaps are most probably related to the large topography changes that exceed the range window size, which causes the altimeter to lose track of the surface. Interpolation of the window delay over these regions as performed in the SCOOP processor results in the missing of data in the eventual L2-Swath dataset. Moreover, the option to alter specific variables in the FBR-to-L1b processor allows for optimization of the processor for the marginal area.

The second question was whether the Swath processing of SARIn data within the margins of Greenland would benefit from applying such a dedicated FBR-to-L1b processing, instead of using the L1b product readily available as provided by ESA.

Overall, it can be concluded that the accuracy of the L2-Swath measurements following from the ESA L1b product can be improved by implementing the FBR-to-L1b processor as developed in this thesis. However, these improvements are only small. It is shown that the results produced by the dedicated FBR-to-L1b processing in this thesis, only minimally differ from the results with the ESA provided L1b data, at least in the case of the Petermann Glacier. It is shown as well that the ESA L1b product already applies a strategy in de-

termining the window delay value per surface location, which causes the FBR data gaps not to be translated to the eventual L2-Swath dataset. Hence, no advantage is provided here.

7.4. Recommendations

Although the FBR-to-L1b processing scheme developed and optimized in this study proved to yield only slightly better results for the Petermann Glacier compared to the ESA-provided data, there are still options for further improvements. Notably, research into either of the following.

- An thorough investigation into all calibration corrections that need to be applied is required to correctly develop a FBR-to-L1b processor. Overall documentation regarding the SARIn processing of Cryosat FBR data remains limited.
- Stack extension has been presented as an improvement to Swath Processing (Mondéjar et al., 2017), and is mainly applied within the FBR-to-L1b processor. This does show to be promising in my personal opinion. By extending the stack, the size of the range window is stretched beyond the conventional (in case of SARIn) 1024 range bins. This is based on the fact that within the marginal area, data is lost as a consequence of large variations in window delay correction.
- Coherence filtering may be applied during FBR to L1b processing already on the single stack samples (Mondéjar et al., 2017). Besides the increase of the stack quality, by filtering on single stack sample level, data storage and processing demands are lowered.
- A newly developed Swath Processing Algorithm, which is based on the smoothness of the phase difference is showing improvements over the use of coherence (Foresta et al., 2018).
- A beneficial addition to the research field would be on the subject of Stack Sample Weighting. In this thesis the SSW was applied over all waveforms independent of location. However, it is expected that it is mostly only required at locations where highly variable topographic changes are present, for example, large cliffs as present in the Petermann glacier area.
- The newly launched ICESAT-2 is a major improvement in providing larger scale validation in comparison to the low density Airborne IceBridge data as used in this thesis. These high measurement density is required to improve the high density swath processing results.
- In order to draw actual conclusions on the actual mean and median IB difference values a even more local research should be considered, potentially in combination with knowledge of the surface types. Perhaps (machine learning) analyses combining optical satellite images with radar altimetry, could prove useful in assessing the interaction characteristics of surface and signal.

A

Verification

A.1. SARIn Waveforms 01-03-2017

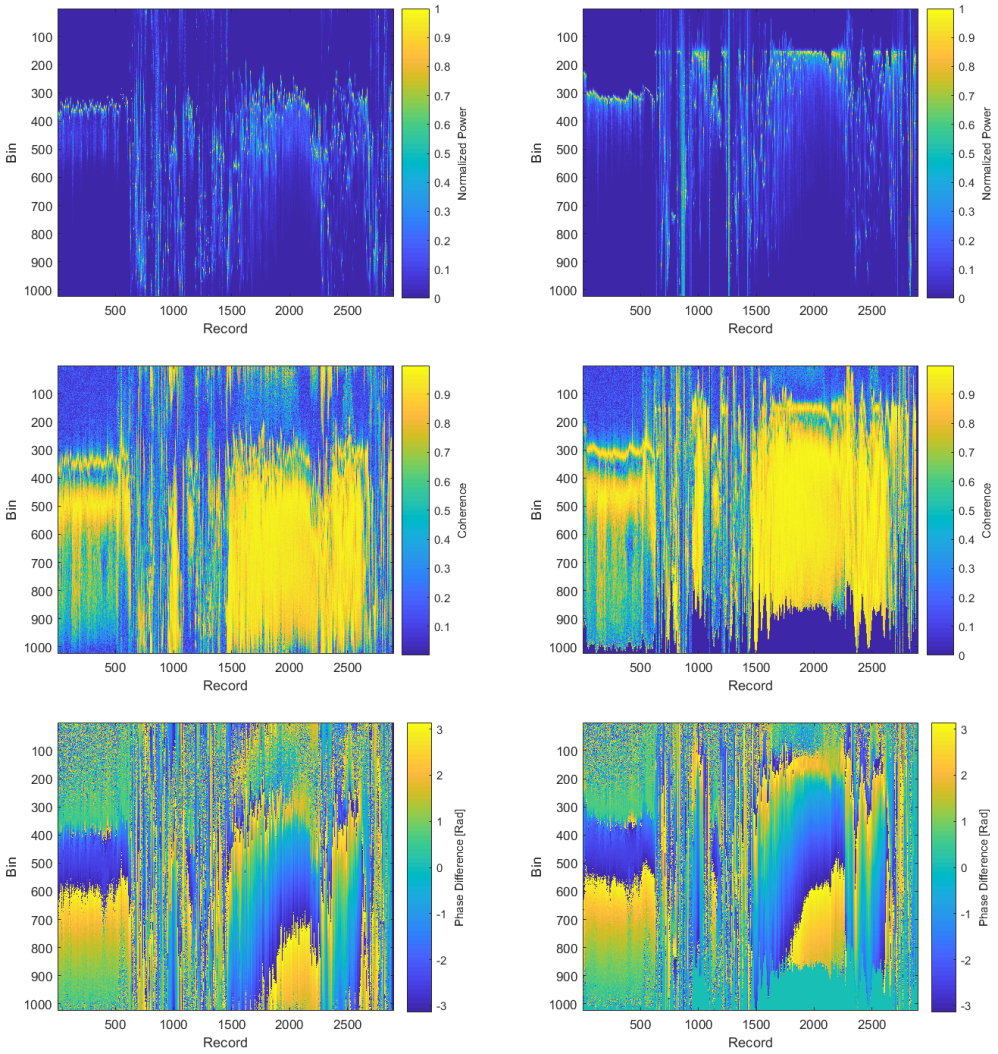

Figure A.1: The Power, Coherence, and Phase Difference waveforms corresponding to the SARIn overpass of the 1'st of March 2017. The FBR derived values are seen on the left, whereas the ESA L1b provided values are seen on the right.

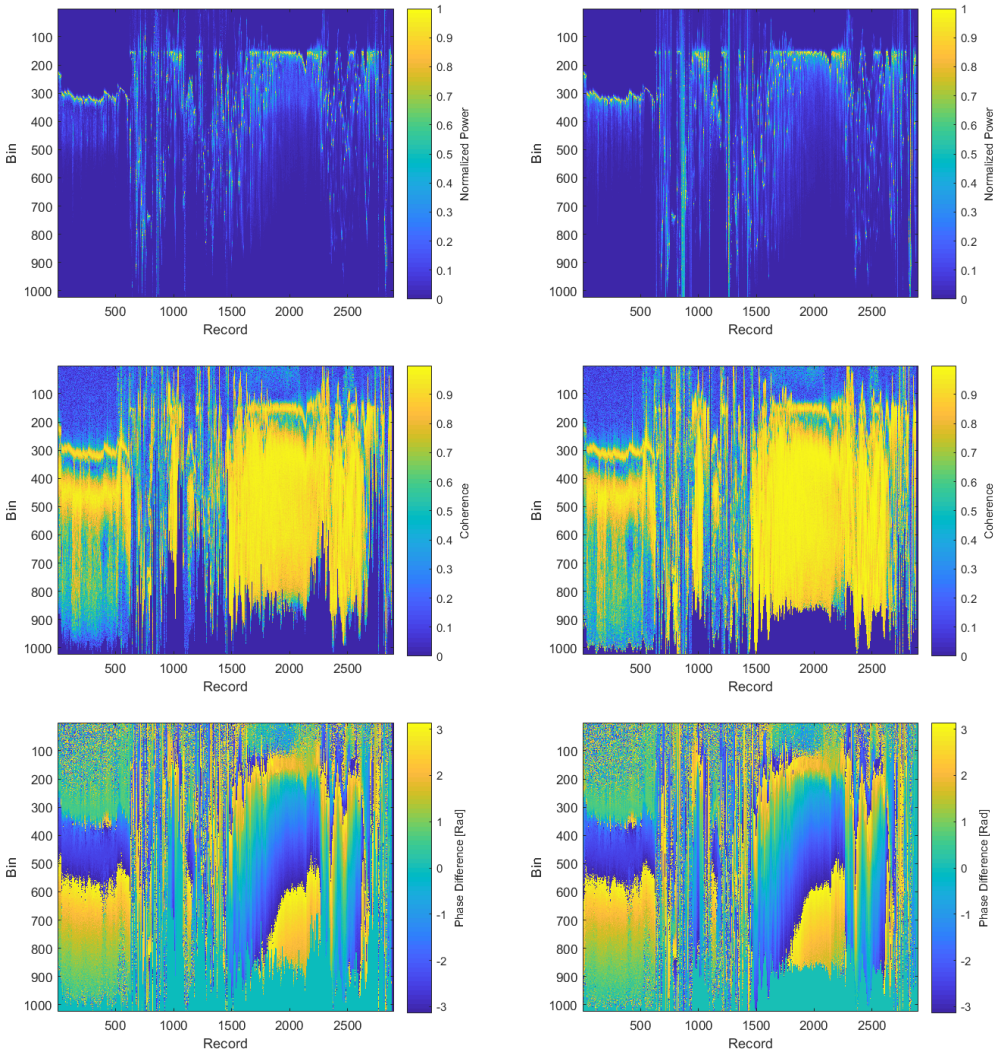

Figure A.2: The Power, Coherence, and Phase Difference waveforms corresponding to the SARIn overpass of the 1'st of March 2017. The shifted FBR derived values are seen on the left, whereas the ESA L1b provided values are seen on the right. The shift is proportional to the difference in window delay between the two datasets.

A.2. Window Delay Correction with Interpolation

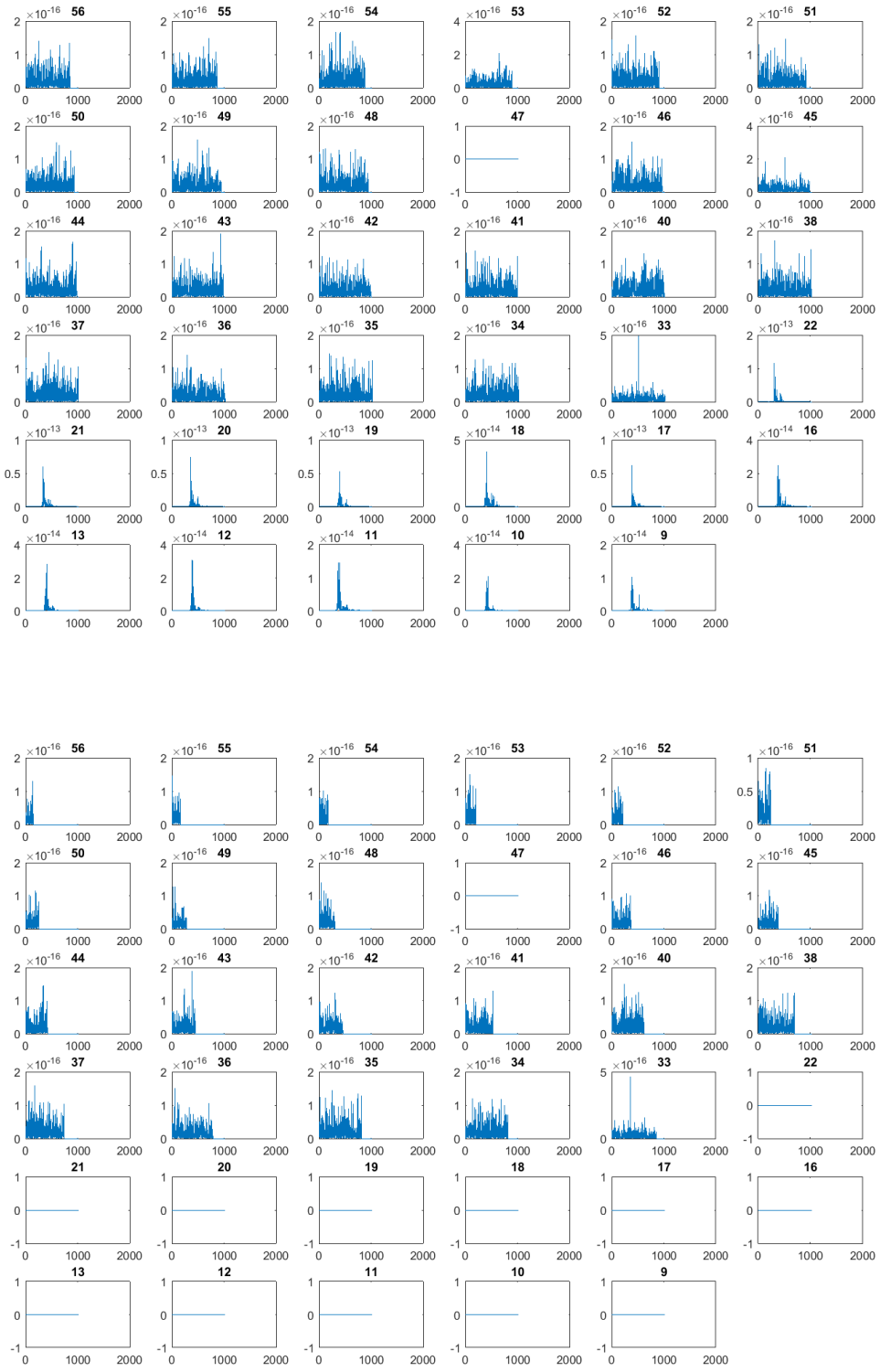

Figure A.3: Two sets of stack sample waveforms without Window Delay Correction and with Window Delay Correction. The separate plots correspond to the individual beams within a stack. The beams are numbered starting from 1, which is aft-looking to 64 which is forward looking

Bibliography

Borstad, C., D. McGrath, and A. Pope
2017. Fracture propagation and stability of ice shelves governed by ice shelf heterogeneity. *Geophysical Research Letters*, 44(9):4186–4194.

Bouffard, J.
2015. CRYOSAT-2 and quality improvements Baseline C. Technical report.

Bouffard, J., E. Webb, M. Scagliola, A. Garcia-Mondéjar, S. Baker, D. Brockley, J. Gaudelli, A. Muir, A. Hall, R. Mannan, M. Roca, M. Fornari, P. Féménias, and T. Parrinello
2018. CryoSat instrument performance and ice product quality status. *Advances in Space Research*, 2.

Braun, M., a. Humbert, and a. Moll
2008. Changes of Wilkins Ice Shelf over the past 15 years and inferences on its stability. *The Cryosphere Discussions*, 2(3):341–382.

Chelton, D. B., E. J. Walsh, and J. L. MacArthur
1989. Pulse Compression and Sea Level Tracking in Satellite Altimetry.

Christie, F. D. W., R. G. Bingham, N. Gourmelen, S. F. B. Tett, and A. Muto
2016. Four-decade record of pervasive grounding line retreat along the Bellingshausen margin of West Antarctica. *Geophysical Research Letters*, 43(11):5741–5749.

Cipollini, P.
2016. SAR Altimetry Coastal and Open Ocean Performance. Technical Report January, ESA.

Davis, C. H.
1995. Growth of the Greenland Ice Sheet: A Performance\rAssessment of Altimeter Retracking Algorithms. *IEEE Transections on Geoscience and Remote sensing*, 33(5).

Davis, C. H.
1997. A robust threshold retracking algorithm for measuring ice-sheet surface elevation change from satellite radar altimeters. *IEEE Transactions on Geoscience and Remote Sensing*, 35(4):974–979.

Dinardo, S.
2013. Guidelines for the SAR (Delay-Doppler) L1b Processing. Technical report, XCRY-GSEG-EOPS-TN-14-0042, ESRIN.

ESA
2012. CryoSat Product Handbook. Technical report, ESA.

Foresta, L., N. Gourmelen, F. Pálsson, P. Nienow, H. Björnsson, and A. Shepherd
2016. Surface Elevation Change and Mass Balance Of Icelandic Ice Caps Derived From Swath Mode CryoSat-2 Altimetry. *Geophysical Research Letters*.

Foresta, L., N. Gourmelen, F. Weissgerber, P. Nienow, J. J. Williams, A. Shepherd, M. R. Drinkwater, and S. Plummer
2018. Heterogeneous and rapid ice loss over the Patagonian Ice Fields revealed by CryoSat-2 swath radar altimetry. *Remote Sensing of Environment*, 211(November 2017):441–455.

Fornari, M., M. Scagliola, N. Tagliani, T. Parrinello, and A. G. Mondejar
2014. CryoSat: SIRAL calibration and performance. *International Geoscience and Remote Sensing Symposium (IGARSS)*, Pp. 702–705.

Fricker, H. A. and L. Padman
2012. Thirty years of elevation change on Antarctic Peninsula ice shelves from multimission satellite radar altimetry. *Journal of Geophysical Research: Oceans*, 117(2):1–17.

Fricker, H. A., N. W. Young, R. Coleman, J. N. Bassis, and J. B. Minster
2005. Multi-year monitoring of rift propagation on the Amery Ice Shelf, East Antarctica. *Geophysical Research Letters*, 32(2):1–5.

Fu, L.-l. and A. Cazenave
2001. *Satellite Altimetry and Earth Sciences: A Handbook of Techniques and Applications*. Academic Press.

Galin, N., D. J. Wingham, R. Cullen, M. Fornari, W. H. F. Smith, and S. Abdalla
2013. Calibration of the CryoSat-2 interferometer and measurement of across-track ocean slope. *IEEE Transactions on Geoscience and Remote Sensing*, 51(1):57–72.

Gardner, A. S., G. Moholdt, J. G. Cogley, B. Wouters, A. A. Arendt, J. Wahr, E. Berthier, R. Hock, W. T. Pfeffer, G. Kaser, S. R. M. Ligtenberg, T. Bolch, M. J. Sharp, J. O. Hagen, M. R. van den Broeke, and F. Paul
2013. A Reconciled Estimate of Glacier Contributions to Sea Level Rise: 2003 to 2009. *Science*, 340(6134):852–857.

Glasser, N. F. and T. A. Scambos
2008. A structural glaciological analysis of the 2002 Larsen B ice-shelf collapse. *Journal of Glaciology*, 54(184):3–16.

Gourmelen, N., M. J. Escorihuela, A. Shepherd, L. Foresta, A. Muir, A. Garcia-Mondejar, M. Roca, S. G. Baker, and M. R. Drinkwater
2017. CryoSat-2 swath interferometric altimetry for mapping ice elevation and elevation change. *Advances in Space Research*.

Gray, L., D. Burgess, L. Copland, R. Cullen, N. Galin, R. Hawley, and V. Helm
2013. Interferometric swath processing of Cryosat data for glacial ice topography. *Cryosphere*, 7(6):1857–1867.

Hawley, R. L., A. Shepherd, R. Cullen, V. Helm, and D. J. Wingham
2009. Ice-sheet elevations from across-track processing of airborne interferometric radar altimetry. *Geophysical Research Letters*, 36(22):1–5.

Helm, V., A. Humbert, and H. Miller
2014. Elevation and elevation change of Greenland and Antarctica derived from CryoSat-2. *The Cryosphere*, 8(4):1539–1559.

Howat, I. M., A. Negrete, and B. E. Smith
2014. The Greenland Ice Mapping Project (GIMP) land classification and surface elevation data sets. *The Cryosphere*, 8(4):1509–1518.

IPCC
2013. *Climate Change 2013: The Physical Science Basis. Contribution of Working Group I to the Fifth Assessment Report of the Intergovern- mental Panel on Climate Change*. Cambridge University Press.

Jensen, J.
1999. Angle measurement with a phase monopulse radar altimeter. *IEEE Transactions on Antennas and Propagation*, 47(4):715–724.

Joughin, I. and D. R. MacAyeal
2005. Calving of large tabular icebergs from ice shelf rift systems. *Geophysical Research Letters*, 32(2):1–4.

Kleinherenbrink, M., P. G. Ditmar, and R. C. Lindenbergh
2014. Retracking Cryosat data in the SARIn mode and robust lake level extraction. *Remote Sensing of Environment*, 152:38–50.

Mantovani, P.
2015. CryoSat Ground Segment. IPF L1b. Product Specification Format. Technical Report CS-RS-ACS-GS-5106 6.4, Advanced Computer Systems (ACS).

Martin, C. F., W. B. Krabill, S. S. Manizade, R. L. Russell, J. G. Sonntag, R. N. Swift, and J. K. Yungel
2012. Airborne Topographic Mapper Calibration Procedures and Accuracy Assessment. *Nasa technical memorandum*, TM–2012-21(February).

Massom, R. A., A. B. Giles, R. C. Warner, H. A. Fricker, B. Legrésy, G. Hyland, L. Lescarmontier, and N. Young
2015. External influences on the Mertz Glacier Tongue (East Antarctica) in the decade leading up to its calving in 2010. *Journal of Geophysical Research: Earth Surface*, (February 2010):1–17.

Mondéjar, A., M. Escorihuela, M. Roca, E. Makhoul, F. Weissgerber, and N. Gourmelen
2017. Swath Processing Improvements of CryoSat-2 for the Study of Ice Caps and Mountain Glaciers.

Münchow, A., L. Padman, P. Washam, and K. Nicholls
2016. The Ice Shelf of Petermann Gletscher, North Greenland, and Its Connection to the Arctic and Atlantic Oceans. *Oceanography*, 29(4):84–95.

Nilsson, J., A. Gardner, L. Sandberg Sørensen, and R. Forsberg
2016. Improved retrieval of land ice topography from CryoSat-2 data and its impact for volume change estimation of the Greenland Ice Sheet. *The Cryosphere Discussions*, Pp. 1–47.

Noël, B., W. J. van de Berg, S. Lhermitte, B. Wouters, H. Machguth, I. Howat, M. Citterio, G. Moholdt, J. T. M. Lenaerts, and M. R. van den Broeke
2017. A tipping point in refreezing accelerates mass loss of Greenland's glaciers and ice caps. *Nature Communications, Published online: 31 March 2017; | doi:10.1038/ncomms14730*, 22(9296):3055–3071.

Paolo, F. S., H. A. Fricker, and L. Padman
2015. Volume loss from Antarctic ice shelves is accelerating. *Science*, 348(6232):327–331.

Prats-iraola, P., S. Member, R. Scheiber, M. Rodriguez-cassola, J. Mittermayer, S. Wollstadt, F. D. Zan, B. Bräutigam, M. Schwerdt, A. Reigber, S. Member, and A. Moreira
2014. On the Processing of Very High Resolution Spaceborne SAR Data. *IEEE Transactions on Geoscience and Remote Sensing*, 52(10):6003–6016.

Pritchard, H., S. Ligtenberg, H. Fricker, D. Vaughan, M. van den Broeke, and L. Padman
2012. Antarctic ice-sheet loss driven by basal melting of ice shelves. *Nature*, 484(7395):502–505.

Pritchard, H. D., R. J. Arthern, D. G. Vaughan, and L. A. Edwards
2009. Extensive dynamic thinning on the margins of the Greenland and Antarctic ice sheets. *Nature*, 461(7266):971–975.

Quartly, G. D., M. A. Srokosz, and T. H. Guymer
1998. Understanding the effects of rain on radar altimeter waveforms. *Advances in Space Research*, 22(11):1567–1570.

Raney, R. K.
1998. The Delay/Doppler Radar Altimeter. *IEEE Transactions on Geoscience and Remote Sensing*, 36(5 PART 1):1578–1588.

Rees, W. G.
2012. *Physical Principles of Remote Sensing*, 1st edition. Cambridge: Cambridge University Press.

Rignot, E., G. Casassa, P. Gogineni, W. Krabill, A. Rivera, and R. Thomas
2004. Accelerated ice discharge from the Antarctic Peninsula following the collapse of Larsen B ice shelf. *Geophysical Research Letters*, 31(August):2–5.

Rignot, E. and P. Kanagaratnam
2006. Changes in the Velocity Structure of the Greenland Ice Sheet. *Science*, 311(5763):986–990.

Scagliola, M.
2018. Test dataset of mispointing angles corrected for aberration of light. Technical report, C2-TN-ARES-GS-5192, Aresys.

Scagliola, M. and M. Fornari
2015. Main evolutions and expected quality improvements in BaselineC Level1b products. *C2-Tn-Ars-Gs-5154*, (1.1):1–43.

Scagliola, M., M. Fornari, and T. Parrinelo
2016. CryoSat Characterization for FBR users. Technical Report 2.0, C2-TN-ARS-GS-5179, Aresys.

Scagliola, M., N. Tagliani, and M. Fornari
2013. Measuring the Effective Along-Track Resolution of Cryosat. *Proceedings of the Cryosat Third User Workship*, (April).

Scott, J. B. T., D. Mair, P. Nienow, V. Parry, and E. Morris
2006. A ground-based radar backscatter investigation in the percolation zone of the Greenland ice sheet. *Handbook of Environmental Chemistry, Volume 5: Water Pollution*, 104(4):361–373.

Shepherd, A., D. Wingham, D. Wallis, K. Giles, S. Laxon, and A. V. Sundal
2010. Recent loss of floating ice and the consequent sea level contribution. *Geophysical Research Letters*, 37(13):1–5.

Simonsen, S. B. and L. S. Sørensen
2017. Implications of changing scattering properties on Greenland ice sheet volume change from Cryosat-2 altimetry. *Remote Sensing of Environment*, 190:207–216.

Slobbe, D., S. Nanda, and M. Kleinherenbrink
2016. Elevation changes of the coastal Greenland ice sheet from CryoSat-2 SARIn. In *European Space Agency Living Planet Symposium, May 9 – May 13 2016, Prague, Czech Republic*.

Tollefson, J.
2017. Larsen C ' s big divide. *Nature*, 542:402–403.

Wang, F., J. L. Bamber, and X. Cheng
2015. Accuracy and Performance of CryoSat-2 SARIn Mode Data Over Antarctica. *IEEE Geoscience and Remote Sensing Letters*, 12(7):1516–1520.

Wingham, D. J., C. R. Francis, S. Baker, C. Bouzinac, D. Brockley, R. Cullen, P. de Chateau-Thierry, S. W. Laxon, U. Mallow, C. Mavrocordatos, L. Phalippou, G. Ratier, L. Rey, F. Rostan, P. Viau, and D. W. Wallis
2006. CryoSat: A mission to determine the fluctuations in Earth's land and marine ice fields. *Advances in Space Research*, 37(4):841–871.

Wouters, B., D. Chambers, and E. J. O. Schrama
2008. GRACE observes small-scale mass loss in Greenland. *Geophysical Research Letters*, 35(20).

Wuebbles, D., D. Fahey, K. Hibbard, D. Dokken, B. Stewart, and T. Maycock
2017. USGCRP Climate Science Special Report: Fourth National Climate Assessment. 1:470.

Zwally, H. J., M. B. Giovinetto, J. Li, H. G. Cornejo, and M. A. Beckley
2005. Mass changes of the Greenland and Antarctica ice sheets and shelves and contributions to sea level rise: 1992-2002. *Journal of Glaciology*, 51(175):509.